U.PORTO
FEUP FACULDADE DE ENGENHARIA UNIVERSIDADE DO PORTO
Departamento de Engenharia Química

efacec

Lepae

Addressing sealing and counter-electrode challenges of dye solar cells towards industrialization

Rui Alberto Teixeira Cruz

Thesis dissertation presented for obtaining the degree of

Doctor in Chemical and Biological Engineering

by the

Faculdade de Engenharia da Universidade do Porto

Advisors:

Adélio Miguel Magalhães Mendes, Associate Professor with "Agregação"

Fernando José Rabaça Vaz, EFACEC Engenharia & Sistemas S.A.

2013

GOVERNO DA REPÚBLICA PORTUGUESA
FCT Fundação para a Ciência e a Tecnologia
MINISTÉRIO DA EDUCAÇÃO E CIÊNCIA
adi agência de inovação
COMPETE PROGRAMA OPERACIONAL FACTORES DE COMPETITIVIDADE
QREN QUADRO DE REFERÊNCIA ESTRATÉGICO NACIONAL PORTUGAL 2007-2013
UNIÃO EUROPEIA Fundo Europeu de Desenvolvimento Regional

Provas de Doutoramento: "Addressing sealing and counter-electrode challenges of dye solar cells towards industrialization"

Provas de Doutoramento em Engenharia Química e Biológica

Requeridas por:

Rui Alberto Teixeira Cruz

Data, Hora e Local

Dia 16 de setembro, às 14h30, na Sala de Atos da Faculdade de Engenharia da Universidade do Porto

Presidente Juri

Doutor Romualdo Luís Ribera Salcedo, Professor Catedrático da FEUP

Vogais

Doutor Hugo Manuel Brito Águas, Professor Auxiliar do Departamento de Ciências dos Materiais da Faculdade de Ciências e Tecnologia da Universidade Nova de Lisboa;

Doutora Maria da Conceição Jesus Rego Paiva, Professora Associada do Departamento de Engenharia de Polímeros da Escola de Engenharia da Universidade do Minho;

Engenheiro Fernando José Rabaça Vaz, Administrador EFACEC Engenharia (Coorientador);

Doutor José Miguel Loureiro, Professor Associado com Agregação do Departamento de Engenharia Química da Faculdade de Engenharia da Universidade do Porto;

Doutor Adélio Miguel Magalhães Mendes, Professor Associado com Agregação do Departamento de Engenharia Química da Faculdade de Engenharia da Universidade do Porto (Orientador);

Doutora Luísa Manuela Madureira Andrade, Investigadora Auxiliar do Departamento de Engenharia Química da Faculdade de Engenharia da Universidade do Porto.

Acknowledgments

I would like to acknowledge the Portuguese Foundation for Science and Technology (FCT) and Efacec – Engenharia e Sistemas S.A. for my Ph.D grant (SFRH/BDE/33439/2008) and all the support. Also I would like to acknowledge projects SolarSel SI IDT - 3423/2008 and WinDSC SI&IDT (ref. 21539/2011) both under framework of the QREN Initiative and the European Regional Development Fund through the Operational Program for Competitiveness Factors. Also I would like to acknowledge project SolarConcept (PTDC/EQU-EQU/120064/2010) for funding.

A very special thank you to my advisors, Prof. Adélio Mendes and Eng. Fernando Vaz and also Nuno Delgado. Prof. Adélio Mendes is right, hard work pays off in the end. I could not have done the work without prof. Adélio Mendes. A special thanks to Drª Luisa Andrade for all the help and discussions. Also I would like to thank all the solar group, and particularly José and Fernando for such a good (team) job. And also thank you all the LEPAE staff.

To all those who stood by my side during all this time, thank you very much for the support and laughs and desperation times.

A special thank you to my father and my mother for making such a good job raising me and caring for me and loving me. This thesis is specially for them. And to my brother for being there for me. I would like to thank all the rest of my family for all the support.

And finally to Filipa. For being the perfect woman for me. Thank you.

P.S If I forgot to mention you and you took offence, please forgive me and know that I thank you too.

“The world that we have made as a result of the level of thinking we have done thus far creates problems that we cannot solve at the same level as the level we created them at.”

(Albert Einstein)

Preface

The present work developed for this dissertation was carried out at the Laboratory of Processes, Environmental and Energy Engineering (LEPAE) facilities, in the Chemical Department of the Faculty of Engineering of the University of Porto (FEUP) and the facilities of Efacec – Engenharia e Sistemas S.A., between 2009 and 2012. All work was accomplished under the grant SFRH/BDE/33439/2008.

The dissertion is comprised of 4 scientific papers and two more add-on chapters, aimed to offer additional relevant information.

Contents

Abstract

In this day and age, the need for sustainable and competitive renewable energy sources is increasing, motivated by the ever-increasing energy costs and depleting nature of conventional energy sources. Photovoltaic systems that convert sunlight into electricity are surely part of the solution for such problem. A dye-sensitized solar cell (DSC) is a type of electrochemical system capable of delivering electricity, which technology has reached a point of maturation that leaves it on the brink of commercial viability.

This thesis aimed to narrow the bridge that still exists between the lab-scale technology and the fully developed marketable product. Specifically, the present work aimed at two key points. Firstly, the development of an alternative and low-cost catalyst responsible for the electrochemical reaction that takes place at the counter-electrode (CE) side. Secondly, the development of a reliable sealing technique for the typical DSC configuration that uses glass substrates, capable of obliging market demands for long-time operation.

Carbon-based materials were studied as replacements for the traditionally used catalyst – platinum (Pt), for the most commonly used iodide-type redox electrolytes. The catalytic activity of all materials was assessed based on their electrochemical impedance spectroscopy parameters and the current-voltages curves of the corresponding DSCs. Additionally the transparency of the CEs was also observed, as high transparent electrodes offe added value to the final product. The structural properties of both the carbon-based materials and the final catalytic films of such materials were also characterized. Single wall carbon nanohorns (SWNH), either in pristine and Pt-decorated structures, were studied as viable replacements to Pt. The use of stand-alone graphene oxide (GO) platelets was investigated. A new manufacturing process is disclosed as it was discovered that thermal reduction of GO under an inert atmosphere yielded films as catalytic as the use of thermally annealed previously chemically reduced GO platelets. To match the performance and transparency of Pt it was

necessary to create a graphene/Ni composite electrode, where oxidized graphene nanoplatelets were placed on top of a FTO substrate decorated with electrophoretically deposited nickel particles.

A novel sealing method for proper encapsulation of DSCs based of glass substrates was developed. The method relies on the use of a laser beam to provide localized heating to the sealing element that is a glass frit. The integration and applicability of graphene films with the developed laser-assisted glass frit sealing on scaled-up pre-module DSCs (active area of 4 cm^2) was also investigated. Preliminary tests seemed to indicate the validity of the application.

Sumário

Atualmente existe uma necessidade cada vez mais crescente para tentar encontrar fontes de energias que sejam renováveis e competitivas. Isto acontece devido ao crescente aumento do custo das fontes de energias convencionais devido à sua depleção. Uma possível resposta para este problema são os sistemas fotovoltaicos que convertem a luz solar em eletricidade. Uma célula solar sensibilizada por corante (*Dye-sensitized Solar Cells*, DSCs) é um tipo de sistema eletroquímico capaz de produzir eletricidade, sendo que a sua tecnologia atingiu um estado de maturação tal, que se encontra neste momento muito próxima da viabilidade comercial.

A presente tese pretende diminuir a diferença existente entre células de tamanho laboratorial e de dimensões médias (próximas do produto final). Concretamente, o trabalho apresentado focou-se em dois grandes objetivos. O primeiro objetivo passou por desenvolver uma alternativa viável, eficiente e de baixo custo ao catalisador responsável pela reação eletroquímica que se dá no lado do contra-elétrodo. O segundo objetivo teve em consideração o desenvolvimento de uma técnica de selagem fiável, aplicável a uma DSC com uma configuração típica que usa substratos de vidro, e capaz de responder às necessidades do mercado da energia fotovoltaica em termos de durabilidade a longo prazo.

Foram testados diversos materiais à base de carbono como possíveis substitutos do material tradicionalmente usado como catalisador – platina (Pt), para os eletrólitos mais usados que contêm um par de iões redox de base iodo. A atividade catalítica dos filmes foi avaliada com base nos resultados de análises de DSCs fabricadas com esses mesmos filmes como contra-elétrodos. A sua avaliação foi realizada usando espetroscopia de impedância eletroquímica e curvas de corrente – voltagem. Paralelamente foi também avaliada a transparência dos contra-elétrodos com os materiais à base de carbono, pois elétrodos altamente transparentes adicionam valor ao produto final. Foi

igualmente realizada uma caracterização da estrutura dos filmes fabricados com os materiais à base de carbono.

Foram estudados nanocones de carbono de parede única (*Single Wall Carbon Nanohorns*, SWNH), sob uma forma inalterada ou recobertos com partículas de Pt, como possíveis substitutos dos contra-elétrodos de Pt. Foram também estudados filmes à base de grafeno. Foi descoberto um novo processo de fabrico de contra-elétrodos à base de grafeno oxidado. Verificou-se que a redução dos filmes de óxido de grafeno através do recozimento térmico originava filmes que eram tão catalíticos como se fosse usado óxido de grafeno termicamente recozido que tinha sido previamente reduzido por métodos químicos. No entanto, para igualar o desempenho e transparência da Pt foi necessário criar um elétrodo compósito de grafeno e Ni. Este compósito envolveu recobrir um substrato de vidro (já por si coberto com uma camada de um óxido condutor) com partículas de Ni através de um método eletroforético e posteriormente aplicar no topo, nanoplaquetas de grafeno previamente oxidadas.

Foi também estudado e desenvolvido um novo método eficaz de selagem para as DSCs baseadas em substratos de vidro. O método é baseado no uso de um feixe laser que providencia um aquecimento localizado ao elemento selante (uma frita de vidro). Foi ainda avaliada a aplicabilidade da integração dos contra-elétrodos desenvolvidos à base de grafeno com o método da selagem laser de fritas de vidro e o aumento de escala deste novo método de selagem em sub-módulos de pequenas dimensões (área ativa da DSC de 4 cm^2). Testes preliminares parecem validar, quer o aumento de escala, quer a integração dos contra-elétrodos à base de grafeno, de DSCs seladas a laser com uma frita de vidro sem que haja uma perda de desempenho.

Figure Captions

Table Captions

Abbreviations and Symbols

Abbreviation / Symbol	**Definition**	**Units**
2D	2 dimensions	
A	Electrode area	cm^2/ m^2
AM	Air mass	
AC	Alternating current	
Al_2O_3	Aluminium oxide	
AFM	Atomic force microscopy	
Ag	Silver	
AgCl	Silver Chloride	
AGO	Thermally annealed graphene oxide	
ARGO	Thermally annealed chemically reduced graphene oxide	
a-Si	Amorphous silicon	
a-Si/µcSi	Amorphous / Microcrystalline silicon	
BIPV	Building integrated photovoltaic	
BTU	British thermal unit	~ 1055 J
ca.	circa	
C	Capacitance	F or µF
C_{CE}	Double-layer capacitance at the CE	µF cm^{-2}
C_{μ}	Chemical capacitance	F or µF
CO_2	Carbon dioxide	
CB	Carbon black or Conduction band	

CE	Counter electrode	
CPE	Constant phase element	
CPE:B	Capacitance measurement in a constant phase element	µF or µF cm^{-2}
CPE:β	Empirical constant in constant phase elements	
CMC	Carboxymethyl cellulose	
CdS	Cadmium sulphide	
CdTe	Cadmium telluride	
CIS	Copper indium diselenide	
c-Si	Crystalline Silicon	
CMOS	Complementary metal-oxide-semiconductor	
DSC	Dye-sensitized Solar Cell or Differential scanning calorimetry	
DTA	Differential thermal analysis	
e^-	Electrons	
E_C	Conduction band energy	J
E_F	Semiconductor's Fermi energy	J
E_g	Bandgap energy	J
E_{Redox}	Redox energy of the electrolyte	J
E_{VB}	Valence band energy	J
E_{2g}	Doubly degenerate in-plane optical vibration in Raman spectrocopy	
EIS	Electrochemical impedance spectroscopy	
EG	Ethylene glycol	
EDP	Electrophoretic deposition	

EDS	Energy dispersive spectroscopy	
f	Frequency	Hz or s^{-1}
F	Faraday constant (F = 96 485,3399(24) C mol^{-1})	C mol^{-1}
FF	Fill factor	
FTO	Fluorine-doped tin-oxide	
GaAs	Gallium arsenide	
GMWNT	Graphene and multi-walled carbon nanotubes	
GO	Graphene oxide	
GnPM5	Commercial graphene with a M5 grade	
h	Planck constant (h = 6.62606896(33)×10^{-34} J s)	J s
h^+	Holes	
HOMO	Highest occupied molecular orbital	
HS-SWNH	High surface single-walled nanohorns	
HEC	Hydroxyethyl cellulose	
H_2O_2	Hydrogen peroxide	
H_2O	Water	
HCl	Hydrochloric acid	
H_3BO_3	Boric acid	
I	Electrical current or electrical current density	mA or mA cm^{-2}
$I(t)$	Current response	mA
I_{oc}	Open-circuit current	mA
I_{MPP}	Current at the maximum-power point	mA
I-V	Current-voltage or Current density-voltage	

$I_{/Pt}$-V	Current density normalized by the amount of Pt used per deposited area-voltage	
$I_{/Pt}$	Current density normalized by the amount of Pt used per deposited area	$\Omega\ \mu g Pt^{-1}$
I_s	Incident light intensity	mW cm^{-2}
I_{sc}	Short-circuit current	mA
I_0	Amplitude of the current signal	mA
i	Imaginary number	
I_D	Intensity of the D band in Raman spectroscopy	
I_G	Intensity of the G band in Raman spectroscopy	
I_D/I_G	Intensity ratio of D band to G band in Raman spectroscopy	
I^-	Iodide	
I_2	Iodine	
I_3^-	Triiodide	
ITO	Indium-tin-oxide	
IPCE	Incident photon-to-current conversion efficiency	%
IEC	International Electrotechnical Commission	
InP	Indium phosphide	
IR	Infrared	
j_0	Exchange current density	mA cm^{-2}
J_{sc}	Short-circuit photocurrent density	mA cm^{-2}
J_{MPP}	Current density at the maximum-power point	mA cm^{-2}
k_B	Boltzman constant (k_B = 1.3806504 (24) 10^{-23} J/K)	
k_{e-}	Recombination rate constant	s^{-1}

KI	Potassium iodide
K^+	Potassium ion
KCl	Potassium chloride
K	Potassium
$KMnO_4$	Potassium permanganate
Li	Lithium
Li^+	Lithium ion
LiI	Lithium iodide
LUMO	Lowest unoccupied molecular orbital
LHE	Light harvesting efficiency
mGOM5	Thermally annealed oxidized commercial graphene with a M5 grade
MPN	3-Methoxypropionitrile
MPP	Maximum-power point
MgO	Magnesium oxide
MLCT	Metal-to-ligand charge transfer
MEMS	Microelectromechanical systems
n	Empirical constant in constant phase elements or the number of electrons transferred in a reaction
N719	Dye molecule - cis-diisothiocyanato-bis(2,2'-bipyridyl-4,4'-dicarboxylato) ruthenium(II) bis(tetrabutylammonium)
N3	Dye molecule - cis-bis(4,4'-dicarboxylate-2,2'-bypiridine) ruthenium (II)
NCS	Isothiocyanato group
NHE	Normal hydrogen electrode

NIR	Near infrared	
NaOH	Sodium hydroxide	
NaI	Sodium iodide	
Na^+	Sodium ion	
NH_3	Ammonia	
$NiSO_4$	Nickel(ÎI) sulfate	
$NiCl_2$	Nickel(ÎI) chloride	
Ni	Nickel	
NC	Normally closed	
OC	Open-circuit	
OECD	Organisation for Economic Co-operation and Development	
OLED	Organic light emitting diode	
P_{in}	Incident power	mW
P_{MAX}	Maximum power	mW cm^{-2}
P	Power laser	W
PMII	1-Propyl-3-methylimidazolium iodide	
PB^-	1-Pyrenebutyrate	
PEC	Photoelectrochemical	
PV	Photovoltaics	
p-n	Positive-negative	
Pb	lead	
Pt	Platinum	
PEO	Polyethylene oxide	

PEDOT	Poly(3,4-ethylenedioxythiophene)	
PSS	Poly(styrenesulfonate)	
PDP	Plasma display panel	
PSD	Particle size distribution	
PC	Personal computar	
q	Elementary charge (q = 1.60217646 × 10^{-19} C)	C
R	Ideal gas constant (R = 8.314472(15) J K^{-1} mol^{-1}) or a resistance (Ω)	J K^{-1} mol^{-1} Ω or Ω cm^{-2}
R_{ct}	Charge-transfer resistance	Ω or Ω cm^{-2}
$R_{c/Pt}$	Charge-transfer resistance normalized by the amount of Pt used per deposited area	Ω µgPt
$R_{c,Pt}$	Charge-transfer resistance of a Pt CE	Ω or Ω cm^{-2}
$R_{c,graphene}$	Charge-transfer resistance of a graphene-based CE	Ω or Ω cm^{-2}
R_{CE}	Charge-transfer resistance at CE	Ω or Ω cm^{-2}
R_k	Recombination resistance	Ω
R_s	Series resistance	Ω or Ω cm^{-2}
R_w	Electron transport resistance	Ω
ref	Reference	
Red	Reduced species	
Ru	Ruthenium	
RGO	Chemically reduced graphene oxide	
S	Ground state of the sensitizer	
S*	Excited state of the sensitizer	
S^+	Oxidised sensitizer	

SC	Semiconductor or Short-circuit	
SCN	Thiocyanate	
Si	Silicon	
SEM	Scanning electron microscopy	
SnO_2:F	Fluorine-tin oxide	
SWNH	Single-walled nanohorns	
sp^2	Double-bond characteristic of graphite-based materials	
t	Time	s
T	Absolute temperature or Transmittance	K / ºC or %
ΔT	Relative transmittance	
TBA	Tetrabutylammonium	
TBP	*Tert*-butylpyridine	
TCO	Transparent conductive oxide	
TG	Thermogravimetric	
TGA	Thermogravimetric analysis	
T_g	Glass transition temperature	
TiO_2	Titanium oxide	
UV	Ultraviolet	
USD	American (USA) dollar	
V	Voltage	V or mV
$V(t)$	Voltage perturbation	V or mV
V_{MPP}	Voltage in the maximum-power point	V or mV
V_{oc}	Open-circuit photovoltage	V

V_0	Amplitude of the voltage signal	V
Vis or VIS	Visible ligth	
VB	Valence band	
WE	Working electrode	
$Z(t)$	Impedance	Ω
Z_0	Ratio between V_0 and I_0	Ω
Z'	Real part of impedance	Ω or Ω cm^2
Z''	Imaginary part of impedance	Ω or Ω cm^2
Z_C	Impedance of a capacitor	Ω or Ω cm^2
Z_{CPE}	Impedance of a constant phase element	Ω or Ω cm^2
Z_N	Impedance of a Warburg element of the Nernst diffusion of I_3^- in the electrolyte	μF or μF cm^{-2}
ZrO_2	Zirconium oxide	

Greek Symbols

Greek symbols	**Definition**	**Units**
$\Delta\eta$	Average relative increase percentage of the overall conversion efficiency	%
$\Delta\tau_{550nm}$	Average relative difference of transmittances measured at a wavelength of 550 nm	%
ΔR_{ct}	Average relative increase percentage of the charge-transfer resistance	%
η_c	Collection efficiency	%
η	Global efficiency of a DSC	%
$\eta_{grapheneCE}$	Global efficiency of a DSC with a graphene-based CE	%
η_{Pt}	Global efficiency of a DSC with a Pt CE	%
ϕ_{nj}	Injection efficiency	%
ϕ	Intensity of the incident light	μWcm^{-2}
ft	Firing time	s
λ	Wavelength	nm
v	Frequency or Laser scan velocity	Hz/s^{-1} or $mm\ s^{-1}$
τ_{μ}	Electron lifetime	s
τ_{550nm}	Transmittance measured at a wavelength of 550 nm	%
$\tau_{550nm,grapheneCE}$	Transmittance measured at a wavelength of 550 nm for a graphene-based CE	%
$\tau_{550nm,Pt}$	Transmittance measured at a wavelength of 550 nm for a Pt CE	%
φ	Phase angle	Degree

ω	Radial frequency	rad s^{-1}
ω_{max}	Radial frequency at the semicircle maximum	rad s^{-1}

CHAPTER 1

Introduction

The development of clean alternatives for the production of energy has suffered exponential growth during the recent years, positioning themselves as key technologies for the incoming future [1]. This development was spiked by the scientific, political and civil societies' concerns with the almost certain depletion of fossil fuels in the next decades [2] and its repercussions on the world economic model of sustained growth, along with the global warming problematic derived from the greenhouse effect caused by fossil fuel combustions. Within these renewable energy technologies, one of the most promising are the photovoltaic cells (PV) having a great growth potential during the next quarter of a century [3, 4]. Photovoltaics are one of the most efficient technologies for converting an almost endless source or power - solar energy - into electricity. On top of that, they are a low maintenance technology, are capable of ensuring a stable and continuous energy production that is sufficient to respond to the needs of an electric grid [5] and are responsible for releasing much less CO_2 emissions than any coal or gas power plant [4]. Although the photovoltaic industry is currently dominated by Si-based cells, an alternative technology called Dye-sensitized Solar Cells (DSCs) is now emerging due to its great low-cost, high energy conversion efficiency and environmentally friendly potential and aesthetic performance, which would result in a low-cost truly building integrated electricity production from solar radiation [6].

In the present chapter, it is reported the working principles of DSCs and its current major challenges; in more detail, it is addressed a DSCs' leak free sealing and the platinum-free use in the counter-electrode. Finally the motivations and main goals of the developed work are presented.

1.1. Energy paradigm

In this day and age the world is faced with a harsh reality: energy consumption keeps increasing at very high rates every year. Despite the efforts from the “industrialized world” that has stabilized their energy spending in the last decade, non-OECD countries such as China and India are now driving the total worldwide energy consumption due to their incredible economic growth - Figure 1.1 [7, 8]. In addition, if policies are not changed, the energy consumption rate is predicted to worsen from 2015 onwards. In 2011 alone, world primary energy consumption has grew by 2.5 % to approximately 148 000 TWh [8], with electricity consumption accounting for 20 055 TWh (~ 7.5 % – 8.0 %) [9].

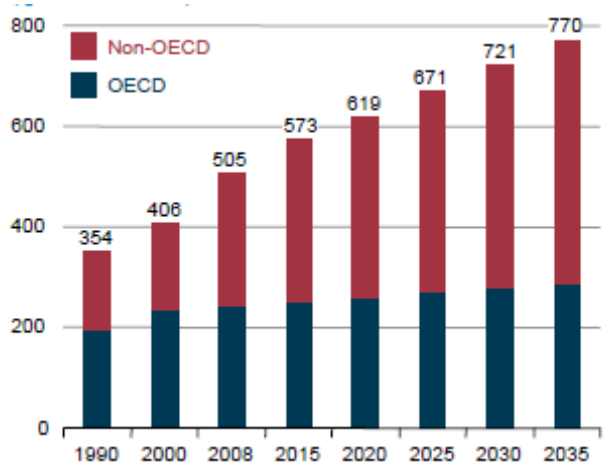

Figure 1.1 World energy consumption (quadrillion BTU) (adapted from [7])

This overwhelmed amount of energy spent each year has a dire effect on the environment as most of the currently used energy sources are fossil fuels that are heavy pollutants. Conversely, due to their scarcity, the economic viability for the extraction of such sources is being questioned. In the current economic model of sustained growth, affordable oil and natural gas are said to be depleted in 20 and 50 years respectively, and coal in 100 years [2]. The exhaustion of

these resources could also pose a serious threat to the national sovereignty of many countries. Owing to this reality, it becomes very clear that energetic alternatives are required. Renewable energy sources can be viewed as “infinite” power sources, a key for the survival of the modern society. As clean energy sources, they could provide answers to some of the major concerns faced by society: the increasingly energy consumption and the need for reduction of CO_2 emissions to atmosphere (as viewed by the Kyoto protocol). Concurrently it can be a way to assure long-term sustainability and security of the entire energy supply network [2, 10]. The study and implementation of energy production technologies from renewable sources has grown exponentially in the last two decades, being estimated an annual implementation growth of 2.6 % in the next 25 years [11]. In 2011, renewable energies (hydropower, biomass, wind, solar, geothermal, biofules) represented 16.7 % of global final energy consumption, supplying 20.3 % of global electricity demands. [12, 13] The European Union has been at the frontline of investment (under the EUROPE 2020 framework) with the goal of having 20 % of primary energy consumption produced from renewable sources by 2020.

Arguably the most renewable energy source is the Sun. Annually the total solar energy striking the earth’s surface is more than 1000 times the global primary energy consumption [2]. Even if only 1 % could be harvested that would still be enough to respond to the worldwide energy demand. In Portugal, for example, studies suggest that there is the potential of viable economic generation of 142 TWh/year of electric energy using solar power concentration technologies (with a power demand for electricity for 2050 estimated at 51 TWh/year) [2]. One of the ways to harvest that energy consists in converting directly the solar radiation into electricity using the photovoltaic effect. Photovoltaic (PV) devices are one of the most promising and “elegant” technologies for generation of electricity as they can be used anywhere in the globe, especially in regions with a latitude lower than 65º. This is of particular relevance for the poorer countries where grids are often very underdeveloped.

The CO_2 emissions released by photovoltaic devices during their lifetime cycle are roughly 10 and 20 times lower than gas or coal powered plants respectively [4]. The photovoltaic industry is still somewhat underdeveloped, despite the incredible exponential implementation growth exhibited by PV. During the 5 year period of 2006-2011, PV's average annual growth was 58 %, the highest for any renewable energy technology, representing in 2011 approximately 70 GW of total installed capacity and generating more than 100 billion USD per year [12, 13]. This growth rate is similar to the one wind power generation (currently second most used renewable energy technology in the European Union, just behind hydropower [2]) displayed 10 years ago [10], positioning itself as a relevant electricity supplier in the near future. The photovoltaic solar cells market is currently predominately based on mono and polycrystalline silicon. Commercial photovoltaic technologies comprise the so-called first generation solar cells (mono and polycrystalline silicon) and second generation solar cells, also called thin-film, such as amorphous silicon (a-Si:H2, a-Si/μc-Si), copper indium diselenide (CIS), copper indium gallium selenide (CIGS) and cadmium telluride (CdTe). Third generation PV solar cells research emerged in the turn of the 20's century as an answer to high silicon prices, metal-based thin-film technologies environmental/scarcity problems as well as poor energy efficiency of the second-generation PV solar cells [14, 15]. The new generation of photovoltaic devices is based on the idea of using nanotechnology and fairly abundant/environmentally friendly raw materials for lowering production costs and increase usability. It includes nanocrystalline solar cells, polymer solar cells and dye solar cells. Most of the third generation cells are not yet being commercialized. When comparing with first generation PV cells that started commercialization in the 1950's and second-generation cells in the late 1970's, it becomes clear that the third generation PV solar cells comprise fairly of young technologies that cannot yet compete with first and second generation cells. However, for some of them market entrance is forecasted for the near future. For example, the roadmap of the EUROPE 2020

framework, predicts that dye solar cells should become commercially available in 2015 [2]. Additionally, the market for dye-sensitized solar cells will grow up to 290 million USD by 2023, according to market projections by IDTechEx [16].

Although average PV module cost has been significantly reduced in the last decades from 100 USD / $Watt_{peak}$ to ~ 2 USD / $Watt_{peak}$, [17] due to technological innovations, economies of scale associated with large production yields and a large drop of the silicon price, energy costs are still higher than for other renewable energy technologies (for example, 20-40 cents of dollar/kWh for PV vs. 5-10 cents of USD / kWh for hydropower) [12, 13]. This has obliged governments to issue feed-in tariffs in order for PV to compete with the major electricity production technologies (coal and gas powered plants). On the other hand, in the last few years, the entrance of PV Chinese companies into the energy market has driven the price of PV modules even further down, with some modules of either mono or multi-cSi as well as for some thin film modules, being priced below USD 1 / $Watt_{peak}$,[13] a threshold that is seen as critical for achieving grid parity (i.e. cost at which is competitive with coal or gas-fired generation without government aid). In fact, in less than 10 years, the once lead manufacturer *Sharp*, is now 6^{th} in the market share, where 4 of the 5 top manufacturers (*Suntech*, *Yingli Solar*, *Trina Solar* and *Sungeon Solar*) are Chinese; the exception is the American *First Solar*. As a consequence, these low prices have caused a tremendous effect. In some countries, like Germany and Italy, using retail PV modules prices (including non-hardware balance of systems and installation costs), and assuming that one uses all the electricity produced by the PV system, i.e., that the PV system is disconnected from the energy grid, it is already possible to pay-back these systems in less than 10 years, without feed-in tariffs [18]. This paradigm shift as even allowed, in some locations, for the cost of PV to have fallen below that of nuclear power. Furthermore, it is expected that traditional energy sources will become more expensive, aggravated by the new carbon tax on CO_2 emissions proposed by the

Kyoto protocol. As a result PV solar cells have the potential to become a true widespread mass technology, displaying a great cost-reduction potential and a diversity of applications.

1.2. Dye-sensitized solar cell

The photovoltaic effect can be generically described as the creation of electrical current upon exposure to light; this effect was first observed by Alexandre-Edmond Becquerel in 1839. He noticed that when two platinum plates were placed in an illuminated solution of a metal halide salt, an electric current was created. Years later, in 1873, Vogel discovered that silver halide emulsions that had been sensitized with a dye possess extended photosensitivity to longer wavelengths [19]. These works, together with the report by Moser a few years later describing the dye-sensitized effect, and the theory of the photovoltaic phenomenon by Einstein, paved the way for the study of photoinduced charge separation phenomena that occurs in a liquid-solid interface. However, it was only after the studies carried out on the electrochemical and photoelectrochemical effects on semiconductor-electrolyte interfaces by Gerischer in the late 1960's that using dye-sensitized photoelectrochemical cells to convert solar energy into electricity was endeavored. Still, the efficiencies of such devices were very low (< 1 %), due to poor light harvesting and dye instability. That is until 1991 when Brian O'Regan and Michael Grätzel were able to describe a bulk heterojunction dye-sensitized solar cell with a solar efficiency conversion over 7 % [6]. The novel device was based on a high surface area semiconductor comprised of nanocrystalline nanometer-sized TiO_2 particles on to which newly-developed organometallic dyes with very high charge-transfer electrons were attached. Although efforts have been made since then, the state-of-art dye-sensitized solar cell (DSC) has only been capable of improving to a proved efficiency of 11.9 % (measured at standard reporting conditions - Air Mass (AM) 1.5 global

sunlight, 100 mW cm^{-2}, 298 K) for an aperture area of 1 cm^2 and 9.9 % for a sub-module with a 17 cm^2 area. [20]. However, Michael Grätzel from EPFL, Switzerland, reported recently a DSC device with an energy conversion efficiency of 12.3 % [21], under standard conditions, and rumours circulate that he has just reached 15 % efficiency, also under standard conditions, though the corresponding publication is still under submission process. There are studies on the area of nanotechnology and applied molecular chemistry suggesting that DSC efficiencies can be improved up to 20 % [19, 22, 23]. Efficiency could be improved by modifying the electrolyte's redox mediator thus improving charge transfer and maximum photovoltage [24, 25], by morphologically modifying the semiconductor [25], or developing new dyes capable of absorbing light in a broader range of the solar spectrum, thus harvesting more energy [25]. Nevertheless, there is still a long way to pave.

Despite having lower efficiencies than first and second generation photovoltaic solar cells [26], DSCs are known to have several advantages when compared with other PV technologies: i) the raw materials necessary for the components of a DSC are abundant, with low toxicity and having a low cost [27-29]; ii) less complexity of the manufacturing process. This reflects on the final cost of a photovoltaic module. Presently a DSC module costs approximately 2.5-3 USD / $Watt_{peak}$ [27, 28], with a prognostic of lowering costs to values around 0.5 USD / $Watt_{peak}$ concerning the production of 8 % – 10 % efficiency modules and for a yearly production of 100 MW [28, 29]; iii) better performance under more demanding atmospheric conditions with electricity production being hardly affected by temperature - from 0 ºC up to 65 ºC [30]; iv) as efficiency is roughly the same for both direct and diffuse light conditions, daily electricity production is higher than first and second generation PV cells by ca. 40 % [31, 32]; v) greater diversity and versatility of applications due to their attractive color and design allowing for tunable customer specifications and enabling its use for example in truly building integrated applications (BIPV) [33]. In face of all this, considerable efforts have

been carried out to scale-up this type of solar cell technology into a commercial device.

However, the development of large area DSC modules has yet to be fully accomplished due to a series of problems that must be tackled if they are to become a truly cost-competitive alternative to conventional photovoltaic devices in the energy market. This work is intended to contribute to solve some of those problems, making the scale-up process progress to a stage very close to commercialization. Mainly this work focuses on two key points:

- The replacement of the catalyst material used for the photoelectrochemical reaction that takes place in the DSC. Traditionally it is used platinum, a scarce and very expensive metal. However, there are studies indicating that certain carbon materials can be used instead with comparable performances [34-37].

- The development of new sealing methods for the encapsulation of the DSCs devices. Currently there are no technological solutions that can assure the required long stability of DSCs' modules (25 years), particularly when subjected to more adverse atmospheric conditions (i.e. operating temperatures from -40 °C up to 85 ºC).

1.2.1. Structure and materials

The schematic of a typical dye-sensitized solar (DSC) cell is shown in Figure 1.2. A typical DSC consists of two glass substrates both covered by a transparent conductive oxide layer (TCO). One of such substrates is also covered by a catalyst material, while the other has attached a layer of a crystalline semiconductor that is in turn covered by a monolayer of dye molecules. An electrolyte sits encapsulated between both substrates. In general the best efficiency is obtained for DSCs illuminated from the front side

(photoanode), although back illumination is also possible for cells with semi-transparent counter-electrodes.

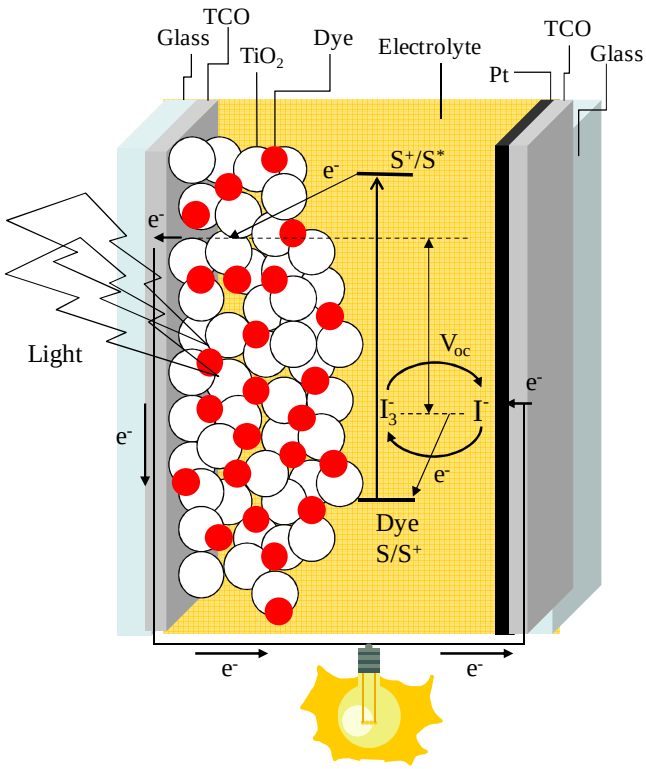

Figure 1.2 Schematic structure and principle of operation of a typical dye-sensitized solar cell. The porous semiconductor (TiO_2) is covered with a monolayer of dye molecules and the counter-electrode is coated with a thin layer of a catalyst material (Pt). An electrolyte sits between these structures that are deposited onto the surface of glass substrates covered with a transparent conductive oxide layer (TCO).

In the traditional p-n junction solid state PV cells, the conversion of sunlight into electricity involves light absorption and charge separation in the same element; in DSCs those processes are differentiated - Figure 1.2 [19]. The photon absorption and creation of the pairs electron-hole are carried out by the dye molecules attached onto the semiconductor, whilst the transport of charge carriers takes place both in the semiconductor and in the electrolyte. As a result,

many different types of materials are used for the fabrication of a DSC and many fields of science must come together to fully realize its potential.

Supporting substrates

Both top and bottom substrates are typically made of glass in order for the solar energy to be able to strike the photosensitizer molecules. However, transparency is only mandatory in one of them. Nevertheless, when both substrates are transparent, it offers added value to numerous applications (facades, windows, roof panels, etc.). For high performance cells, along with transparency (transmittance higher than 80 %) the supporting substrate must also have very low sheet resistance (< 15 Ω/sq). Traditionally a transparent conductive oxide layer (TCO) is deposited on the top of the glass surface in order to extract electrons and transport them onto a outer circuit. One of the most used TCO in electronic industry is indium-tin oxide (ITO). However, ITO's resistance increases dramatically above 450 ºC in air, the temperature required for the preparation of the photoelectrode [38]. As an alternative, fluorine-doped tin oxide, SnO_2:F (FTO) is used. Efforts have been made to find alternatives that are lightweight and flexible. Among those are conductive polymer films (indium doped tin oxide-coated polyethyleneterephtalate - ITO-PET or polyethylenenaphtalate - ITO-PEN) and metal substrates (stainless steel and titanium sheets) [39, 40].

Semiconductor (Photoanode)

The semiconductor is a part of the photoanode of a DSC, usually placed in the front substrate (the one receiving sunlight). The semiconductor holds the dye molecules, accepts the electrons from the dye and transport the electrons towards the TCO (and consequently onto the external circuit). Usually semiconductor oxides are used, because materials such as Si, InP, GaAs and

CdS are susceptible to photocorrosion when placed under irradiation in a solution. The choice material for DSCs is normally titanium oxide (TiO_2) as it has good chemical and mechanical stability under visible light when placed in a solution, is non-toxic and inexpensive [41, 42]. The correct crystalline form of TiO_2 is also essential. Titanium dioxide exists in three different crystallographic configurations where the most effective is anatase due to its larger band gap (~3.2 eV), stability and electronic conductivity and position of the conducting band. The large band gap prevents the semiconductor to absorb visible light. This makes it more stable as the generation of holes by band gap excitation (that would act as oxidant species) is prevented [43]. The TiO_2 layer is created by coating a paste of TiO_2 nanoparticles by doctor-blading or screen-printing into the TCO substrate an then sintered at temperatures above 450 ºC [44]. This sintering stage is important to allow the formation of electronic pathways for the photogenerated electrons until the TCO surface. Because the film is comprised of nanoparticles (10 – 30 nm), the formed structure is very porous, where the actual surface area is several times higher than its apparent area, in the range of 50 - 100 $m^2 \cdot g^{-1}$ [45]; this way, the amount of dye molecules adsorbed onto the surface of the TiO_2 particles, in a monolayer, is very high (~ 10^{-7} $mol \cdot cm^{-2}$) and consequently the light absorption efficiency is also very high. The appropriate photoelectrode pore size network (average pore size of ca. 10 - 20 nm) is also relevant, as the electrolyte species must be able to easily diffuse for regenerating (reduce) the dye molecules [45].

The maximum thickness of the photoelectrode is conditioned by the poor electronic conductivity of TiO_2 and optimized dyed photoelectrodes are semi-transparent. For increasing the photoelectrode ability to harvest light, a light-scattering layer is currently employed. In this case a second layer of larger TiO_2 (200- 400 nm) is added on top of the first layer (opposite photoelectrode side to the light source), effectively scattering incident light and redirecting unused photons back into the semiconductor [44, 46]. Other ways of increasing performance consists in adding thin layers of semiconductors that are more

negative conductors than TiO_2 (such as Al_2O_3 and MgO or even very thin and compact TiO_2 layers), which would work as insulators. This would allow favouring electronic injection while decreasing charge transfer from the TCO to the electrolyte, thus increasing overall efficiency [47, 48].

Dye (Photosensitizer)

As previously mentioned, in a DSC light absorption and electron generation are responsibility of the dye molecules chemically bonded to the surface of the semiconductor. Although first introduced 20 years ago, the researchers are still using sensitizers based on bipyridyl complexes of ruthenium (Ru) [49]. The main advantages centre on their high conversion efficiency of solar energy into electricity, low toxicity, photostability (enduring at least 10^8 redox cycles, corresponding to ca. 20 years of operation) and high spectral absorption range (300 nm – 900 nm). A typical example of a Ru complex sensitizer is *cis* - bis (4,4'-dicarboxylate-2,2'-bypiridine) ruthenium (II), or N3 dye [49]. Binding to the TiO_2 surface is achieved from the carboxylic groups by either carboxylate bidentate coordination or ester bonding (-C(=O)-), which provides excellent stability, along with effective electron injection from the Ru complex into the TiO_2. Its isothiocyanato (NCS) groups enhance the response to visible light. A similar Ru complex sensitizer is the black dye (tris(cyanato)-2,2',2''-terpyridyl-4,4',4''-tricarboxylate) Ru(II)). Absorption of light is attributed to the metal-to-ligand charge-transfer transition. The highest occupied molecular orbital (HOMO) are d-orbitals of the Ru metal, while the lowest unoccupied molecular orbit (LUMO) are ligand's orbital. Besides enhancing the response to visible light, the negative shift caused by the isothiocyanato (NCS) groups, contribute to electron acceptance from reduced redox ions. The excited state of these Ru complex dyes is situated just above the conduction band of the semiconductor, which is sufficient for electron injection. Likewise, their ground state is situated slightly below the redox potential of the electrolyte, guaranteeing a proper

regeneration. The most commonly used Ru complex-based dye is the N719 dye due to its unparalleled efficiency performance [20, 50]. The N719 dye is a tetrabutylammonium (TBA) salt based on the N3 dye - Figure 1.3, where two protons are replaced by two cations.

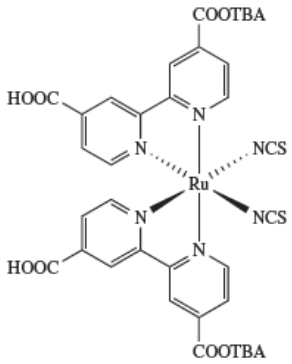

Figure 1.3 Molecular structure of the N719 dye.

Other dyes have been considered due to the scarcity nature of the ruthenium [28, 51]. Organic dyes such as cyanines, phtalocyanines, merocyanines and porphyrins are seen as viable alternatives as their cost is lower than ruthenium-based dyes; actually, the efficiency of porphyrins-based DSCs could surpass that of the N719 in the near future [21].

Electrolyte

The electrolyte is placed between the two substrates (photoanode and counter-electrode). Typically it is used a liquid electrolyte that is able to penetrate the porous network of the TiO_2 photoanode. The electrolyte is comprised of a redox couple in a matrix. The redox couple is responsible for regenerating the oxidized dye (after the formed electron had been injected into the semiconductor) and carry the formed holes (positive charges) towards the counter-electrode. The most commonly used and the only commercial available

are iodide-based electrolytes, having a redox couple of triiodide / iodide (I_3^-/I^-). When combined with ruthenium-based dyes the DSC's voltage is maximized because its redox potential is energetically favoured with such dyes [52]. Another reason for its use is that it does not compete with the Ru-based sensitizer for absorption in the visible spectrum and it is reversible at counter-electrode side. Because the electrolyte is responsible for the mass transport of the charge carriers, the overall efficiency of a DSC is strongly affected by its properties [53]. The electrolyte has a great influence in the maximum current density delivered by the cell as it is limited by the reduction kinetics of the I_3^- at the CE. It also strongly influences the dark current reaction kinetics and determines the charge transport rate in the electrolyte medium and in the pores of the semiconductor. For example, the viscosity of the solvent directly affects the ion conductivity and thus the overall performance [53].

Typically a liquid electrolyte is comprised of a mixture of iodides (LiI, NaI or KI) with imidazolium-derivate iodides and I_2, dissolved in nonprotonic solvents (e.g. propionitrile, acetonitrile, methoxypropionitrile). The DSC's performance can be negatively affected by cations Li^+, Na^+ and K^+, as they can adsorb onto the TiO_2 surface lowering its conduction band level. Room temperature molten salts (ionic liquids) are used to extend the longevity of the DSCs. Ionic liquids are often part of the electrolyte composition due to their good thermal and chemical stability, nonflammability, negligible vapour pressure, high solubility for organic or inorganic materials and high ionic conductivity [54]. High viscosity electrolytes are also employed for stability issues although yielding less efficient cells.

Despite its superior performance, iodide electrolytes have some limitations such as their corrosive nature and complex redox chemistry [55]. Owing to that, ferrocene and cobalt-based electrolytes have been recently developed and paired with suitable dyes. These redox couples have more positive redox potential edges that translate in extended photovoltages, thus yielding higher-efficiency DSCs [21, 55].

Catalyst material (Counter-electrode)

Platinum (Pt) is the most used material for the reduction reaction for the counter-electrode side, due to its high electrocatalytic activity. The deposition method onto the TCO substrate influences the overall performance, with screen-printing and drop-casting yielding the best results. Typically the load of Pt deposited is very low (5 – 100 µg cm^{-2}) and as a consequence the electrode becomes very transparent [56-58]. Due to its scarcity and high-cost it is preferable to find alternatives that are abundantly available. Previous studies have tried to reproduce the Pt's catalytic activity by using different carbonaceous materials – carbon black (CB) (stand alone or with graphite powder) [35, 36, 56, 59, 60], activated carbon [36] or single [34] or multi-wall carbon nanotubes [61-63]; these materials are low cost, resistant to corrosion and have good electrocatalytic activity towards the reduction of triiodide. The active sites responsible for catalysis are located at the edges of the carbon crystals [56] and their performance is also strongly affected by the available surface area for reaction [35, 36]. In order for these carbononaceous CEs to have comparable efficiencies to Pt CE, they have to be several µm-thick [35, 56] and thus opaque.

Amidst the carbon materials, graphene has emerged as potential catalyst for DSC. Graphene, the elementary structure of graphite, is an atomically thick sheet composed of sp^2 carbon atoms arranged in a flat honeycomb structure [64]. It has two faces with no bulk in between, therefore reagents can attach to both graphene faces. There is a great interest on graphene because of its ultrathin geometry (is the thinnest known material) and properties such as high charge carrier mobility, excellent thermal conductivity and high mechanical strength (the strongest ever measured) [64]. Up until now graphene has attracted considerable attention as an alternative to the transparent conducting oxides. The more traditionally used ones are indium-tin-oxide and fluor-doped

tin oxide and they are typically applied in a vast array of photoelectronic applications such as liquid crystal displays, organic solar cells, organic light emitting diodes (OLED) and fiber optic communications devices. Graphene electrodes possess the potential to have simultaneously high electrical conductivity and optical transparency (thus fulfilling the requirements for electrodes of the previously mentioned applications), while allowing for the use of flexible substrates, etching and high temperature processing. Moreover, when comparing with other promising carbon structures alternatives, such as carbon nanotubes, graphene is a cheaper and practical alternative [65-69].

The most promising path for producing graphene related compounds, from both scale-up and cost perspectives, is starting from graphene oxide (GO) obtained by a chemical oxidation method and later reduce it either chemically or thermally [70, 71]. The reduced graphene oxide (RGO) possesses some oxygen-containing functional groups (–OH and =O) on the planes and –COOH and carbonyl groups decorating the periphery of the planes [72], that, along with lattice surface defects produced during the oxidation of the graphene sheets, are believed to be responsible for the electrocatalytic activity [35, 73-79]. Owing to that, its use as a CE material is favoured in opposition to perfect, fully-reduced and defect-free, graphene. Additionally, graphene has an exceptional specific high surface area and because it has a higher oxidation potential than Pt, it should provide more resistance to electrocorrosion [73].

So far, simultaneously transparent and very efficient CEs comprised solely of graphene have not yet been obtained. Hong *et al.* [75] have used 1-pyrenebutyrate (PB^-) functionalized graphene dispersed in an organic matrix composite of PEDOT: PSS yielding a very transparent CE with a relative difference in efficiency of less ca. 30 % than that of a Pt CE. The polymer was used to act as the conductive support with graphene being the responsible for the catalysis. Polymer matrixes are often used to avoid agglomeration of powder reduced graphene sheets, but they prevent the free flowing of electrons

[77]. Choi *et al.* [80] used an hybrid structure of graphene and multi-walled carbon nanotubes (GMWNTs) to produce a 3 % efficiency DSC.

Zhang *et al.* [76] used an ethylcelulose and terpineol printable paste, containing chemically reduced GO, to fabricate a CE with an efficiency of 2.94 %, after annealing it at 450 ºC in air for 15 min. Roy-Mayhew *et al.* [73] have prepared CEs made of graphene functionalized with oxygen-containing groups (produced from a thermal exfoliation method) with the aid of a mixture of surfactants and PEO (polyethylene oxide). After carbonizing the electrodes at 350 ºC in air, the opaque CE yielded a ca. 90 % relative difference in efficiency compared to a Pt CE. Huh *et al.* [81], reported a CE made from partially reduced graphene oxide (reduction obtained by annealing the GO at 250 ºC for 2 min in air) resulting in a ultrathin film with good transparency but with an efficiency of 2.30 %, ca. 40 % of that of a Pt CE. Very recently Kavan *et al.* [82] have used commercially available graphene to fabricate a CE by drop-casting, without any annealing. The produced CE exhibited a transmittance of ~ 85 % (λ = 550 nm) and an efficiency of 5 %, a 72.5 % relative efficiency compared to a Pt CE. Choi *et al.* [83] have used an electrophoretic technique to deposit chemically RGO, followed by annealing at 600 ºC for 1 min, to fabricate a CE with a 85 % transmittance (λ = 550 nm) and a 2.3 % efficiency. From the work developed by other authors up to this point, it seems that the best results are achieved when RGO (typically obtained by chemical reduction) is used.

Sealing

In order to prevent leakage of electrolyte and evaporation of the solvent (when applied) into the exterior, it is needed to seal the components of a DSC. Additionally the sealing material aids into preventing moisture to enter the cell and damage its inner components. This sealing material must also be

chemically stable against the electrolyte components (solvents and redox mediator) and stable under cyclic temperature and radiation variations.

Presently, lab-scale size DSCs are sealed using commercial polymeric materials (based of ethylene and acrylic acid), such as *Surlyn*® and *Bynel*® *(Dupont)*, which are photoresistant and have poor electric conductivity. Sealing occurs using a combination of pressure (80 – 900 psi) and temperature (80 ºC – 120 ºC). If a DSC would to be subjected to this temperature range or higher, for more than one minute, it could cause the degradation of the photosensitizer [84]. A frequently used solution to preserve the dye is to introduce it into the cell after the sealing stage takes place trough recirculation [85-87]. However such procedure is likely to reduce the efficiency of the DSC, due to adsorption occurring in a non-uniform and non-monolayer fashion. Nevertheless, the biggest problem with this type of sealants relates to the fact that they lose their mechanical properties when placed under the typical operation temperature experienced by a photovoltaic module, 60 ºC – 85 ºC [87]. As a result, the polymeric material no longer is capable of providing a tight seal to the cell. The DSC then allows the diffusion of moisture and oxygen into its interior, causing the degradation of the electrolyte and of the photosensitizer respectively [88-90]. In some cases, leakage of electrolyte can even occur, compromising likewise the normal operation of the cell [88-90].

More recently it has been demonstrated to be possible to seal DSCs using glass frits (glass powder dispersed into an organic matrix). This is a type of glass-on-glass sealant that possesses very stable thermal, chemical and mechanical properties [28, 86, 91-94]. Nonetheless, the sealing procedure requires relatively high temperatures (400 ºC – 600 ºC) in order for the sealing material to fuse properly [28, 86, 93]. Owing to that, it is mandatory to introduce the dye afterwards. These high temperatures can be seen as problematic, as the upper threshold limit for DSC's components is ca. 500 ºC (except for the photosensitizer that has a much mower threshold, ca. 100 ºC). Some frits, in order to lower their fusing temperature, have in their composition

lead, which yields metallic ions that contaminate the electrolyte and the catalyst in the counter-electrode side [92]. More recently, new lead-free frits have emerged with fusion temperatures of ca. 400 ºC – 500 ºC [86, 95]. Nevertheless, the high sealing temperatures still present themselves as an issue for scaling-up and module production, as they limit the overall performance of the DSCs.

In order to overcome the current limitations regarding DSC's long-term stability, a new sealing method has been devised - Figure 1.4 [96]. This method is based on a laser-assisted glass frit bonding technique, where a glass frit (chemically and mechanically stable) is employed as the sealing material. The fusing of the frit and the glass substrates is carried out using an adequate laser beam. Both, the laser beam and frit, fire and absorb in the near infrared spectrum respectively (ca. 1100 nm), whilst the TCO-covered glass substrates are transparent in that region, thus enabling a localized heating and minimizing heat deterioration on the DSC's components. Other sealing techniques involve using UV-cured resins or secondary (doubling) seals [90, 97].

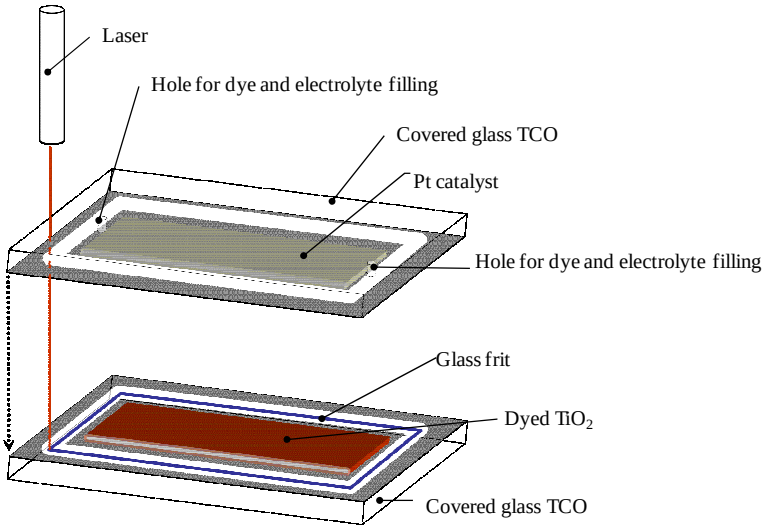

Figure 1.4 Schematic of the method devised for sealing a DSC by the use of a laser-assisted glass frit technique (adapted from [38]).

1.2.2. Energy diagram and working principle

The working principle of a DSC is based on the kinetic of the electron transfer reactions that takes place between the several components. The efficiency of a DSC is predominantly determined by four energy levels of the components: the excited state (corresponding to the highest occupied molecular orbital - HOMO) and the ground state (lowest occupied molecular orbital – LUMO) of the sensitizer, the redox potential of the mediator in the electrolyte and the Fermi level of the semiconductor (TiO_2). The energy diagram and electron transfer paths of a DSC is shown in Figure 1.5.

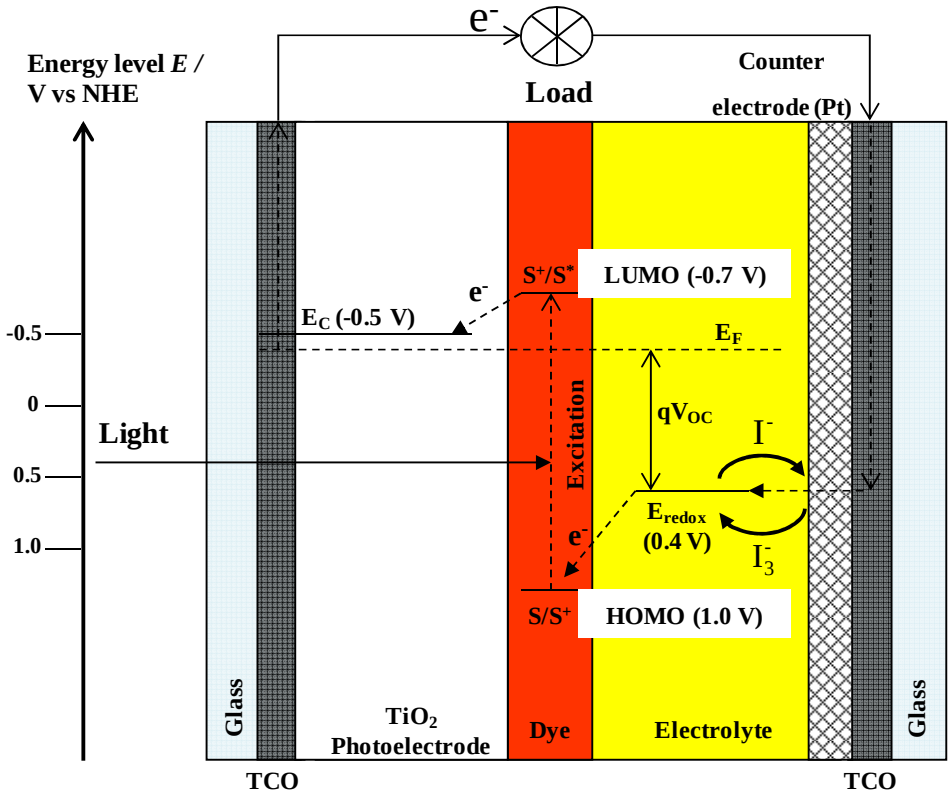

Figure 1.5 Schematic energy diagram and electron transfer paths of a DSC. The energy values for typical DSC's components are displayed. Dotted lines (-->) represent the electrons transfer pathway.

As previously mentioned, in a DSC, charge separation and charge transport occurs in different components and is separated spatially. The conversion of photons into current obeys to the following steps:

1. The photosensitizer that is adsorbed onto the semiconductor's (TiO_2) surface absorb incident photon flux. A dye electron is excited from the ground state (S) to the excited state (S*) due to its metal-to-ligand charge-transfer (MLCT) complex.

$$S + h\upsilon \rightarrow S^* \tag{1.1}$$

2. The excited electrons are rapidly injected into the conduction band of the semiconductor (TiO_2), yielding excitons (excited electrons) and subsequent charge separation, resulting in the oxidation of the photosensitizer (S^+).

$$S^* \rightarrow S^+ + e^-_{CB,TiO_2} \tag{1.2}$$

3. The electrons that were injected into the conduction band diffuse across the semiconductor (TiO_2) towards the external circuit, where they perform electrical work. They are then directed onto the back contact reaching the catalyst-covered (typically Pt) counter-electrode.

4. The oxidized redox mediator (I_3^-) that has diffused through the electrolyte towards the counter-electrode, is reduced (to I^-).

$$I_{3^-} + 2e^-_{CE} \rightarrow 3I^- \tag{1.3}$$

5. The reduced redox mediator (I^-) travels across the electrolyte and yields electrons to the oxidized phtotosensitizer regenerating it to its ground state, and becomes oxidized (I_3^-), thus closing the cycle.

$$2S^* + 3I^- \rightarrow I_3^- + 2S \tag{1.4}$$

Overall electrical work is performed without any chemical transformation. From this cycle it becomes clear that the DCS's negative pole is at the semiconductor side, while the positive pole is at the counter-electrode side.

Under normal operating conditions, i.e. production of electrical current (flow of electrons from the photoanode side into the counter-electrode side), the DSC is said to be operating under reverse bias. Apart from the forward electron transfer and ionic transport processes, loss processes can occur in a DSC - Figure 1.6:

6. Recombination of injected electrons in the semiconductor (TiO_2) with oxidized photosensitizers.

$$S^+ + e^-_{CB,TiO_2} \rightarrow S \tag{1.5}$$

7. Decay of photosensitizer from its excited state to its ground sate.

$$S^* \rightarrow S \tag{1.6}$$

8. Recombination of injected electrons in the semiconductor (TiO_2) with the oxidized redox mediator (I_3-).

$$I_{3^-} + 2e^-_{CB,TiO_2} \rightarrow 3I^- \tag{1.7}$$

It should also be mentioned that because TiO_2 has an energy bandgap of ~3.2 eV (corresponding to a wavelength of 390 nm), it does not absorb any visible light. The direct absorption of ultraviolet light is unwanted as it creates highly reactive holes in the TiO_2 valence band, thus promoting undesired electron recombination with the redox mediator present in the electrolyte and loss of efficiency – reaction (1.7).

The thermodynamic maximum energy efficiency of a DSC is 33 %, considering no overvoltages and harvesting photons up to 1.1 eV [23]. However, based on available materials this value drops to 20.25 % considering that the loss-in-potential is only 0.4 eV and that an optical bandgap of 1.31 eV (940 nm) is possible [23]. Efficient DSCs must obey to a series of assumptions. The generated photocurrent depends on the energy gap between the HOMO and LUMO of the photosensitizer (similar to the energy band gap in inorganic semiconductor materials). The smaller this gap, the larger the photocurrent will be, as the long wavelength region of the solar spectrum will be used.

Additionally the LUMO level must be sufficiently negative with respect to the semiconductor (be above the conduction band of the semiconductor), for electrons to be injected rapidly before they can have the chance to return to the HOMO level. Time-resolved laser spectroscopy measurements are used to study the kinetics of the reactions that take place inside the DSC while producing electricity. Reaction kinetic measurements have shown that the injection rates are higher than 10^{12} s^{-1}, while decay to ground state rates are ca. 10^{9} - 10^{3} s^{-1} - Figure 1.6 [22]. The electronic coupling between the photosensitizer LUMO level and the accepting states of the semiconductor controls the rate of electron injection [98, 99].

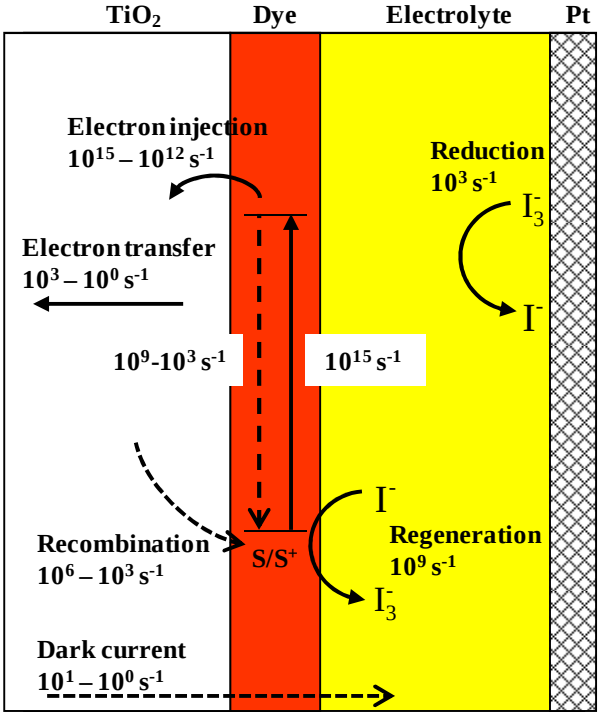

Figure 1.6 Schematic diagram of the kinetics of the electron-transfer processes at the different interfaces in DSCs. Full lines (→) represent forward electron transfer; dotted lines (-->) represent electron pathways losses (based on the electron flux of an electricity producing cycle).

The redox mediator in the electrolyte is responsible for the regeneration of the oxidised photosensitizer. In order for the dye to accept electrons effectively, the redox potential of the redox mediator (I_3^-/I^-) must be more positive (be above) than the HOMO level of the dye. The recombination rate of the of injected electrons in the TiO_2 with the oxidized dye – reaction (1.5) was found to be smaller (10^6 - 10^3 s^{-1}) than the dye regeneration by the redox mediator (10^9 s^{-1}), driving the electron flux in the correct direction [22]. Additionally, this difference of levels between the LUMO and the TiO_2, and the HOMO and the redox couple I_3^-/I^- must be higher than 200 mV in order for the electron-transfer reactions to take place efficiently [42]. However, to avoid an overloss of photovoltage, the overvoltage in all interfaces should be as small as possible. In particular the overvoltage required for the I_3^- reduction at the counter-electrode (difference between the redox potential of the redox mediator and HOMO level of the photosensitizer) must be as small as possible. The photovoltage of the DSC is developed between the potential of the redox mediator in the electrolyte and the Fermi level of the semiconductor. In a case of a DSC using a TiO_2 semiconductor and a I_3^-/I^- redox couple, the maximum voltage is expected to be ca. 0.9 V (-0.5 V for TiO_2 and 0.4 V for I_3^-/I^- versus normal hydrogen electrode (NHE) - Figure 1.5). Losses of photovoltages can also occur due to a change in the Fermi level of the semiconductor, as it depends on type and concentrations of the species present in the electrolyte. The specification of the electrolyte can also contribute to lower the generated photocurrent by increasing the recombination rate of electrons in the TiO_2 with the dye – reaction (1.5). The electrolyte can even cause a generation of current limited by diffusion, if the I_3-concentration is not high enough as to provide enough recombination centres for the electrons at the counter-electrode. However, simultaneously, it should not be too high, as this increases the recombination of the holes in the electrolyte (I_3^-) using electrons that are transferred along the TiO_2 structure – reaction (1.7). Indeed, this mechanism that takes place at the semiconductor/electrolyte interface (dark current) is the most significant

pathway loss in a DSC as it is a competing process with the I_3^- reduction [42]. Furthermore catalysts are deposited at the counter-electrode in order to reduce the charge transfer resistance in comparison with the one experienced by the exposed FTO layer at the photoanode side.

1.2.3. Characterization and performance

_I-V_ characteristics of a solar cell

The performance of a DSC can be accessed by measuring the current-voltage (*I-V*) response of the device, also known as the characteristic curve. The *I-V* characteristic curve gives a measure of the cell's overall solar energy-to-electricity conversion efficiency, η. The electrical parameters that are important to determine the cell's efficiency (η), are the short-current density (J_{sc}), the open-circuit voltage (V_{oc}) and the maximum power point (P_{MAX}) and their respective voltage and current density (V_{MPP}, J_{MPP}). The J_{sc} is a function of the intensity of the irradiation light. The V_{oc} is given by the difference between the potential of the redox mediator in the electrolyte and the Fermi level of the semiconductor. The P_{MAX} represents the highest power output of the cell when illuminated, and is a product of the current density and voltage – Figure 1.7. Frequently, the current, *I*, of a cell is related to its active surface area in order to obtain the current density (*J*) and it is plotted against voltage, being denominated as a *I-V* curve. A typical *I-V* curve is shown in Figure 1.7.

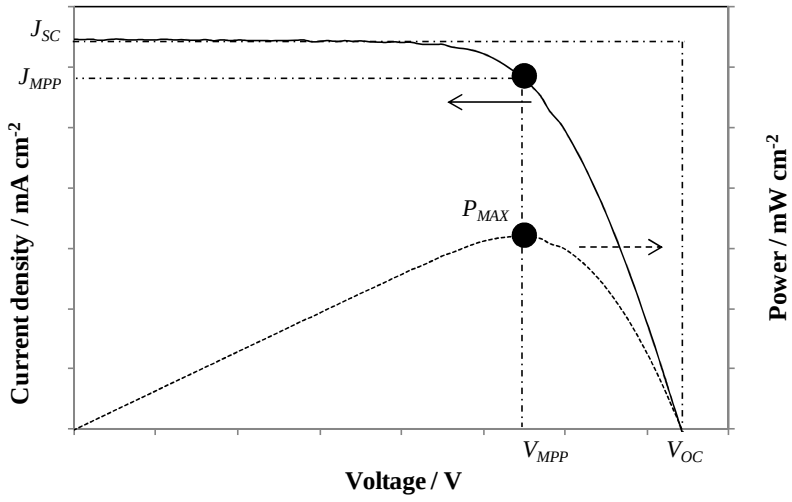

Figure 1.7 Typical *I-V* curve of a DSC (solid line) and respective power curve (dash line). Inset is also represented the maximum power point of operation.

The efficiency is calculated as the ratio between the maximum power generated by the cell and the power of the incident irradiation, P_{in}.

$$\eta = \frac{P_{MAX}}{P_{in}} \tag{1.8}$$

The maximum power is related to the so called fill factor (*FF*). Fill factor is a representation of the actual power delivered by the cell in opposition to the theoretically maximum, and expresses the overall resistances/losses taken place in the system:

$$FF = \frac{V_{MPP} J_{MPP}}{V_{oc} J_{sc}} \tag{1.9}$$

Efficiency can therefore be calculated trough the following expression:

$$\eta = FF \frac{V_{oc} J_{sc}}{P_{in}} \tag{1.10}$$

I-V curves are typically obtained with a white light irradiation spectrum, under standard conditions of AM 1.5, incident light intensity of 100 mW cm^{-2} (or 1 sun) and 25 °C. AM 1.5 simulate the solar spectrum with an incident angle, such that the light path through the atmosphere is 1.5 times longer than the one striking the surface in a perpendicular angle.

Incident photon-to-current conversion efficiency

The incident photon-to-current conversion efficiency (IPCE) is defined as the ratio between the number of photoinjected electrons that flow through the cell's external circuit (generating electrical current) and the number of incident photons in the same surface area for a specific wavelength of the incident light. In DSCs the IPCE is a product of three factors:

$$\mathrm{IPCE} = \mathrm{LHE}\,\phi_{\mathrm{inj}}\eta_{\mathrm{c}} \tag{1.11}$$

where LHE (light harvesting efficiency) is the ratio between the number of absorb and incident photons, i.e., the absorption efficiency of the incident radiation on the cell (correlated directly with the dye's absorption spectrum); ϕ_{inj} is the injection efficiency of the photoexcited electrons into the conduction band of the semiconductor; η_c is the electron collection efficiency through the external circuit. The IPCE can also be written according to:

$$\mathrm{IPCE}[\%] = \frac{1240[\mathrm{eV\,.\,nm}]\ \mathrm{x}\ J_{sc}[\mu\mathrm{Acm}^{-2}]}{\lambda[\mathrm{nm}]\ \mathrm{x}\ \phi[\mu\ \mathrm{Wcm}^{-2}]}\, x100 \tag{1.12}$$

where J_{sc} is the short-circuit current for the incident radiation, λ is the wavelength and ϕ is the intensity of the incident light. When ϕ_{inj} and η_c are close to 100 % (characteristic of very efficient cells), IPCE is determined only by the LHE (i.e. 1 - Transmittance) of the absorbed dye. Very high efficient cells have very high IPCE values, because dyes such as N3 and N719, can efficiently convert photon to electrons over a broad range in the visible light spectrum (up from 90 %) [49].

Electrochemical impedance spectroscopy fundamentals

For more detailed information regarding the performance of a DSC, dynamic methods should be considered. One of the most useful methods for transient probing is electrochemical impedance spectroscopy (EIS). EIS focus on the investigation of the kinetic phenomena of charge transfer at the different DSC components. The main advantage of this technique is to be able to differentiate each complex process occurring in each of the cell's components [100-104]. Additionally it is a very user-friendly technique.

EIS is commonly based on applied a small voltage sinusoidal perturbation, at a given frequency, and measuring the corresponding current response. That response has associated a phase shift, although having the same period. Impedance can be interpreted as being a measurement of the ability of a system to oppose the flow of electrical current, for a particular applied voltage in a specific period of time. This can be expressed as the following:

$$Z = Z_0 \frac{\cos(\omega t)}{\cos(\omega t - \varphi)} \tag{1.13}$$

where Z is the impedance of a given system, ω is the radial frequency, φ is the phase shift, t is time and Z_0 is the magnitude ratio between the voltage perturbation signal, V_0, and the corresponding current response, I_0. Accordingly, the impedance response of a system can be expressed in terms of real and imaginary components (i), using complex notation:

$$Z = Z_0(\cos\varphi + i\sin\omega) \tag{1.14}$$

Equation 1.14 allows for the system to be represented in the form of a Bode and Nyquist diagrams. The Bode diagram is a representation of the symmetric value of the phase shift vs. the applied frequency. The Nyquist diagram is the representation of the negative imaginary impedance component, $-Z'' = Z_0 \sin\varphi$, vs. the real impedance component, $Z' = Z_0 \cos\varphi$. It is important to mention that

the impedance analysis here described assumes a linear response of the system as a function of the imposed perturbation. A pseudo-linear behavior has been shown to exist when EIS measurements are performed using a very small perturbation voltage (1-20 mV), thus ensuring the applicability of the technique [105].

The charge transport in a DSC can be represented by a electrical analog characterized by resistances, capacitances, etc., associated in series and in parallel. The parameters of these models can then be obtained by fitting then to the EIS data. As a result, the fitted data enables the characterization of the electrochemical phenomena that occurs inside the cell such as reaction kinetics, electrical ohmic resistances and mass transfer.

A DSC behaves very differently when subjected to different conditions. When the cell is placed in the dark under short-circuit conditions, there is no generation of either current or voltage, as the Fermi level of the electrons in the conduction band of the semiconductor is in equilibrium with the redox level of the electrolyte. When placed under illumination at short-circuit conditions, current is generated and measured for applied voltage of 0 V - J_{sc}. When the DSC placed under open-circuit conditions (obliging the cell to operate at V_{oc}), either with or without illumination, the EIS characterization under such conditions can provide very useful information concerning its operation - Figure 1.8.

When placed under illumination at open-circuit, Figure 1.8 (a), no current flows through the external circuit. Consequently, as the counter-electrode is in equilibrium (there is no electron transfer from the catalyst to the redox mediator), all injected electrons into the semiconductor's bandgap, are recombined with the triiodide ions, I_3^-, present in the electrolyte. At the same time, oxidized photosensitizer molecules are reduced (restored) by iodide ions, I^- [106]. Consequently, all energy contained in the absorbed photons is converted into thermal energy, through the two cycles of oxidation/reduction.

The EIS spectra obtained under such conditions enables to study the recombination of the I_3^- ions and the thermal loss of the electrons and how the combination of such phenomena has in the overall efficiency of the cell [100, 106, 107].

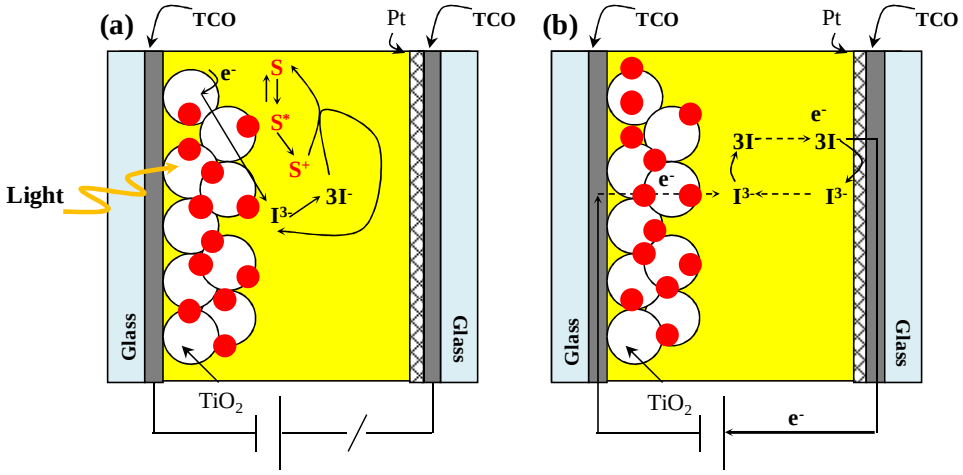

Figure 1.8 DSC operating under different conditions: (a) under illumination and at open-circuit voltage; (b) under dark and also at open-circuit voltage.

When the DSC is placed in the dark at open-circuit, Figure 1.8 (b), the flow of the electrons is reversed and the cell operates at forward bias. In these conditions oxidation of iodide ions, I^-, occur at the catalyst interface at the counter-electrode side. As a result, electrons are transported across the external circuit and into the semiconductor, where they travel across until reaching the electrolyte/semiconductor interface. There recombination of the triiodide ions takes place, yielding new iodide ions that diffuse through the electrolyte until the counter-electrode interface, for a new cycle [100]. A typical EIS generated under the aforementioned conditions is represented in Figure 1.9 .It can be seen three frequency peaks in the Bode phase diagram and 3 semicircles in the Nyquist diagrams. The different peaks and semicircles represented can be attributed to different phenomena, from high to low frequencies (left to right in Figure 1.9 (b)): redox reaction/catalysis that takes place at the counter-electrode

interface, electron transfer (transport and recombination) at the semiconductor/electrolyte interface and the Nernst diffusion of the redox mediator species throughout the electrolyte [100]. For some configurations of materials, the low frequency peak disappears underneath the mid-frequency one [100]. By fitting such spectra through the use of electrical analogues it is possible to extract further information of the phenomena.

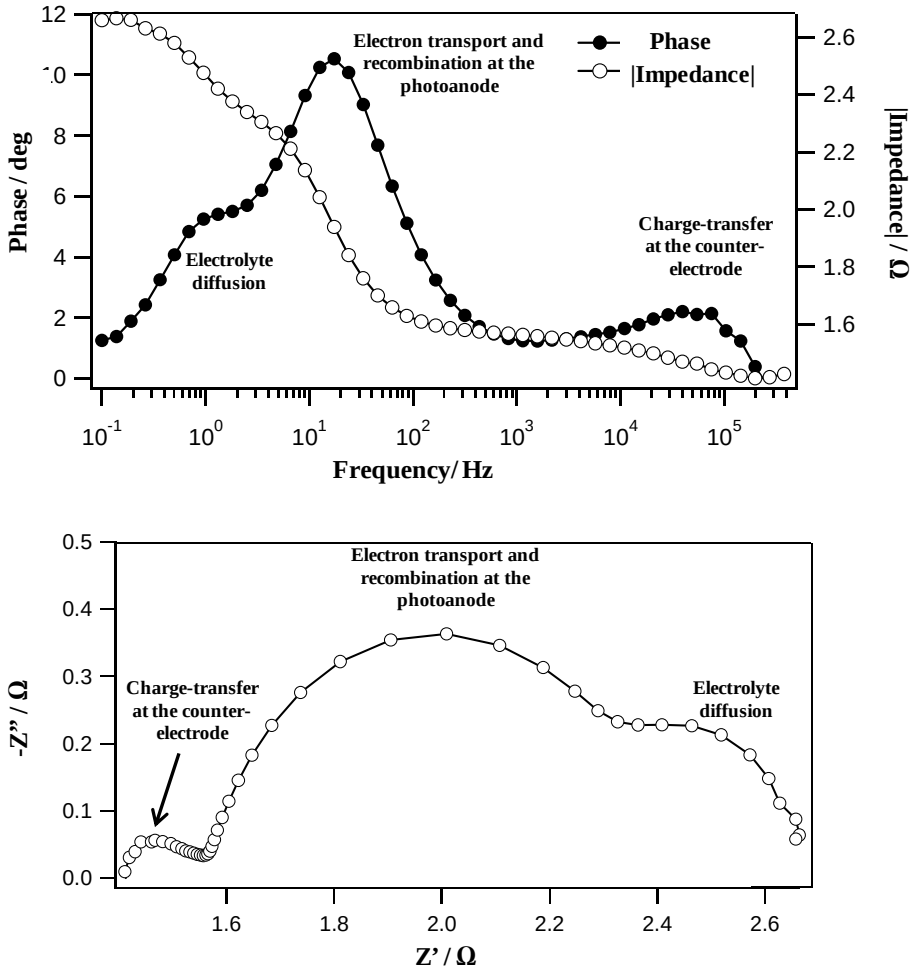

Figure 1.9 Typical Bode (a) and Nyquist (b) diagrams of a DSC, obtained in the dark under open-circuit conditions.

1.3. Objectives and outline of this thesis

In the last few years, DSCs are been gaining interested as potential replacement to traditional photovoltaic technologies. This thesis intent to narrow the gap that presently exists concerning the industrialization of such cells.

In Chapter 1, the energy paradigm is introduced with particular focus on photovoltaic technology, where it is included the DSC. The physics of the DSC is discussed. A brief overview of the typical structure and materials is given and its the working principle is presented. The main characterization techniques are addressed.

Chapters 2, 3 and 4 concern the study of the feasibility to use carbon-based materials as low-cost and efficient replacements of the traditional used catalyst (platinum) in the counter electrode side. Chapter 2 addresses the use of singe-wall carbon nanohorns either in pristine and Pt-decorated forms. In Chapter 3, graphene structures are studied. The role of the degree and type of reduction on graphene-oxide films, targeting efficient and transparent cells is studied. Chapter 4 adresses the use of composite graphene-metal films as a way to further improve efficiency.

In Chapter 5, an innovative sealing method using a laser-assisted glass frit technique explored and tested.

Chapter 6 exhibits the up-scaling and integration of non-optimized graphene-based counter-electrodes with the developed sealing technique of Chapter 5.

Finally, Chapter 7 presents the main conclusions of the present thesis, along with future work suggestions.

References

1. *International Energy Outlook*. 2009, Energy Information Administration.
2. DLR, G.A.C.-. *Concentrating Solar Power for the Mediterranean Region*. 2005, Institute of Technical Thermodynamics: Stuttgart.
3. Hoffmann, W., *PV solar electricity industry: Market growth and perspective.* Solar Energy Materials and Solar Cells, 2006. **90**(18-19): p. 3285-3311.
4. Greijer, H., L. Karlson, S.E. Lindquist, and A. Hagfeldt, *Environmental aspects of electricity generation from a nanocrystalline dye sensitized solar cell system.* Renewable Energy, 2001. **23**(1): p. 27-39.
5. Konrad, T. *http://www.altenergystocks.com/archives/2009/04/why_csp_should_not_try_to_be_coal.html*. 15th January 2010 15th January 2010]; Available from: http://www.altenergystocks.com/archives/2009/04/why_csp_should_not_try_to_be_coal.html.
6. O'Regan, B. and M. Grätzel, *A Low-Cost, High-Efficiency Solar-Cell Based on Dye-Sensitized Colloidal TiO_2 Films.* Nature, 1991. **353**(6346): p. 737-740.
7. *International Energy Outlook 2011*. 2011, Energy Information Administration.
8. BP, *Statistical Review of World Energy*. 2012.
9. *Key World Energy Statistics 2011*. 2011, International Energy Agency.
10. Jager-Waldau, A., *Photovoltaics and renewable energies in Europe.* Renewable & Sustainable Energy Reviews, 2007. **11**: p. 1414-1437.

11. *International Energy Outlook 2007*. 2007, Energy Information Administration.
12. *Renewables 2011 Global Status Report - REN 21*. 2011.
13. *Renewables 2012 Global Status Report - REN 21*. 2012.
14. Dhere, N., *Toward GW/year of CIGS production within the next decade.* Solar Energy Materials and Solar Cells, 2007. **91**(15-16): p. 1376-1382.
15. Pizzini, S., M. Acciarri, and S. Binetti, *From electronic grade to solar grade silicon: chances and challenges in photovoltaics.* physica status solidi (a), 2005. **202**(15): p. 2928-2942.
16. Zervos, H., *Dye Sensitized Solar Cells (DSSC/DSC) 2012-2023: Technologies, Markets, Players*. 2012.
17. Dorn, J.G. *Solar Power*. 2007 [cited 2008 10/12/2008]; Available from: http://www.earthpolicy.org/Indicators/Solar/2007.htm.
18. Webpage. [cited 2013 May, 3th]; Available from: https://docs.google.com/spreadsheet/pub?key=0Ahl2afL-jL0BdEVGU3dsbllfTzlxMEV0aTNqT0d5Nnc&output=html.
19. Grätzel, M., *Photoelectrochemical cells.* Nature, 2001. **414**(6861): p. 338-344.
20. Green, M.A., K. Emery, Y. Hishikawa, W. Warta, and E.D. Dunlop, *Solar cell efficiency tables (version 41).* Progress in Photovoltaics: Research and Applications, 2013. **21**(1): p. 1-11.
21. Yella, A., H.-W. Lee, H.N. Tsao, C. Yi, A.K. Chandiran, M.K. Nazeeruddin, E.W.-G. Diau, C.-Y. Yeh, S.M. Zakeeruddin, and M. Graetzel, *Porphyrin-Sensitized Solar Cells with Cobalt (II/III)-Based Redox Electrolyte Exceed 12 Percent Efficiency.* Science, 2011. **334**(6056): p. 629-634.
22. Grätzel, M., *Solar Energy Conversion by Dye-Sensitized Photovoltaic Cells.* Inorg. Chem., 2005. **44**(20): p. 6841-6851.

23. Snaith, H.J., *Estimating the Maximum Attainable Efficiency in Dye-Sensitized Solar Cells.* Advanced Functional Materials, 2010. **20**(1): p. 13-19.

24. Boschloo, G., L. Haggman, and A. Hagfeldt, *Quantification of the Effect of 4-tert-Butylpyridine Addition to I^-/I_3^- Redox Electrolytes in Dye-Sensitized Nanostructured TiO_2 Solar Cells.* J. Phys. Chem. B, 2006. **110**(26): p. 13144-13150.

25. Hamann, T., R. Jensen, A. Martinson, H. Ryswyk, and J. Hupp, *Advancing beyond current generation dye-sensitized solar cells.* Energy & Environmental Science, 2008. **1**(1): p. 66-78.

26. Green, M.A., K. Emery, Y. Hishikawa, and W. Warta, *Solar cell efficiency tables (Version 33).* Progress in Photovoltaics: Research and Applications, 2009. **17**(1): p. 85-94.

27. Spath, M., J. van Roosmalen, P. Sommeling, and N. van der Burg, *Dye sensitised solar cells from laboratory scale to pre-pilot stage.* Proceedings of 3rd World Conference on Photovoltaic Energy Conversion, Vols a-C, 2003: p. 196-199.

28. Kroon, J., N. Bakker, H. Smit, P. Liska, K. Thampi, P. Wang, S. Zakeeruddin, M. Grätzel, A. Hinsch, S. Hore, U. Würfel, R. Sastrawan, J. Durrant, E. Palomares, H. Pettersson, T. Gruszecki, J. Walter, K. Skupien, and G. Tulloch, *Nanocrystalline dye-sensitized solar cells having maximum performance.* Progress in Photovoltaics: Research and Applications, 2007. **15**(1): p. 1-18.

29. Smestad, G.P., *Education and solar conversion: Demonstrating electron transfer.* Solar Energy Materials and Solar Cells, 1998. **55**(1-2): p. 157-178.

30. Raga, S.R. and F. Fabregat-Santiago, *Temperature effects in dye-sensitized solar cells.* Physical Chemistry Chemical Physics, 2013. **15**(7): p. 2328-2336.

31. Toyoda, T., T. Sano, J. Nakajima, S. Doi, S. Fukumoto, A. Ito, T. Tohyama, M. Yoshida, T. Kanagawa, T. Motohiro, T. Shiga, K. Higuchi, K. Tanaka, Y. Takeda, T. Fukano, N. Katoh, A. Takeichi, K. Takechi, and M. Shiozawa. *Outdoor performance of large scale DSC modules*. in *International Conference on Photochemistry*. 2003. Nara, JAPAN: Elsevier Science Sa.

32. Tulloch, G., *Light and energy--dye solar cells for the 21st century.* Journal of Photochemistry and Photobiology A: Chemistry, 2004. **164**(1-3): p. 209-219.

33. Yoon, S., S. Tak, J. Kim, Y. Jun, K. Kang, and J. Park, *Application of transparent dye-sensitized solar cells to building integrated photovoltaic systems.* Building and Environment, 2011. **46**(10): p. 1899-1904.

34. Suzuki, K., M. Yamaguchi, M. Kumagai, and S. Yanagida, *Application of Carbon Nanotubes to Counter Electrodes of Dye-sensitized Solar Cells.* Chemistry Letters, 2003. **32**(1): p. 28-29.

35. Murakami, T. and M. Grätzel, *Counter electrodes for DSC: Application of functional materials as catalysts.* Inorganica Chimica Acta, 2008. **361**(3): p. 572-580.

36. Imoto, K., K. Takahashi, T. Yamaguchi, T. Komura, J. Nakamura, and K. Murata, *High-performance carbon counter electrode for dye-sensitized solar cells.* Solar Energy Materials and Solar Cells, 2003. **79**(4): p. 459-469.

37. Lee, W.J., E. Ramasamy, D.Y. Lee, and J.S. Song, *Grid type dye-sensitized solar cell module with carbon counter electrode.* Journal of Photochemistry and Photobiology a-Chemistry, 2008. **194**(1): p. 27-30.

38. Kwak, D.-J., B.-H. Moon, D.-K. Lee, C.-S. Park, and Y.-M. Sung, *Comparison of transparent conductive indium tin oxide, titanium-doped indium oxide, and fluorine-doped tin oxide films for dye-sensitized solar cell application.* Journal of Electrical Engineering and Technology, 2011. **6**(5): p. 684-687.

39. Toivola, M., J. Halme, K. Miettunen, K. Aitola, and P.D. Lund, *Nanostructured dye solar cells on flexible substrates-Review.* International Journal of Energy Research, 2009. **33**(13): p. 1145-1160.

40. Miettunen, K., J. Halme, and P. Lund, *Metallic and plastic dye solar cells.* Wiley Interdisciplinary Reviews: Energy and Environment, 2013. **2**(1): p. 104-120.

41. Goncalves, L.M., V.D. Bermudez, H.A. Ribeiro, and A.M. Mendes, *Dye-sensitized solar cells: A safe bet for the future.* Energy & Environmental Science, 2008. **1**(6): p. 655-667.

42. Kalyanasundaram, K. and M. Grätzel, *Applications of functionalized transition metal complexes in photonic and optoelectronic devices.* Coordination Chemistry Reviews, 1998. **177**(1): p. 347-414.

43. Deb, S., *Dye-sensitized TiO_2 thin-film solar cell research at the National Renewable Energy Laboratory (NREL).* Solar Energy Materials and Solar Cells, 2005. **88**(1): p. 1-10.

44. Ito, S., T. Murakami, P. Comte, P. Liska, C. Grätzel, M. Nazeeruddin, and M. Grätzel, *Fabrication of thin film dye sensitized solar cells with solar to electric power conversion efficiency over 10%.* Thin Solid Films, 2008. **516**(14): p. 4613-4619.

45. Lee, K.-M., V. Suryanarayanan, and K.-C. Ho, *Influences of different TiO_2 morphologies and solvents on the photovoltaic performance of dye-sensitized solar cells.* Journal of Power Sources, 2009. **188**(2): p. 635-641.

46. Koo, H., J. Park, B. Yoo, K. Yoo, K. Kim, and N. Park, *Size-dependent scattering efficiency in dye-sensitized solar cell.* Inorganica Chimica Acta, 2008. **361**(3): p. 677-683.

47. Hu, L.H., S.Y. Dai, J. Weng, S.F. Xiao, Y.F. Sui, Y. Huang, S.H. Chen, F.T. Kong, X. Pan, L.Y. Liang, and K.J. Wang, *Microstructure design of nanoporous TiO_2 photoelectrodes for dye-sensitized solar cell modules.* Journal of Physical Chemistry B, 2007. **111**(2): p. 358-362.

48. Hart, J., D. Menzies, Y. Cheng, G. Simon, and L. Spiccia, *TiO_2 sol-gel blocking layers for dye-sensitized solar cells.* Comptes Rendus Chimie, 2006. **9**(5-6): p. 622-626.

49. Nazeeruddin, M., A. Kay, I. Rodicio, R. Humphry-Baker, E. Mueller, P. Liska, N. Vlachopoulos, and M. Grätzel, *Conversion of light to electricity by cis-X2bis(2,2'-bipyridyl-4,4'-dicarboxylate)ruthenium(II) charge-transfer sensitizers (X = Cl-, Br-, I-, CN-, and SCN-) on nanocrystalline titanium dioxide electrodes.* J. Am. Chem. Soc., 1993. **115**(14): p. 6382-6390.

50. Nazeeruddin, M.K., T. Bessho, L. Cevey, S. Ito, C. Klein, F. De Angelis, S. Fantacci, P. Comte, P. Liska, H. Imai, and M. Graetzel, *A high molar extinction coefficient charge transfer sensitizer and its application in dye-sensitized solar cell.* Journal of Photochemistry and Photobiology a-Chemistry, 2007. **185**(2-3): p. 331-337.

51. Kalowekamo, J. and E. Baker, *Estimating the manufacturing cost of purely organic solar cells.* Solar Energy, 2009. **83**(8): p. 1224-1231.

52. Wolfbauer, G., A.M. Bond, J.C. Eklund, and D.R. MacFarlane, *A channel flow cell system specifically designed to test the efficiency of redox shuttles in dye sensitized solar cells.* Solar Energy Materials and Solar Cells, 2001. **70**(1): p. 85-101.

53. Hauch, A. and A. Georg, *Diffusion in the electrolyte and charge-transfer reaction at the platinum electrode in dye-sensitized solar cells.* Electrochimica Acta, 2001. **46**(22): p. 3457-3466.

54. Kong, F., S. Dai, and K. Wang, *Review of recent progress in dye-sensitized solar cells.* Advances in OptoElectronics, 2007. **2007**: p. 75384.

55. Daeneke, T., T.-H. Kwon, A.B. Holmes, N.W. Duffy, U. Bach, and L. Spiccia, *High-efficiency dye-sensitized solar cells with ferrocene-based electrolytes.* Nat Chem, 2011. **3**(3): p. 211-215.

56. Murakami, T.N., S. Ito, Q. Wang, M.K. Nazeeruddin, T. Bessho, I. Cesar, P. Liska, R. Humphry-Baker, P. Comte, P. Pechy, and M. Gratzel, *Highly efficient dye-sensitized solar cells based on carbon black counter electrodes.* Journal of The Electrochemical Society, 2006. **153**(12): p. A2255-A2261.

57. Lan, Z., J. Wu, J. Lin, and M. Huang, *Morphology controllable fabrication of Pt counter electrodes for highly efficient dye-sensitized solar cells.* Journal of Materials Chemistry, 2012. **22**(9): p. 3948-3954.

58. Kaniyoor, A. and S. Ramaprabhu, *Enhanced efficiency in dye sensitized solar cells with nanostructured Pt decorated multiwalled carbon nanotube based counter electrode.* 2012.

59. Denaro, T., V. Baglio, M. Girolamo, V. Antonucci, A.S. Arico, F. Matteucci, and R. Ornelas, *Investigation of low cost carbonaceous materials for application as counter electrode in dye-sensitized solar cells.* Journal of Applied Electrochemistry, 2009. **39**(11): p. 2173-2179.

60. Kitamura, T., M. Maitani, M. Matsuda, Y. Wada, and S. Yanagida, *Improved Solid-State Dye Solar Cells with Polypyrrole using a Carbon-Based Counter Electrode.* Chemistry Letters, 2001. **30**(10): p. 1054-1055.

61. Cha, S.I., B.K. Koo, S.H. Seo, and D.Y. Lee, *Pt-free transparent counter electrodes for dye-sensitized solar cells prepared from carbon nanotube micro-balls.* Journal of Materials Chemistry, 2009. **20**(4): p. 659-662.

62. Chou, C.-S., R.-Y. Yang, M.-H. Weng, and C.-I. Huang, *The applicability of SWCNT on the counter electrode for the dye-sensitized solar cell.* Advanced Powder Technology, 2009. **20**(4): p. 310-317.

63. Ramasamy, E., W.J. Lee, D.Y. Lee, and J.S. Song, *Spray coated multi-wall carbon nanotube counter electrode for tri-iodide (I_3-) reduction in dye-sensitized solar cells.* Electrochemistry Communications, 2008. **10**(7): p. 1087-1089.

64. Geim, A.K. and K.S. Novoselov, *The rise of graphene.* Nature Materials, 2007. **6**(3): p. 183-191.

65. Wu, Z., Z. Chen, X. Du, J.M. Logan, J. Sippel, M. Nikolou, K. Kamaras, J.R. Reynolds, D.B. Tanner, A.F. Hebard, and A.G. Rinzler, *Transparent, Conductive Carbon Nanotube Films.* Science, 2004. **305**(5688): p. 1273-1276.

66. Wallace, G.G. and D. Li, *Process for the preparation of graphene*. 2009, UNIV WOLLONGONG.

67. Choi, J., Y. Lee, H. Shin, S. Yoon, J.Y. Choi, Y.H. Lee, H.J. Shin, and S.M. Yoon, *Flexible transparent electrode useful in a display device e.g. liquid crystal display and an electronic paper like display, comprises a transparent substrate, and a transparent conductive film comprising a graphene sheet*. 2009, SAMSUNG ELECTRONICS CO

LTD (SMSU) UNIV SUNGKYUNKWAN FOUND CORP COLLABORATI (UYSU-Non-standard).

68. Shin, H.-j., J.-y. Choi, and S.-m. Yoon, *Reduced graphene oxide doped with dopant, thin layer and transparent electrode.* 2009, Samsung Electronics Co., Ltd.

69. Wang, S.J., Y. Geng, Q. Zheng, and J.-K. Kim, *Fabrication of highly conducting and transparent graphene films.* Carbon, 2010. **48**(6): p. 1815-1823.

70. Li, D., M.B. Muller, S. Gilje, R.B. Kaner, and G.G. Wallace, *Processable aqueous dispersions of graphene nanosheets.* Nature Nanotechnology, 2008. **3**(2): p. 101-105.

71. Titelman, G.I., V. Gelman, S. Bron, R.L. Khalfin, Y. Cohen, and H. Bianco-Peled, *Characteristics and microstructure of aqueous colloidal dispersions of graphite oxide.* Carbon, 2005. **43**(3): p. 641-649.

72. Si, Y. and E.T. Samulski, *Synthesis of Water Soluble Graphene.* Nano Letters, 2008. **8**(6): p. 1679-1682.

73. Roy-Mayhew, J.D., D.J. Bozym, C. Punckt, and I.A. Aksay, *Functionalized Graphene as a Catalytic Counter Electrode in Dye-Sensitized Solar Cells.* Acs Nano, 2010. **4**(10): p. 6203-6211.

74. Trancik, J.E., S.C. Barton, and J. Hone, *Transparent and catalytic carbon nanotube films.* Nano Letters, 2008. **8**(4): p. 982-987.

75. Hong, W.J., Y.X. Xu, G.W. Lu, C. Li, and G.Q. Shi, *Transparent graphene/PEDOT-PSS composite films as counter electrodes of dye-sensitized solar cells.* Electrochemistry Communications, 2008. **10**(10): p. 1555-1558.

76. Zhang, D.W., X.D. Li, S. Chen, H.B. Li, Z. Sun, X.J. Yin, and S.M. Huang. *Graphene Nanosheet Counter-Electrodes for Dye-Sensitized*

Solar Cells. in *Nanoelectronics Conference (INEC), 2010 3rd International*. 2010. New York.

77. Wang, X., L.J. Zhi, and K. Mullen, *Transparent, conductive graphene electrodes for dye-sensitized solar cells.* Nano Letters, 2008. **8**(1): p. 323-327.

78. Xu, Y., H. Bai, G. Lu, C. Li, and G. Shi, *Flexible Graphene Films via the Filtration of Water-Soluble Noncovalent Functionalized Graphene Sheets.* Journal of the American Chemical Society, 2008. **130**(18): p. 5856-5857.

79. Wan, L., S. Wang, X. Wang, B. Dong, Z. Xu, X. Zhang, B. Yang, S. Peng, J. Wang, and C. Xu, *Room-temperature fabrication of graphene films on variable substrates and its use as counter electrodes for dye-sensitized solar cells.* Solid State Sciences, 2011. **13**(2): p. 468-475.

80. Choi, H., H. Kim, S. Hwang, W. Choi, and M. Jeon, *Dye-sensitized solar cells using graphene-based carbon nano composite as counter electrode.* Solar Energy Materials and Solar Cells, 2011. **95**(1): p. 323-325.

81. Huh, S.H., S.-H. Choi, and H.-M. Ju, *Thickness-dependent solar power conversion efficiencies of catalytic graphene oxide films in dye-sensitized solar cells.* Current Applied Physics, 2011. **11**(3, Supplement): p. S352-S355.

82. Kavan, L., J.H. Yum, and M. Grätzel, *Optically Transparent Cathode for Dye-Sensitized Solar Cells Based on Graphene Nanoplatelets.* Acs Nano, 2010. **5**(1): p. 165-172.

83. Choi, H., S. Hwang, H. Bae, S. Kim, H. Kim, and M. Jeon, *Electrophoretic graphene for transparent counter electrodes in dye-sensitised solar cells.* Electronics Letters, 2011. **47**: p. 281-283.

84. Pettersson, H., T. Gruszecki, L.-H. Johansson, and P. Johander, *Manufacturing method for monolithic dye-sensitised solar cells permitting long-term stable low-power modules.* Solar Energy Materials and Solar Cells, 2003. **77**(4): p. 405-413.

85. Spath, M., P.M. Sommeling, J.A.M. van Roosmalen, H.J.P. Smit, N.P.G. van der Burg, D.R. Mahieu, N.J. Bakker, and J.M. Kroon, *Reproducible manufacturing of dye-sensitized solar cells on a semi-automated baseline.* Progress in Photovoltaics, 2003. **11**(3): p. 207-220.

86. Sastrawan, R., J. Beier, U. Belledin, S. Hemming, A. Hinsch, R. Kern, C. Vetter, F.M. Petrat, A. Prodi-Schwab, P. Lechner, and W. Hoffmann, *A glass frit-sealed dye solar cell module with integrated series connections.* Solar Energy Materials and Solar Cells, 2006. **90**(11): p. 1680-1691.

87. Hinsch, A., J. Kroon, R. Kern, I. Uhlendorf, J. Holzbock, A. Meyer, and J. Ferber, *Long-term stability of dye-sensitised solar cells.* Progress in Photovoltaics: Research and Applications, 2001. **9**(6): p. 425-438.

88. Syrrokostas, G., A. Siokou, G. Leftheriotis, and P. Yianoulis, *Degradation mechanisms of Pt counter electrodes for dye sensitized solar cells.* Solar Energy Materials and Solar Cells, 2012. **103**: p. 119-127.

89. Bari, D., N. Wrachien, R. Tagliaferro, S. Penna, T.M. Brown, A. Reale, A. Di Carlo, G. Meneghesso, and A. Cester, *Thermal stress effects on Dye-Sensitized Solar Cells (DSSCs).* Microelectronics Reliability, 2011. **51**(9-11): p. 1762-1766.

90. Kitamura, T., K. Okada, H. Matsui, and N. Tanabe, *Durability of Dye-Sensitized Solar Cells and Modules.* Journal of Solar Energy Engineering-Transactions of the Asme, 2010. **132**(2).

91. Lamberson, L.A., R.M. Morena, L. Lamberson, and R. Morena, *Hermetically sealed glass package preform manufacture, e.g. for sensor, by depositing frit comprising base glass from, e.g. rare earth metal oxide, and filler on glass substrate, and pre-sintering at lower temperature in inert atmosphere*, Corning Inc (Corg).

92. Sastrawan, R., J. Beier, U. Belledin, S. Hemming, A. Hinsch, R. Kern, C. Vetter, F.M. Petrat, A. Prodi-Schwab, and P.L.W. Hoffmann, *New interdigital design for large area dye solar modules using a lead-free glass frit sealing.* Progress in Photovoltaics: Research and Applications, 2006. **14**(8): p. 697-709.

93. Hinsch, A., S. Behrens, M. Berginc, H. Bonnemann, H. Brandt, A. Drewitz, F. Einsele, D. Fassler, D. Gerhard, H. Gores, R. Haag, T. Herzig, S. Himmler, G. Khelashvili, D. Koch, G. Nazmutdinova, U. Opara-Krasovec, P. Putyra, U. Rau, R. Sastrawan, T. Schauer, C. Schreiner, S. Sensfuss, C. Siegers, K. Skupien, P. Wachter, J. Walter, P. Wasserscheid, U. Wurfel, and M. Zistler, *Material development for dye solar modules: Results from an integrated approach.* Progress in Photovoltaics, 2008. **16**(6): p. 489-501.

94. Lee, W.J., E. Ramasamy, D.Y. Lee, and J.S. Song, *Glass frit overcoated silver grid lines for nano-crystalline dye sensitized solar cells.* Journal of Photochemistry and Photobiology a-Chemistry, 2006. **183**(1-2): p. 133-137.

95. Lorenz, N., S. Millar, M. Desmulliez, and D.P. Hand, *Hermetic glass frit packaging in air and vacuum with localized laser joining.* Journal of Micromechanics and Microengineering, 2011. **21**(4): p. 045039.

96. Ribeiro, F., J. Maçaira, R. Cruz, J. Gabriel, L. Andrade, and A. Mendes, *Laser assisted glass frit sealing of dye-sensitized solar cells.* Solar Energy Materials and Solar Cells, 2012. **96**(0): p. 43-49.

97. Kato, N., Y. Takeda, K. Higuchi, A. Takeichi, E. Sudo, H. Tanaka, T. Motohiro, T. Sano, and T. Toyoda, *Degradation analysis of dye-sensitized solar cell module after long-term stability test under outdoor working condition.* Solar Energy Materials and Solar Cells, 2009. **93**(6-7): p. 893-897.

98. Tachibana, Y., J.E. Moser, M. Gratzel, D.R. Klug, and J.R. Durrant, *Subpicosecond Interfacial Charge Separation in Dye-Sensitized Nanocrystalline Titanium Dioxide Films.* J. Phys. Chem., 1996. **100**(51): p. 20056-20062.

99. Cherepy, N., G. Smestad, M. Grätzel, and J. Zhang, *Ultrafast Electron Injection: Implications for a Photoelectrochemical Cell Utilizing an Anthocyanin Dye-Sensitized TiO_2 Nanocrystalline Electrode.* J. Phys. Chem. B, 1997. **101**(45): p. 9342-9351.

100. Kern, R., R. Sastrawan, J. Ferber, R. Stangl, and J. Luther, *Modeling and interpretation of electrical impedance spectra of dye solar cells operated under open-circuit conditions.* Electrochimica Acta, 2002. **47**(26): p. 4213-4225.

101. Wang, Q., J.E. Moser, and M. Gratzel, *Electrochemical impedance spectroscopic analysis of dye-sensitized solar cells.* Journal of Physical Chemistry B, 2005. **109**(31): p. 14945-14953.

102. Han, L.Y., N. Koide, Y. Chiba, and T. Mitate, *Modeling of an equivalent circuit for dye-sensitized solar cells.* Applied Physics Letters, 2004. **84**(13): p. 2433-2435.

103. Stangl, R., J. Ferber, and J. Luther, *On the modeling of the dye-sensitized solar cell.* Solar Energy Materials and Solar Cells, 1998. **54**(1-4): p. 255-264.

104. Wang, Q., S. Ito, M. Gratzel, F. Fabregat-Santiago, I. Mora-Sero, J. Bisquert, T. Bessho, and H. Imai, *Characteristics of high efficiency dye-*

sensitized solar cells. Journal of Physical Chemistry B, 2006. **110**: p. 25210-25221.

105. Macdonald, J.R., *Impedance Spectroscopy*. 1987: Wiley.

106. Fabregat-Santiago, F., J. Bisquert, G. Garcia-Belmonte, G. Boschloo, and A. Hagfeldt, *Influence of electrolyte in transport and recombination in dye-sensitized solar cells studied by impedance spectroscopy.* Solar Energy Materials and Solar Cells, 2005. **87**(1-4): p. 117-131.

107. Fabregat-Santiago, F., J. Bisquert, E. Palomares, L. Otero, D.B. Kuang, S.M. Zakeeruddin, and M. Gratzel, *Correlation between photovoltaic performance and impedance spectroscopy of dye-sensitized solar cells based on ionic liquids.* Journal of Physical Chemistry C, 2007. **111**(17): p. 6550-6560.

Chapter 2

Use of single wall carbon nanohorns as counter-electrodes in dye-sensitized solar cells

Rui Cruz, Lúcia Brandão, Adélio Mendes

(International Journal of Energy Research, 2012, DOI: 10.1002/er.2959)

Abstract

The catalytic activity of single wall carbon nanohorns (SWNH) as counter electrodes (CE) of dye sensitized solar cells (DSC) was studied for the iodide/triiodide redox reaction. The catalytic activities of SWNH and high surface SWNH (HS-SWNH) obtained by partial oxidation of SWNH, were assessed based on charge transfer resistances (R_{ct}) and current-voltage curves. A half-cell configuration was used and CE performances were compared to CEs made of carbon black (CB) and Pt. A CE assembled with HS-SWNH and mixed with 10 wt.% of hydroxyethyl cellulose (HEC) - HS-SWNH/HEC, was found to have the highest electrocatalytic activity (lowest R_{ct}) among all the carbon-based CEs tested when annealed at 180 ºC (R_{ct} = 141 Ω cm^2); however, a very thick film (several tens of μm) would be required in order to perform comparably to a Pt CE. The annealing of such CE at higher temperatures (above 400 ºC) did not improve its catalytic activity, contrary to the other studied carbonaceous CEs.

The redox catalytic activity of SWNH and HS-SWNH decorated with Pt were also studied on a half-cell configuration and compared to that of Pt/CB and pristine Pt. The Pt/SWNH/HEC CE showed the highest electrocatalytic

activity per mass of Pt, needing just 50 % of Pt load to yield the same electrocatalytic activity of a DSC equipped with a Pt CE, but having half of its transparency. Additionally, applications in temperature-sensitive substrates are envisioned for the Pt/SWNH/HEC CE due to the use of lower annealing temperatures

Keywords: Dye-sensitized solar cell; Cathode; Single wall carbon nanohorns; Platinum.

2.1. Introduction

Dye-sensitized solar cells (DSCs) are seen as a promising alternative for conventional photovoltaic devices due to their potentially low production costs, versatility and high efficiency for energy conversion [1-3]. A DSC is generally comprised of three main components [4]: i) a porous nanocrystalline TiO_2 film coated with a monolayer of a dye and deposited onto a transparent conductive oxide (TCO) coated glass substrate that acts as photoelectrode, ii) an iodide/triiodide redox couple-based electrolyte and iii) a TCO coated glass substrate covered by a catalytic material acting as the counter electrode (CE).

The CE is a very important component in DSC. It collects electrons from the external circuit and reduces (catalyzes) the redox species present in the electrolyte that are used for regenerating the sensitizer dye after electron injection, according to $I_3^- + 2e^- \rightarrow 3I^-$. Typically a platinum layer of ca. 10 nm is used as the catalytic material as it presents the lower overpotential to this reaction while other metals (such as aluminium, iron or nickel) can be corroded by the electrolyte solution. However, platinum is very expensive [5] and future solar conversion systems producing electric power at very high scale would prefer the use of cheap and readily available materials that are simultaneously cheaper than Pt and capable of yielding a relatively high conversion efficiency for DSCs. For that reason, other materials have been suggested for using as CEs [6]: conductive polymers, polymer/platinum composites and carbonaceous materials. Carbon materials have been widely reported due to their electronic conductivity, corrosion resistance towards I_2, high reactivity for triiodide reduction and low cost [6-8]. For instance, Kay and Grätzel [9] fabricated a DSC with a relative high efficiency using a mixture of graphite and carbon black. Since then, CEs of carbon black (CB) [6-8, 10], activated carbon [11], single or multi wall carbon nanotubes [12-15] and graphene [16-19] have been tested. For carbon materials, the active sites responsible for catalysis are located at the edges of the carbon crystals [8]. The performance of these carbon

materials is also strongly affected by the available surface area for reaction [6, 11, 20]. This means that typically high surface area carbons and/or high carbon layer thicknesses (carbon load) have to be used, undermining the DSC's transparency properties offered by the Pt CE.

Platinum nanoparticles supported on different carbon structures have also been used as CE. This strategy allows increasing greatly the available active surface area for catalysis, due to the use of very small platinum nanoparticles. For instance, Li *et. al.* [21] manufactured CEs using CB loaded with a low content of Pt, 1.5 wt%, yielding the same conversion efficiency of a typical Pt CE. Huang *et. al.* [22] used a hybrid material of platinum nanoparticles and multi wall carbon nanotubes to create a CE yielding a relative efficiency of 15 % more than that of pristine Pt CE.

Carbon nanohorns are a new class of carbon with a similar graphitic structure as carbon nanotubes (highly convoluted graphene sheets) [23, 24]. Carbon nanohorns are ca. 2-3 nm in diameter and ca. 50 nm in length and self-assemble in aggregates of about 100 nm. This feature increases their surface area (ca. 300 m^2 g^{-1}) while maintaining the high electrical conductivity due to the close contact amongst carbon nanohorns. On the other hand, their chemical defects and crystal edges provide good electrocatalytic properties for the iodide/triiodide [11, 16, 25] redox reaction. Carbon nanohorns can be easily oxidized by chemical or physical oxidation in order to increase its specific surface area (up to 1000 m^2 g^{-1}) by opening the horn tip, what makes the inner tubular area further accessible to reactants [26]. Moreover, single wall carbon nanohorns (SWNH) can be used as a Pt electrocatalyst support, an approach that has already been successfully applied in fuel cells [26, 27]. Owing to that, a good electrochemical activity should be achievable, while minimizing the necessary amount of Pt for the reduction of the triiodide ions.

There is only one report referring the use of SWNH as CE in DSCs [15]. The DSC's efficiency obtained when compared to a carbon nanotube CE was

lower; however the surface area of SWNH used was low. The study of SWNH in DSC application needs then to be further addressed. This work focus on the use of SWNH in CE with two different surface areas decorated and not decorated with Pt nanoparticles and the influence of a cellulose-based binder. Comparison with carbon black and pristine Pt is also performed.

2.2. Material and Methods

2.2.1. Synthesis and characterization of SWNH

Two different nanocarbon structures are considered in this work: commercial carbon black (Vulcan XC/72R, Cabot) and single wall carbon nanohorns (SWNH). SWNH were synthesized using a AC arc discharge in air, as previously described [24, 27]. The composition of the SWNH sample is ca. 3 wt.% amorphous carbon, 84.5 wt.% SWNH and 12.5 wt.% graphitic carbon [26]. Oxidation treatment for SWNH surface area modification was performed in a furnace during 10 min using a vertical oxygen flow of 30 mL_N min^{-1} at 500 ºC, as described in [26]. The high surface SWNH (HS-SWNH) composition is ca. 84.5 wt.% SWNH and 15.5 wt.% graphitic carbon [26]. Carbon-based CEs decorated with Pt nanoparticles were also tested. For that, ethylene glycol (EG) was used as reducing agent in order to anchor Pt nanoparticles on the different carbon supports [24, 27]. Briefly, SWNH or CB were previously suspended in an ethylene glycol (EG) solution (5 vol.% of water in EG), and the required amount of a 0.8 wt% metal catalyst solution (H_2PtCl_6 .6H2O from Sigma-Aldrich) in the EG solution was added drop wise. NaOH was added to adjust pH above 13 and the mixture was refluxed for 3 h. The sample was filtered and dried for 8 h at 80 ºC. Well-dispersed ≈ 3 nm Pt particles were observed in all carbon structures considered [26, 27]. Surface area and Pt content of the nanocarbon materials tested are given in Table 2.1, respectively [26].

Table 2.1 Surface area and Pt content of the different carbon materials studied.

Catalytic material	BET surface area, $m^2 g^{-1}$	Pt wt.%
CB	231	15.6
SWNH	176	10.0
HS-SWNH	730	20.0

2.2.2. Half-cell (Symmetric dummy cell) preparation

For all CEs, conductive fluorine-doped tin oxide (FTO)-coated glass substrates (2 mm-thick, 2.5 cm x 2.5 cm, sheet resistance 15 Ω $square^{-1}$, Dyesol) were used. The CE based on Pt (Pt CE) was prepared by drop casting a solution of H_2PtCl_6 (ca. 40% Pt (ACROS) in ethanol) onto the surface of the FTO-coated glass substrate, followed by heat treatment at 400 ºC for 15 minutes. The CE based on the carbon nanostructures with and without Pt nanoparticles were prepared by air-brushing ethanolic suspensions of the carbonaceous materials, mixed or not with 10 wt.% of hydroxyethyl cellulose (HEC), onto the conductive glass placed onto a hot-plate at 120 ºC. They were then annealed at 180 ºC for 1 hour and 120 ºC overnight or annealed at 400 ºC / 450 ºC for 15 minutes. The carbon load applied was always ca. 0.4 mg cm^{-2}. Electrodes were assembled at least in duplicate to assess reproducibility.

2.2.3. Electrochemical impedance spectroscopy of half-cells

A half-cell configuration (Figure 2.1), consisting of two identical FTO-coated glass substrates coated with the catalytic material, was used for the electrochemical impedance spectroscopy (EIS) study. The half-cell was sealed with a 25-µm thick Surlyn frame (Solaronix) at 100 ºC for 15 s. After sealing, the cells were filled with an iodide based electrolyte solution (EL-HSE, Dyesol) through a pre-drilled 1 mm diameter hole done on one of the sides. This hole was sealed afterwards using a melted Surlyn disc and a thin glass lamella. Half-

cells were assembled in duplicate for each catalytic material and reproducibility was achieved.

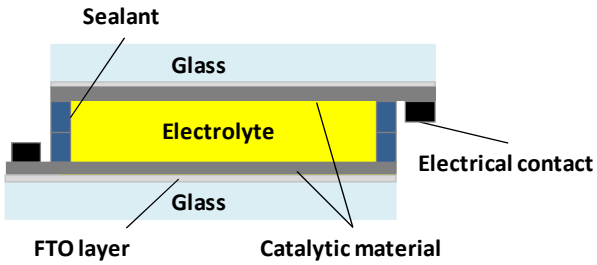

Figure 2.1 Half-cell configuration used in EIS and *I-V* measurements.

EIS experiments were carried out with a ZENNIUM workstation (Ref. 2425-C, Zahner Elektrik, Germany). The frequency range used was 100 mHz - 100 kHz and the magnitude of the modulation signal was 10 mV. All the measurements were performed at room temperature in the dark at 0V. The EIS spectra were fitted to an equivalent electrical analogue [28] – Figure 2.2 (based on a Randles-type circuit), comprised of a charge-transfer resistance, R_{ct}, a double-layer capacitance C, a series resistance, R_s and the Nernst diffusion impedance in the electrolyte, Z_N. Due to deviations from the ideal capacitance, this effect is best described by a constant phase element, CPE, characterized by two parameters - *CPE:B* and *CPE:β* [28]. ZView software (Scribner Associates Inc.) was used to perform the fitting. Current density–voltage (*I-V*) measurements were also carried out in the dark with a scan rate of 100 mV s^{-1} ranging from - 1 V to 1 V.

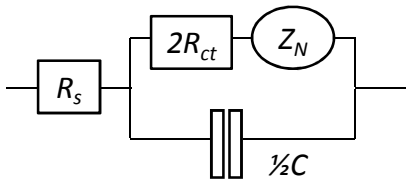

Figure 2.2 Electrical analogue used for fitting the electrochemical impedance spectra data of half-cells.

2.2.4. Dye-sensitized solar cell fabrication

DSCs with an active area of 0.6 cm^2 were fabricated according to the following procedure: FTO-coated glass substrates (2 mm-thick, 2.5 cm x 1.8 cm) were washed in an ultrasonic bath with detergent and then ethanol. A TiO_2 electrode (photoanode) with a thickness of ca. 4-6 μm, was obtained by spreading a TiO_2 paste (20-nm sized TiO_2 particles, DSL18R-T - Dyesol) onto the conducting glass using the doctor blade technique. The deposited paste was sintered in air at 500 °C for 30 minutes. After cooling to 70 °C the TiO_2 electrode was sensitized by immersing it in a N719 dye solution (0.3 mM in ethanol, Dyesol) for a period greater than 12 h and at room temperature. Afterwards the dye-sensitized electrode was rinsed with ethanol and dried in moisture-free environment.

Two CE specimens of Pt (reference) and two CE specimens of SWNH decorated with Pt nanoparticles and mixed with 10 wt.% of HEC were prepared as described above (in section 2.2). The Pt CE was annealed at 400 °C for 15 minutes, while the Pt/SWNH/HEC was annealed at 180 °C for 1 hour and 120 °C overnight.

The photoanode and the counter electrode were sealed with a 25-μm thick Surlyn frame at 100 °C for 15 s. After sealing, the cells were filled with an electrolyte solution (iodide based, EL-HSE Dyesol, Dyesol) through a pre-drilled 1 mm diameter hole done in the counter electrode side. The hole was sealed using a melted Surlyn disc and a thin glass lamella.

2.2.5. I-V and transmittance measurements

A 150 W xenon light source (Oriel class A solar simulator, Newport USA) irradiating 100 mW cm^{-2} (1 sun light-intensity) at the surface of the DSC and equipped with an air mass filter of 1.5 (Newport, USA) was used. The simulator was calibrated using a single crystal Si photodiode (Newport, USA). The *I-V*

characteristics were obtained by applying an external potential bias and measuring the generated photocurrent. Transmittance measurements of DSCs were carried out using an UV/VIS/NIR spectrophotometer (Lambda 750, Perkin Elmer).

2.3. Results and discussion

2.3.1. Half-cell configuration

SWNH, HS-SWNH and CB were tested for the iodide/triodide redox reaction in a half-cell configuration (Figure 2.1). The influence of the annealing temperature and hydroxyethyl cellulose (HEC) presence were also assessed for the different carbon-based CEs. The use of HEC should help to promote the adhesion of the carbonaceous materials to the substrate during the air brushing deposition [21]. The catalytic activity of the CEs was evaluated based on the charge-transfer resistance (R_{ct}) measured at the CE/electrolyte interface on typical CE-CE cells (half-cells). This parameter was obtained by fitting the EIS data (Nyquist plots) obtained in the dark at 0 V – Figures 2.3 (b), 2.4 (b) and 2.5 (b) – to a Randles-type circuit. Additionally, *I-V* measurements - Figures 2.3 (a), 2.4 (a) and 2.5 (a) - were carried out in order to observe the behavior of the CEs at different applied voltages.

2.3.1.1. Pt free carbon counter-electrodes

Table 2.2 shows the parameters obtained from fitting the EIS data for the different Pt free CEs studied, annealed at different temperatures. Results indicate that the R_{ct} of all the catalytic materials studied is affected by the annealing temperature and by the presence of HEC. Figure 2.3 shows the corresponding *I-V* curves.

Table 2.2 Parameters determined by fitting the EIS experimental data to the equivalent circuit – Randles-type circuit, for half-cells assembled with Pt free carbon supported counter electrodes annealed at different temperatures. Standard deviation is shown between brackets.

		0 V		
Annealing T	**CE**	R_{ct} / Ω cm^2	*CPE:B* / μF cm^{-2}	*CPE:β*
180 °C	FTO	4.30 x 10^6	6.9	0.96
	CB	2554 (723)	55.7 (14.2)	0.95
	CB/HEC	1770 (267)	140 (38)	0.95
	SWNH	5912 (1970)	48.8 (15.7)	0.95
	SWNH/HEC	2882 (146)	151 (58)	0.91
	HS-SWNH	1742 (221)	100 (42)	0.93
	HS-SWNH/HEC	141 (47)	180 (57)	0.90
450 °C	CB	18.6 (6.0)	257 (106)	0.80
	CB/HEC	59.5 (22.5)	494 (85)	0.85
400 °C	SWNH	351 (32)	208 (80)	0.88
	SWNH/HEC	266 (12)	410 (127)	0.88
	HS-SWNH	850 (112)	207 (74)	0.88
	HS-SWNH/HEC	1912 (104)	185 (41)	0.90

The deposited films that were annealed at 180 °C still retained HEC within their structure, since the onset decomposition temperature of HEC is 240 °C (DTA/TG data not shown here). Additionally carbon degradation should not occur since the onset burning temperature of the carbon materials is even higher than that of HEC. At 180 °C, the HS-SWNH/HEC CE presents the lowest R_{ct} at 0 V (Table 2.2) and the highest current density for the applied voltage range (Figure 2.3). The improved electrocatalytic activity should be related to the oxidative treatment of the SWNH sample that yielded an increase in the active surface area, originating a higher capacitance and a lower R_{ct}. Additionally, the treatment burned out the 5 or 6 carbon rings [26], leaving holes in the basal

plane and thus creating more edges and consequently more active sites responsible for catalysis [8]. The result obtained for the HS-SWNH/HEC CE could envision a possible application in temperature-sensitive substrates (such as flexible polymeric substrates) due to the lower annealing temperatures. However, for such CEs to have efficiencies comparable to a Pt CE, thick films of HS-SWNH/HEC should be used (several tens of μm). Lower thicknesses (ca. 2 – 30 μm) can be achieved by using for instance carbon nanotubes [12, 13, 25]); however, SWNH are cheaper than carbon nanotubes and potentially as cheap as carbon black because they do not require a metal catalyst during synthesis and do not need purification [29, 30]. Moreover, the performance of a carbon nanotube-based CE annealed at lower temperatures has not been evaluated; for instance, Table 2.2 shows that for a CB-based CE the decrease in annealing temperature can increase R_{ct} up to 2 orders of magnitude.

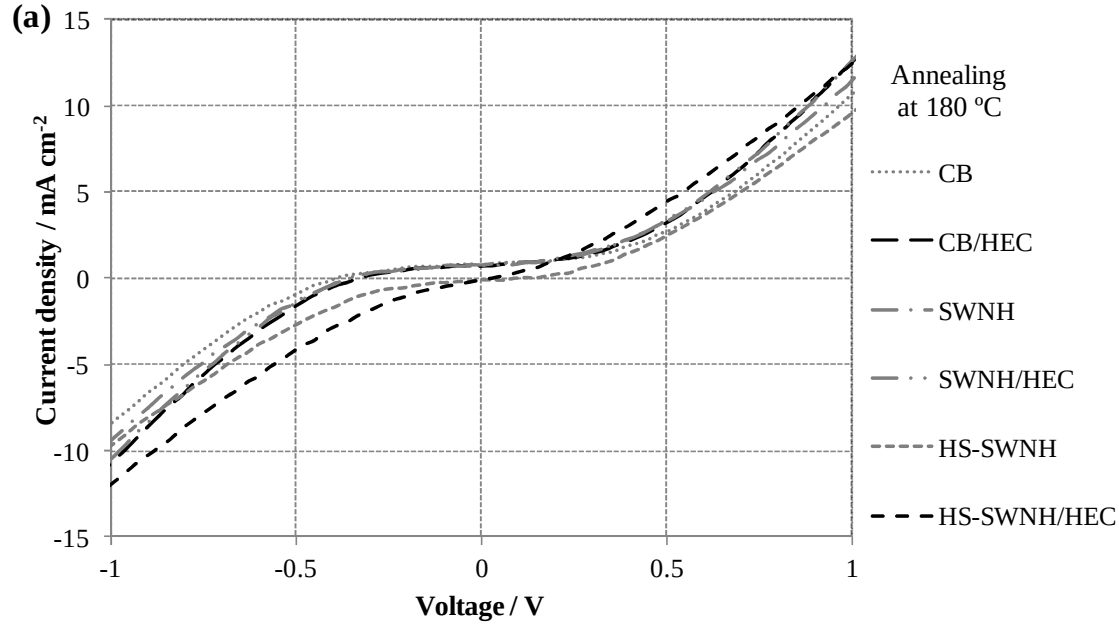

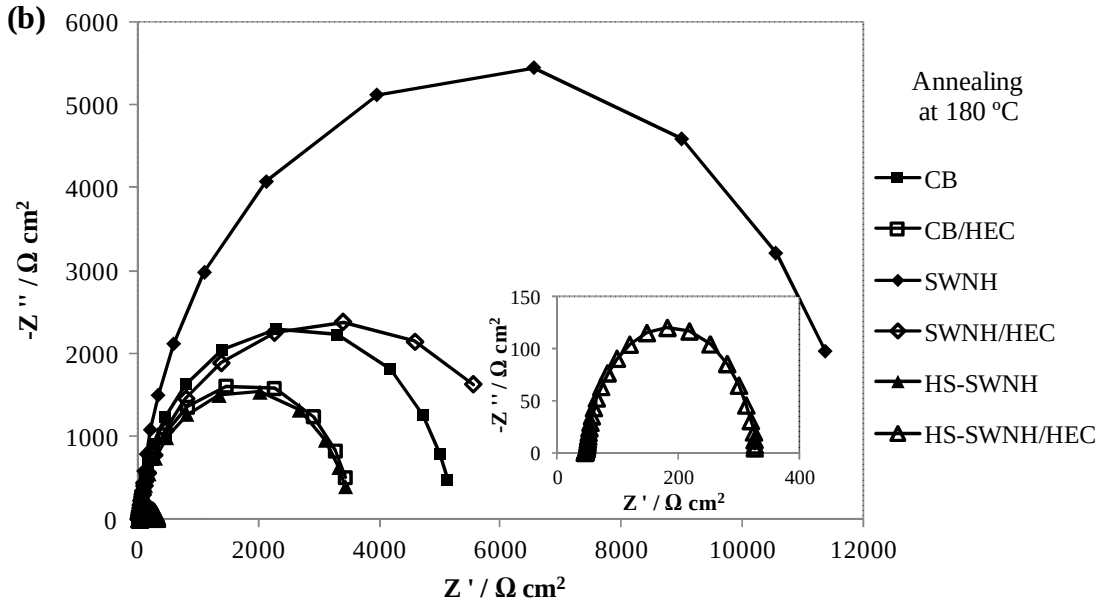

Figure 2.3 Half-cells assembled with Pt free carbon supported counter electrodes annealed at 180 ºC: **(a)** Current density – voltage measurements; **(b)** EIS spectra with the enlarged Nyquist plot of the HS-SWNH/HEC CE are represented onset.

The influence of binders in carbon-based counter-electrodes has been poorly studied in the literature. It is normally assumed that binders should be burned out to increase the surface area that takes part in the charge-transfer reactions [20, 31, 32], thus increasing the capacitance and the catalytic capabilities of such counter-electrodes. However, the data presented in Table 2.2 show that for all tested materials when annealed at 180 ºC, the addition of HEC causes a decrease of R_{ct} and an increase of the capacitance. The presence of HEC appears to bind together the catalytic particles originating a more uniform and densely packed catalytic film. Consequently, the number of electronic bridges between particles increases, increasing the flow of electrons (lower R_{ct}) and increasing the effective electrically accessible catalytic surface area (higher capacitance). The binding effect of HEC overlaps in this case the blocking effect of some of the active sites. The presence of HEC should also promote a better electrical contact with the FTO [21, 33-35].

The R_{ct} measurements obtained at 0 V show that the CB/HEC is more catalytically active than the SWNH/HEC CE - Table 2.2; however, when analyzing the IV curves - Figure 2.3 (a) – at 0.5 V, their performances seem to be similar. This suggests that both electrodes, if used as CE in a DSC, could yield similar performances, since a DSC's efficiency is evaluated based on its maximum power point (typically for applied potentials higher than 0.4 V).

Table 2.2 also shows the CE performances after annealing at higher temperatures. The SWNH-based CEs were annealed at 400 ºC, since SWNH burn at higher temperatures [26]. This temperature is smaller than 450 °C as normally used for annealing CB [8]. The annealing temperature of 400 ºC / 450 ºC caused the decrease of R_{ct} by 1-2 orders of magnitude for all counter electrodes, except for the HS-SWNH and HS-SWNH/HEC CEs - Table 2.2. This decrease can be attributed to the thermal annealing that makes the CE more electrochemically active [36].

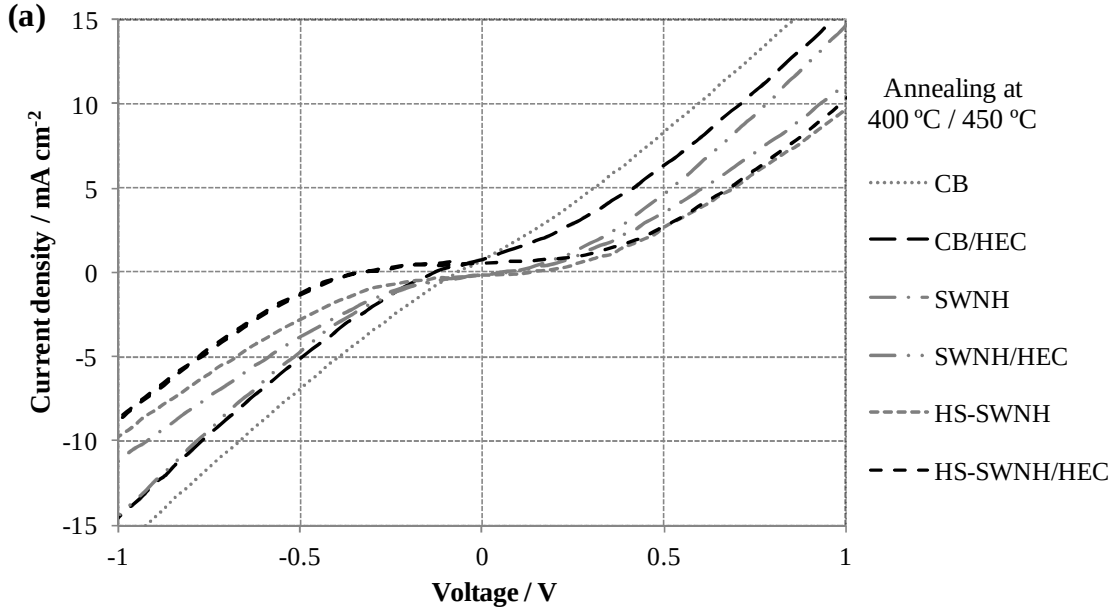

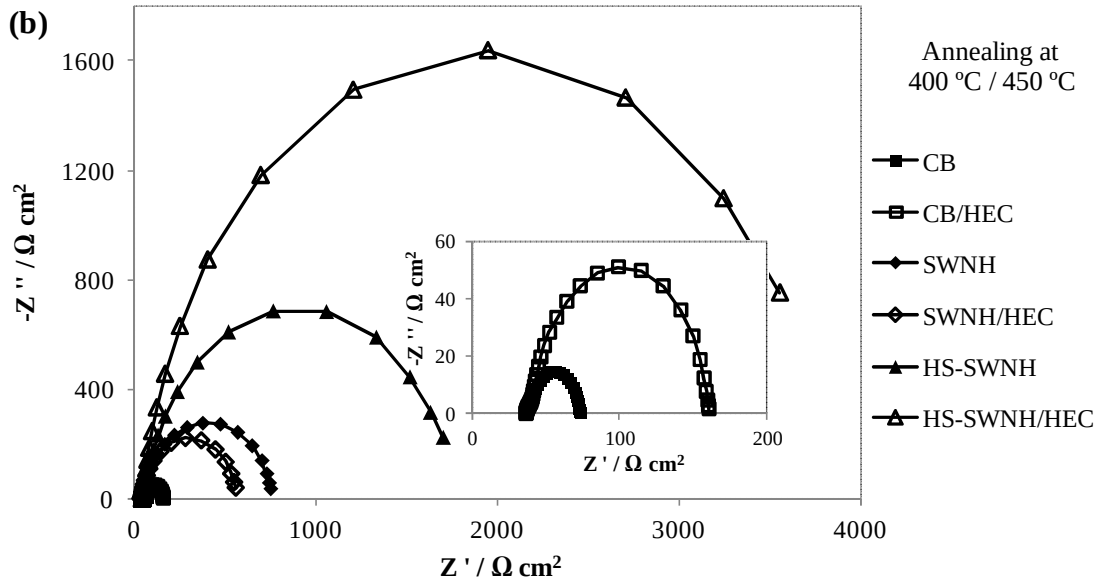

Figure 2.4 Half-cells assembled with Pt free carbon supported counter electrodes annealed at 400 ºC and 450 ºC: **(a)** Current density – voltage measurements; **(b)** EIS spectra with the enlarged Nyquist plots of the CB and CB /HEC CEs are represented onset.

At these high annealing temperatures, CB presented the lowest R_{ct}, (Table 2.2 and Figure 2.4) and yielded the best catalytic performance (Figure 2.4), and is in agreement with other studies [8]. The annealing of CB causes the removal of amorphous material leaving more crystalline edge sites available for the catalysis [8].

The lowest catalytic activities were observed for the HS-SWNH CEs - Table 2.2 and Figure 2.4. Actually, they perform similarly to the HS-SWNH sample annealed at 180 ºC - Table 2.2 and Figure 2.3. This happens because the oxidative pretreatment performed on the HS-SWNH, is somehow equivalent to a thermal annealing treatment, thus rendering this higher temperature annealing somewhat ineffective [26, 36]. The very poor performance exhibited by the HS-SWNH/HEC CE (it was the only one yielding a worse R_{ct} when annealed at 400 ºC) may indicate that some change in the carbon surface has occurred. A similar effect was noticed by Seo *et. al.* when they burned out a cellulose

derivative (carboxymethyl cellulose, CMC) from a highly defective multiwalled carbon nanotubes-based CE and observed that above the decomposition temperature of the CMC the performance of the cells worsened [34].

The influence of HEC presence on samples annealed at 400 ºC / 450 ºC cannot be assessed in a straightforward manner as before, for samples that were annealed at 180 ºC, because in this case the HEC was burned out from the counter electrode. Results for the samples annealed at higher temperatures show that the initial addition of HEC to the samples did not originate a clear decrease in the R_{ct} as it was observed for samples annealed at 180 ºC; on the other hand, the capacitance increased sensibly probably due to an easier access of the electrolyte to the nanostructured catalyst caused by the HEC burn out. However, the burning out of HEC could also have broken some of the electronic bridges between particles, thus decreasing the effective electrically accessible catalyst area. Owing to that the amount of HEC should be optimized to obtain the best CE performance.

Summarizing, the results indicate that SWNH-based CEs show strong limitations for being used in a Pt free CE as in order to have comparable performances to the reference CE ($R_{ct} \leq 10\ \Omega\ cm^2$ [28]), very thick layers (in the order of several tens of μm) are required. In the following section, the use of SWNH as Pt support was evaluated as CE.

2.3.1.2. Pt carbon supported counter electrodes

SWNH provide a good dispersion support for the Pt nanoparticles and conduct well the electric current [24, 26, 27]. Consequently, the use of such composite materials should in principle lead to an efficient catalysis of the iodide/triiodide redox reaction. For comparison purposes CB was also decorated with Pt nanoparticles. An annealing temperature of 180 ºC was used

in the case of these Pt-decorated carbon-based materials, since the presence of Pt nanoparticles lowers the burning temperature (confirmed by thermal gravimetric analysis, not shown here). To compare the different CEs prepared, the parameter R_{ct} was normalized by the amount of Pt used per deposited area, $R_{ct/Pt} = R_{ct}$ x Pt load (with the load of Pt in μgPt cm^{-2}). Likewise, the current density was normalized by the amount of Pt used per deposited area, $I_{/Pt} = I$ x (Pt load)$^{-1}$.

The parameters obtained from fitting the EIS data to the analog electric circuit are shown in Table 2.3, and the $I_{/Pt}$-V curves are shown in Figure 2.5. Data indicate that the best result was achieved for the Pt/SWNH/HEC CE, being the only electrode to display simultaneously a lower $R_{ct/Pt}$ (Table 2.3) and higher $I_{/Pt}$ over all the applied voltage range (Figure 2.5) than the Pt CE.

Table 2.3 Parameters determined by fitting the EIS experimental data to the equivalent circuit – Randles-type circuit, for half-cells assembled with Pt carbon supported counter electrodes. Standard deviation is shown between brackets.

	0 V			
CE	R_{ct} **/ Ω cm^2**	$R_{ct/Pt}$ **/ Ω μgPt**	***CPE:B* / μF cm^{-2}**	***CPE, β***
Pt	4.8 (1.5)	266 (45)	43.9 (3.8)	0.86
Pt/CB	8.8 (1.3)	551 (79)	88.3 (40)	0.85
Pt/CB/HEC	5.5 (1.1)	343 (68)	276 (98)	0.80
Pt/SWNH	10.6 (3.6)	422 (143)	95.4 (7.3)	0.84
Pt/SWNH/HEC	4.1 (0.9)	130 (28)	235 (75)	0.80
Pt/HS-SWNH	22.0 (11.0)	1833 (921)	125 (43)	0.86
Pt/HS-SWNH/HEC	3.8 (0.9)	303 (74)	256.2 (81)	0.81

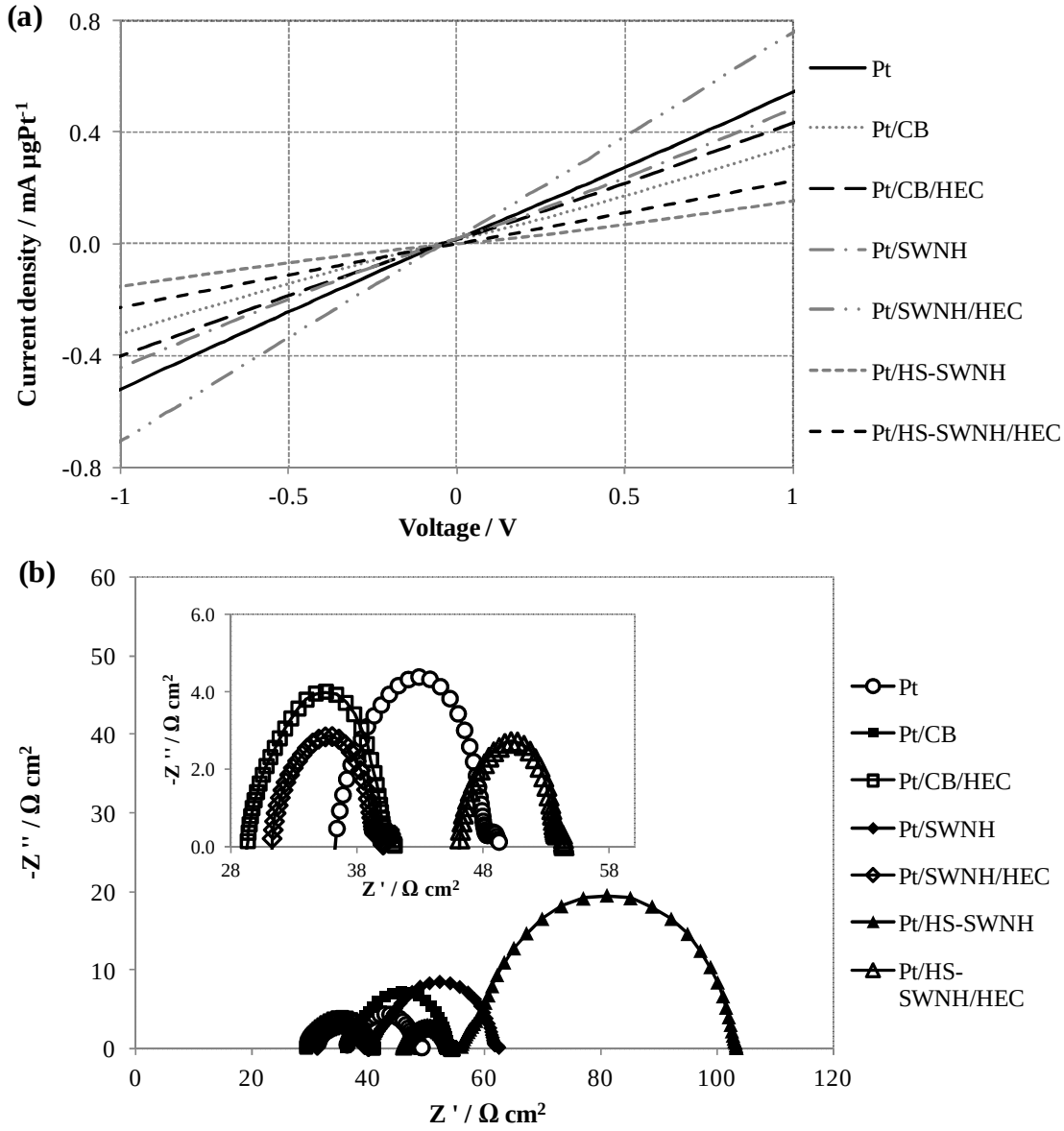

Figure 2.5 Half-cells assembled with Pt carbon supported counter electrodes: **(a)** Current density normalised by the amount of Pt used – voltage measurements; **(b)** EIS spectra with the enlarged Nyquist plots of the Pt, Pt/CB/HE, Pt/SWNH/HEC and Pt/HS-SWNH/HEC CEs are represented onset.

The Pt/HS-SWNH/HEC displays a similar $R_{ct/Pt}$ at 0 V when compared to the Pt/SWNH, but at higher applied potentials the IV curve – Figure 2.5 (a) - shows lower current densities (higher $R_{ct/Pt}$); this should be related to a smaller

electronic conductivity of HS-SWNH when compared to SWNH. The lower electronic conductivity of the HS-SWNH is also evident on the Pt/HS-SWNH CE that presents a very high $R_{ct/Pt}$. This could be explained by the oxidation treatment process, which, although creating more edge sites responsible for catalysis, also creates vacancies and discontinuities in the basal planes of the crystalline structure, thus disrupting the conductive network and consequently decreasing the electronic conductivity of the HS-SWNH [37, 38]. Moreover, oxidation should introduce oxygen-containing functional groups that are known to induce a smaller electronic conductivity [39, 40]. An interesting feature is that the Pt/SWNH/HEC CE allows a 51 % reduction of the Pt load comparatively to the reference Pt CE. When using Pt-decorated SWNH, the metal nanoparticles become the most important moieties responsible for the catalysis; the SWNH, besides providing a good dispersion, also ensure a low electrical resistance, thus facilitating electron transfer/conduction. Since Pt nanoparticles have a high electrocatalytic activity, the support of the Pt-decorated carbon catalysts should have an electronic conductivity as high as possible. Hence, highly oriented carbon materials are preferred, with SWNH exhibiting the best performance as a support material. Furthermore, the addition of HEC helped to create a more uniform and densely packed film providing a better electrical contact with the FTO – Table 2.3. Furthermore, as with the Pt-free carbon CEs, increasing the number of electronically bridged catalyst particles originates R_{ct} to decrease and capacitance to increase – Table 2.3. The Pt/SWNH/HEC CE could therefore be used in devices assembled with temperature-limited substrates that cannot withstand the high-temperature thermal annealing usually required for Pt activation.

In the following section, the use of the Pt/SWNH/HEC CE in a DSC was accessed and compared with a DSC assembled with a conventional Pt CE.

2.3.2. DSC configuration

2.3.2.1. I-V measurements

Figure 2.6 shows the *I-V* characteristic curves for two DSC, one with a traditional Pt CE and the other with the Pt/SWNH/HEC CE. The corresponding photovoltaic parameters (short-circuit current density, J_{sc}; open-circuit voltage, V_{oc}; fill factor, *FF;* and efficiency, η) are summarized on Table 2.4. The results presented in Table 2.4 show that the DSC made with a Pt/SWNH/HEC CE has similar energy conversion efficiency as the DSC assembled with the Pt CE (the relative efficiency, $\Delta\eta$, difference is -0.54 %). EIS results showed in the section 2.3.1.2 indicate that Pt/SWNH/HEC CE should have yielded a DSC with a better performance than one with the Pt CE as a consequence of the smaller $R_{ct/Pt}$ and higher $I_{/Pt}$. However, by accessing the relative catalytic merit of both CEs using the product of R_{ct} and capacitance [20], the higher capacitance displayed by the Pt/SWNH/HEC CE (influenced by the amount of catalyst surface area) appears to have undermined the overall catalytic capability. As a result a DSC was yielded having a similar performance as one assembled with the Pt CE.

Table 2.4 Photovoltaic parameters for the DSC assembled with a Pt CE and the Pt/SWNH/HEC CE. Standard deviation is shown between brackets.

CE	V_{OC} / V	J_{SC} / mA cm^{-2}	*FF*	η / %
Pt	0.72 (0.01)	6.91 (0.67)	0.63 (0.03)	3.09 (0.28)
Pt/SWNH/HEC	0.71 (0.01)	6.85 (0.22)	0.64 (0.01)	3.08 (0.19)

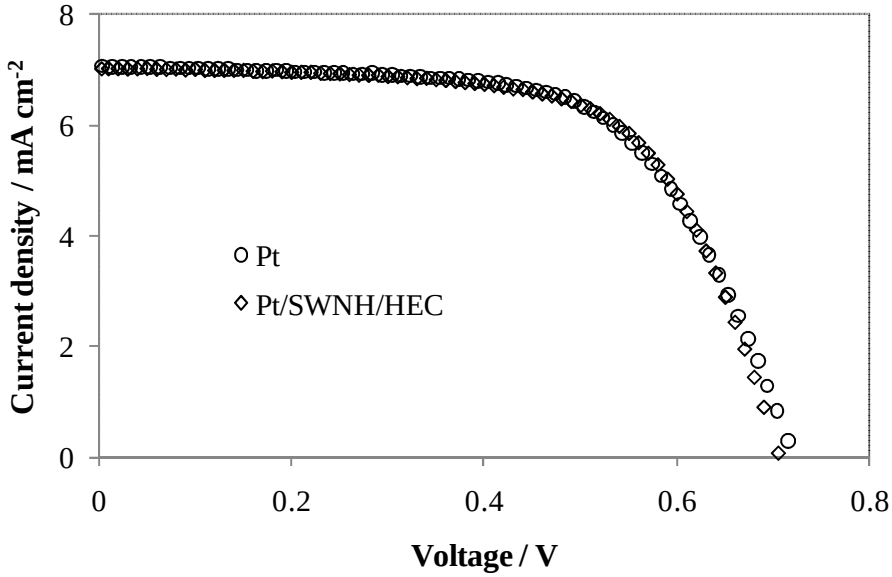

Figure 2.6 *I-V* characteristics measured at 1 sun light intensity (100 mW·m^{-2}; AM 1.5 G) for DSCs assembled with a Pt CE and a Pt/SWNH/HEC CE.

For carbonaceous CEs to have comparable efficiencies to a Pt CE, they are required to be several µm thick [6, 8], thus rendering them opaque. In our case, the use of SWNH decorated with Pt yielded a semi-transparent CE -

Figure **2.7**. The transmittance spectrum of the DSCs based on Pt/SWNH/HEC and Pt counter electrodes are compared in Figure 2.8. The transmittance, *T*, was measured at 700 nm where the transmittance is maximum for the dye used – N719 [41]. It was determined that the DSC made with the Pt/SWNH/HEC CE has a relative transmittance, Δ*T*, of ca. 50 % less than the DSC made with the Pt CE (31.4 % vs. 61.4%). Additionally, Figure 2.8 shows that, within the range of the wavelengths of the visible light, only 50 % of it passes through the DSC assembled with the Pt/SWNH/HEC CE when compared with the DSC made with the Pt CE.

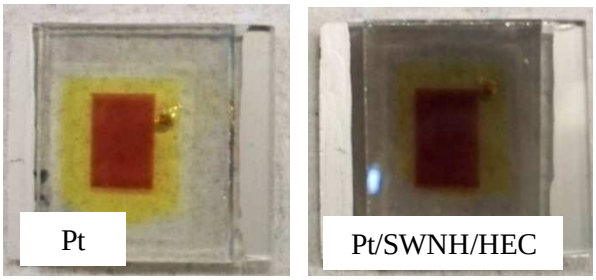

Figure 2.7 DSCs assembled with a Pt CE and a Pt/SWNH/HEC CE.

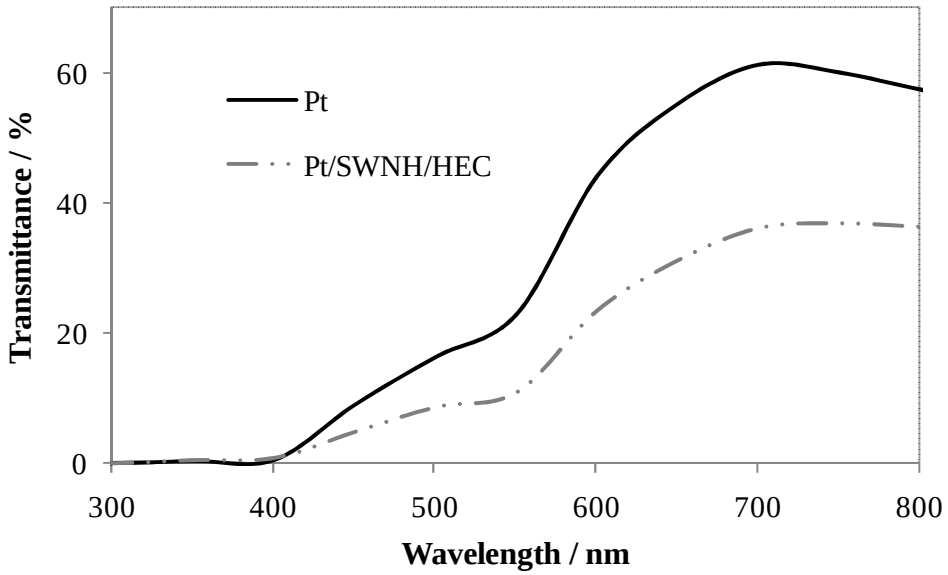

Figure 2.8 Transmittance spectra of DSCs assembled with a Pt CE and a Pt/SWNH/HEC CE. At 700 nm, DSCs assembled with a Pt and Pt/SWNH/HEC CEs have transmittances of 61.4 % and 31.4 % respectively.

These results show that a DSC assembled with a CE comprised of SWNH doped with Pt nanoparticles and mixed with 10 wt.% of HEC, yields the same energy conversion efficiency as a DSC prepared with a Pt CE, while reducing the CE's Pt load by ca. 50 %, and having half the transparency. Furthermore the Pt/SWNH/HEC CE could be applied to temperature-sensitive substrates (such as polymeric substrates) without compromising the device's performance.

2.4. Conclusions

The use of SWNH as CEs in DSC was investigated. High surface SWNH, obtained by oxidative treatment, mixed with 10 wt.% of HEC yielded a promising no-annealed CE that could be used in temperature-limited applications. However a several tens of μm-thick film should be required in order to perform comparably to a Pt CE. Higher annealing temperatures (above 400 °C) do not favor SWNH-based CEs, performing even worse than when compared with other carbonaceous materials such as carbon black.

On the other hand, SWNH can be used as a Pt electrocatalyst support as they ensure a good electrochemical activity while minimizing the amount of Pt required for the reduction of the triiodide ions. SWNH decorated with Pt nanoparticles and mixed with 10 wt.% of HEC showed the highest electrocatalytic activity for the iodide/triiodide redox reaction. A DSC fabricated with a Pt/SWNH/HEC CE yielded the same energy conversion efficiency as one assembled with a Pt CE, despite being loaded with only ca. 50 % of Pt. However, the DSC fabricated with a Pt/SWNH/HEC CE showed half of the transparency exhibited by the DSC assembled with a Pt CE. Furthermore the Pt/SWNH/HEC CE has the potential to be used in temperature-limited devices since it requires a low annealing temperature (180 °C). The presence of HEC seems to have a positive effect on the overall catalytic behavior of both Pt free carbon-based and Pt carbon supported CEs when annealed at low temperatures (ca. 180 °C).

Acknowledgments

R. Cruz is grateful to the Portuguese Foundation for Science and Techonology (FCT) and Efacec – Engenharia e Sistemas S.A. for his Ph.D grant (reference: SFRH/BDE/33439/2008). L. Brandão is grateful to FCT for

her post-doc grant (reference SFRH/BPD/41233/2007). This work was accomplished under the project SolarSel - SI IDT - 3423/2008, co-financed by the European Union and the Portuguese Government through ADI – Agência de Inovação, in the framework of the QREN Initiative and the European Regional Development Fund through the Operational Program for Competitiveness Factors.

References

1. Toivola, M., J. Halme, K. Miettunen, K. Aitola, and P.D. Lund, *Nanostructured dye solar cells on flexible substrates-Review.* International Journal of Energy Research, 2009. **33**(13): p. 1145-1160.
2. Mao, S.S. and X.B. Chen, *Selected nanotechnologies for renewable energy applications.* International Journal of Energy Research, 2007. **31**(6-7): p. 619-636.
3. Guo, K.W., *Green nanotechnology of trends in future energy: a review.* International Journal of Energy Research, 2012. **36**(1): p. 1-17.
4. O'Regan, B. and M. Grätzel, *A Low-Cost, High-Efficiency Solar-Cell Based on Dye-Sensitized Colloidal TiO_2 Films.* Nature, 1991. **353**(6346): p. 737-740.
5. Smestad, G., C. Bignozzi, and R. Argazzi, *Testing of dye sensitized TiO2 solar cells I: Experimental photocurrent output and conversion efficiencies.* Solar Energy Materials and Solar Cells, 1994. **32**(3): p. 259-272.
6. Murakami, T. and M. Grätzel, *Counter electrodes for DSC: Application of functional materials as catalysts.* Inorganica Chimica Acta, 2008. **361**(3): p. 572-580.
7. Kitamura, T., M. Maitani, M. Matsuda, Y. Wada, and S. Yanagida, *Improved Solid-State Dye Solar Cells with Polypyrrole using a Carbon-Based Counter Electrode.* Chemistry Letters, 2001. **30**(10): p. 1054-1055.
8. Murakami, T.N., S. Ito, Q. Wang, M.K. Nazeeruddin, T. Bessho, I. Cesar, P. Liska, R. Humphry-Baker, P. Comte, P. Pechy, and M. Gratzel, *Highly efficient dye-sensitized solar cells based on carbon*

black counter electrodes. Journal of The Electrochemical Society, 2006. **153**(12): p. A2255-A2261.

9. Kay, A. and M. Grätzel, *Low cost photovoltaic modules based on dye sensitized nanocrystalline titanium dioxide and carbon powder.* Solar Energy Materials and Solar Cells, 1996. **44**(1): p. 99-117.
10. Denaro, T., V. Baglio, M. Girolamo, V. Antonucci, A.S. Arico, F. Matteucci, and R. Ornelas, *Investigation of low cost carbonaceous materials for application as counter electrode in dye-sensitized solar cells.* Journal of Applied Electrochemistry, 2009. **39**(11): p. 2173-2179.
11. Imoto, K., K. Takahashi, T. Yamaguchi, T. Komura, J. Nakamura, and K. Murata, *High-performance carbon counter electrode for dye-sensitized solar cells.* Solar Energy Materials and Solar Cells, 2003. **79**(4): p. 459-469.
12. Cha, S.I., B.K. Koo, S.H. Seo, and D.Y. Lee, *Pt-free transparent counter electrodes for dye-sensitized solar cells prepared from carbon nanotube micro-balls.* Journal of Materials Chemistry, 2009. **20**(4): p. 659-662.
13. Chou, C.-S., R.-Y. Yang, M.-H. Weng, and C.-I. Huang, *The applicability of SWCNT on the counter electrode for the dye-sensitized solar cell.* Advanced Powder Technology, 2009. **20**(4): p. 310-317.
14. Ramasamy, E., W.J. Lee, D.Y. Lee, and J.S. Song, *Spray coated multi-wall carbon nanotube counter electrode for tri-iodide (I_3-) reduction in dye-sensitized solar cells.* Electrochemistry Communications, 2008. **10**(7): p. 1087-1089.
15. Suzuki, K., M. Yamaguchi, M. Kumagai, and S. Yanagida, *Application of Carbon Nanotubes to Counter Electrodes of Dye-sensitized Solar Cells.* Chemistry Letters, 2003. **32**(1): p. 28-29.

16. Hong, W.J., Y.X. Xu, G.W. Lu, C. Li, and G.Q. Shi, *Transparent graphene/PEDOT-PSS composite films as counter electrodes of dye-sensitized solar cells.* Electrochemistry Communications, 2008. **10**(10): p. 1555-1558.

17. Roy-Mayhew, J.D., D.J. Bozym, C. Punckt, and I.A. Aksay, *Functionalized Graphene as a Catalytic Counter Electrode in Dye-Sensitized Solar Cells.* Acs Nano, 2010. **4**(10): p. 6203-6211.

18. Choi, H., H. Kim, S. Hwang, W. Choi, and M. Jeon, *Dye-sensitized solar cells using graphene-based carbon nano composite as counter electrode.* Solar Energy Materials and Solar Cells, 2011. **95**(1): p. 323-325.

19. Liang, M.H., B. Luo, and L.J. Zhi, *Application of graphene and graphene-based materials in clean energy-related devices.* International Journal of Energy Research, 2009. **33**(13): p. 1161-1170.

20. Aitola, K., J. Halme, N. Halonen, A. Kaskela, M. Toivola, A.G. Nasibulin, K. Kordás, G. Tóth, E.I. Kauppinen, and P.D. Lund, *Comparison of dye solar cell counter electrodes based on different carbon nanostructures.* Thin Solid Films, 2011. **519**(22): p. 8125-8134.

21. Li, P.J., J.H. Wu, J.M. Lin, M.L. Huang, Y.F. Huang, and Q.G. Li, *High-performance and low platinum loading Pt/Carbon black counter electrode for dye-sensitized solar cells.* Solar Energy, 2009. **83**(6): p. 845-849.

22. Huang, K.C., Y.C. Wang, R.X. Dong, W.C. Tsai, K.W. Tsai, C.C. Wang, Y.H. Chen, R. Vittal, J.J. Lin, and K.C. Ho, *A high performance dye-sensitized solar cell with a novel nanocomposite film of PtNP/MWCNT on the counter electrode.* Journal of Materials Chemistry, 2010. **20**(20): p. 4067-4073.

23. Antisari, M.V., D.M. Gattia, L. Brandao, R. Marazzi, and A. Montone, *Carbon Nanostructures produced by an AC Arc Discharge.* Thermec 2009, Pts 1-4, 2010. **638-642**: p. 1766-1771.

24. Brandão, L., D.M. Gattia, R. Marazzi, M.V. Antisari, S. Licoccia, A. D'Epifanio, E. Traversa, and A. Mendes, *Improvement of DMFC Electrode Kinetics by using Nanohorns Catalyst Support.* Materials Science Forum, 2010. **638-642**: p. 1106-1111.

25. Trancik, J.E., S.C. Barton, and J. Hone, *Transparent and catalytic carbon nanotube films.* Nano Letters, 2008. **8**(4): p. 982-987.

26. Brandão, L., M. Boaventura, C. Passeira, D.M. Gattia, R. Marazzi, M.V. Antisari, and A. Mendes, *An Electrochemical Impedance Spectroscopy Study of Polymer Electrolyte Membrane Fuel Cells Electrocatalyst Single Wall Carbon Nanohorns-Supported.* Journal of Nanoscience and Nanotechnology, 2011. **11**(10): p. 9016-9024.

27. Brandão, L., C. Passeira, D. Mirabile Gattia, and A. Mendes, *Use of single wall carbon nanohorns in polymeric electrolyte fuel cells.* Journal of Materials Science, 2011. **46**(22): p. 7198-7205.

28. Hauch, A. and A. Georg, *Diffusion in the electrolyte and charge-transfer reaction at the platinum electrode in dye-sensitized solar cells.* Electrochimica Acta, 2001. **46**(22): p. 3457-3466.

29. Wang, H., M. Chhowalla, N. Sano, S. Jia, and G.A.J. Amaratunga, *Large-scale synthesis of single-walled carbon nanohorns by submerged arc.* Nanotechnology, 2004. **15**(5): p. 546-550.

30. Sano, N., *Low-cost synthesis of single-walled carbon nanohorns using the arc in water method with gas injection.* Journal of Physics D-Applied Physics, 2004. **37**(8): p. L17-L20.

31. Mei, X., S.J. Cho, B. Fan, and J. Ouyang, *High-performance dye-sensitized solar cells with gel-coated binder-free carbon nanotube films as counter electrode.* Nanotechnology, 2010. **21**(39): p. 395202.

32. Li, K.X., Y.H. Luo, Z.X. Yu, M.H. Deng, D.M. Li, and Q.B. Meng, *Low temperature fabrication of efficient porous carbon counter electrode for dye-sensitized solar cells.* Electrochemistry Communications, 2009. **11**(7): p. 1346-1349.

33. Zhang, D.W., X.D. Li, H.B. Li, S. Chen, Z. Sun, X.J. Yin, and S.M. Huang, *Graphene-based counter electrode for dye-sensitized solar cells.* Carbon, 2011. **49**(15): p. 5382-5388.

34. Seo, S.H., S.Y. Kim, B.-K. Koo, S.-I. Cha, and D.Y. Lee, *Influence of electrolyte composition on the photovoltaic performance and stability of dye-sensitized solar cells with multiwalled carbon nanotube catalysts.* Langmuir, 2010. **26**(12): p. 10341-10346.

35. Khelashvili, G., S. Behrens, A. Hinsch, W. Habicht, D. Schild, A. Eichhöfer, R. Sastrawan, K. Skupien, E. Dinjus, and H. Bönnemann, *Preparation and characterization of low platinum loaded Pt:SnO2 electrocatalytic films for screen printed dye solar cell counter electrode.* Thin Solid Films, 2007. **515**(7-8): p. 4074-4079.

36. Ermete, A., *Carbon supports for low-temperature fuel cell catalysts.* Applied Catalysis B: Environmental, 2009. **88**(1–2): p. 1-24.

37. Xu, S., Y. Luo, and W. Zhong, *Investigation of catalytic activity of glassy carbon with controlled crystallinity for counter electrode in dye-sensitized solar cells.* Solar Energy, 2011. **85**(11): p. 2826-2832.

38. Bai, H., C. Li, and G. Shi, *Functional Composite Materials Based on Chemically Converted Graphene.* Advanced Materials, 2011. **23**(9): p. 1089-1115.

39. Wang, X., L.J. Zhi, and K. Mullen, *Transparent, conductive graphene electrodes for dye-sensitized solar cells.* Nano Letters, 2008. **8**(1): p. 323-327.

40. Wang, S.J., Y. Geng, Q. Zheng, and J.-K. Kim, *Fabrication of highly conducting and transparent graphene films.* Carbon, 2010. **48**(6): p. 1815-1823.

41. Yoon, S., S. Tak, J. Kim, Y. Jun, K. Kang, and J. Park, *Application of transparent dye-sensitized solar cells to building integrated photovoltaic systems.* Building and Environment, 2011. **46**(10): p. 1899-1904.

Chapter 3

Reduced graphene oxide films as transparent counter-electrodes for dye-sensitized solar cells

Rui Cruz, David Alfredo Pacheco Tanaka, Adélio Mendes

(Solar Energy, 2012. 86(2): p. 716-724., DOI: 10.1016/j.solener.2011.11.010)

Abstract

Stand-alone graphene-based films were prepared from graphene oxide (GO) nanoplatelets and their use as counter-electrodes (CEs) in dye-sensitized solar cells (DSCs) was investigated. The graphene-based CEs were produced by spray deposition of GO and chemically reduced GO, followed by thermal annealing under an inert atmosphere. These GO-based CEs were shown to have similar transparency as a reference CE made of Pt. Consistent with impedance data from symmetrical half-cells, DSCs assembled with such GO-based CEs exhibited relative efficiencies of ca. 75 % comparatively to the reference Pt CE. The possibility of obtaining transparent (transmittance higher than 80 %) and reasonable catalytic films for DSCs (energy conversion efficiency of 2.64 %) from GO nanoplatelets was demonstrated. The need for reduction of the graphene oxide nanoplatelets prior to deposition was not observed, allowing for a simplified CE manufacturing process. However, further work is still needed to equal or surpass the performance of Pt CEs.

Keywords: Dye-sensitized solar cell; Graphene oxide; Transparent counter-electrode; Annealing; Thermal reduction.

3.1. Introduction

In the last few years, the interest in dye-sensitized solar cells (DSCs) has grown considerably as they are seen as a promising alternative to conventional photovoltaic devices for producing electrical power due to their potential for low production costs.

A conventional DSC comprises [1]: a dye-absorbed mesoporous nanocrystalline TiO_2 film deposited onto a transparent conductive oxide (TCO) coated glass substrate, an iodide/triiodide redox couple-based electrolyte and a TCO coated glass substrate covered by a catalytic material acting as a the counter-electrode (CE). The CE plays a key role in DSC as it receives electrons from the external circuit and reduces (electrocatalyzes) the redox species in the electrolyte used for regenerating the sensitizer after electron injection. The CE is usually made of a thin layer of platinum (Pt); however, due to the scarcity nature of this noble metal [2], it is important to develop new low-cost CEs using materials that are simultaneously abundant, non-toxic and capable of yielding DSCs of relatively high conversion efficiency. An ideal CE should have low electrical resistance and high electrocatalytic activity towards the iodide/triiodide (I^- / I_3^-) redox reaction, while being stable and as transparent as possible. Transparency is not mandatory but offers added value to numerous applications (facades, windows, roof panels, etc.). Moreover it enables its use in other applications, such as tandem cells [3, 4].

In this paper we report stand-alone graphene CEs yielding similar transparencies and relative efficiencies of ca. 75 % comparatively to a Pt CE. The graphene-based CEs were produced from depositing both GO and chemically RGO over a TCO coated glass substrate, followed by annealing under an inert atmosphere. The obtained results suggest that efficient and transparent graphene counter electrodes can be obtained directly from GO nanoplatelets, thus reducing the complexity of the manufacturing process. Further optimization of the manufacturing procedure is under study.

3.2. Material and Methods

3.2.1. Preparation of graphene oxide and chemically reduced graphene oxide

The production of graphene oxide was carried out using the modified Hummer's method [5, 6]. Graphite was added to a solution of H_2SO_4 at room temperature; the solution was cooled at 0 °C using an ice bath and then $KMnO_4$ was added gradually. The mixture was heated at 35 °C and stirred for 2 h. After that, water was added into the mixture at 0 °C (ice bath). Then H_2O_2 (30 %) was added until no gas is produced. The solid was filtered, washed with HCl (0.1 M) and water. The graphene oxide was dried under vacuum at room temperature for 24 h and then triturated using a mortar. The as-prepared GO powder, was first exfoliated in water, for 4 h in a basic pH (ca. 9), with the help of NH_3, 6 M, using an ultrasonic bath. Then, the GO aqueous colloid was centrifuged twice at 5000 rpm for 30 min. To chemically reduce the graphite oxide platelets, hydrazine (N_2H_4 in water, 2 M) and NH_3, 6 M, were added to a GO solution and stirred for 30 min. Then the mixture was heated at 90 ºC for 3 h and afterwards centrifuged at 5000 rpm for 30 min to remove aggregates and larger sheets. According to particle size distribution analysis (data not shown here), GO and chemically RGO platelets had diameters of ca. 2 µm.

3.2.2. Counter-electrode and half-cell (symmetric dummy cell) fabrication

For all CEs, conductive fluorine-doped tin oxide (FTO) coated glass substrates (2 mm-thick, 2.5 cm x 2.5 cm, sheet resistance 15 $\Omega \cdot \text{square}^{-1}$, Dyesol) were used. Prior to use, FTO-coated glass substrates were washed in an ultrasonic bath with detergent (Alconox, VWR) for 60 min and then ethanol for 45 min. The CE based on Pt (Pt CE) was prepared by depositing a Pt paste (Pt-Catalyst T/ SP, Solaronix) onto the entire surface of the conductive glass using doctor-blade, followed by heat treatment at 400 °C for 15 min. Graphene-based

CEs were prepared by spray deposition using a Revell 39101 airbrush, with the aid of a compressed flow of reconstituted air. Distance between the substrate and the spray nozzle was approximately 10 cm. GO and chemically reduced GO ethanolic suspensions with a concentration of 0.06 mg catalytic material per gram of suspension, were prepared from aqueous colloids of both materials. These ethanolic suspensions exhibited a negligible sedimentation. The suspensions were sprayed onto the conductive glass substrates placed on a pre-heated hot-plate at ca. 120 ºC. The films were then annealed for 60 min at 400 ºC under an inert atmosphere. The CE formed by deposition of GO and posterior annealing is referred hereinafter as annealed GO, or AGO; the CE prepared by deposition of chemically RGO and posterior annealing is referred hereinafter as annealed RGO, or ARGO. The AGO and ARGO load applied to each electrode was ca. 0.01 mg cm^{-2}.

A half-cell configuration, consisting of two identical FTO-coated glass substrates coated with the catalytic materials [7], was used for the electrochemical impedance spectroscopy (EIS) study. The half-cell was sealed with a 25-µm thick Surlyn frame (Solaronix) at 100 ºC for 15 s. After sealing, the cells were filled with an iodide based electrolyte solution (organic iodide salt, 10 - 30 wt.%, iodine 10 wt.%, inorganic iodide salt 10 wt.%, imidazole compound 10 wt.% in 3-methoxypropionitrile 60 wt.%, EL-HSE, Dyesol) through a pre-drilled 1 mm diameter hole. These holes were then sealed using a melted Surlyn disc and a thin glass lamella. The active area, i.e., the area of the electrode in contact with the electrolyte, was 3 cm^2. Half-cells were assembled in duplicate for each catalytic material and reproducibility assessed.

3.2.3. Dye-sensitized solar cell fabrication

DSCs with an active area of 0.6 cm^2 were fabricated according to the following procedure: FTO-coated glass substrates (2 mm-thick, 2.5 cm x 1.8 cm) were washed in an ultrasonic bath with detergent (Alconox, VWR) and then ethanol. A TiO_2 electrode (photoanode) with a thickness of ca. 4-6 µm,

was obtained by spreading a TiO_2 paste (20-nm sized TiO_2 particles, DSL18R-T - Dyesol) onto the conducting glass using the doctor blade technique. The deposited paste was sintered in air at 500 ºC for 30 min. After cooling to 70 ºC, the TiO_2 electrode was sensitized by immersing it in a N719 dye solution (0.3 mM in ethanol, Dyesol) at room temperature for more than 12 h. Afterwards the dye-sensitized electrode was rinsed with ethanol and dried in moisture-free environment. Pt and graphene-based CEs were prepared as described above (in section 3.2). Each specimen was prepared in duplicate. The photoanode and the counter-electrode were sealed with a 25-µm thick Surlyn frame at 100 ºC for 15 s. After sealing, the cells were filled with an electrolyte solution (iodide based, EL-HSE Dyesol, Dyesol) through a pre-drilled 1 mm diameter hole done in the counter-electrode side. The hole was sealed using a melted Surlyn disc and a thin glass lamella. Reproducibility was achieved for all DSCs.

3.2.4. Transmittance measurements

Transmittance measurements of the different CEs were carried out using an UV/VIS/NIR spectrophotometer (Lambda 750, Perkin Elmer). Graphene and Pt films were deposited on bare and FTO-covered glass substrates. Measurements were taken from the coated side. The relative difference in transmittance between the DSC made with graphene-based CEs and the Pt-DSC, $\Delta\tau_{550nm}$, was calculated based on transmittance measured at a wavelength of 550 nm , τ_{550nm}, according to the following equation:

$$\Delta\tau_{550nm} = \frac{\tau_{550nm,grapheneCE} - \tau_{550nm,Pt}}{\tau_{550nm,Pt}} x100 \quad (3.1)$$

3.2.5. Half-cell and dye-sensitized solar cell characterization

The half-cells (HCs) were characterized by electrochemical impedance spectroscopy (EIS). EIS experiments were carried out with a ZENNIUM workstation (Ref. 2425-C, Zahner Elektrik, Germany). The frequency range was 100 mHz-100 kHz and the magnitude of the modulation signal was 10 mV.

All the measurements were performed at room temperature in the dark at 0 V and 0.4 V. A ZView software (Scribner Associates Inc.) was used to process the EIS data. Current density–voltage (*I-V*) measurements were also carried out in the dark with a scan rate of 100 mV s^{-1} ranging from – 1 V to 1 V.

DSCs were characterized by measuring their current density-voltage (*I-V*) characteristics and EIS. For I-V characterization a 150 W xenon light source (Oriel class A solar simulator, Newport USA) irradiating 100 mW cm^{-2} (1 sun light-intensity) at the surface of the DSC and equipped with an air mass filter of 1.5 (Newport, USA) was used. The simulator was calibrated using a single crystal Si photodiode (Newport, USA). The *I-V* characteristics were obtained applying an external potential bias and measuring the generated photocurrent. The photovoltaic parameters (short-circuit current density, J_{sc}; open-circuit voltage, V_{oc}; fill factor, *FF*) were extracted from the *I-V* curve and used to calculate the DSC's efficiency, η:

$$\eta = \frac{V_{OC} J_{SC} FF}{I_S} x100 \tag{3.2}$$

where I_S is the intensity of the incident light. The relative difference in energy conversion efficiency, $\Delta\eta$, between the DSC made with graphene-based CEs and the Pt-DSC was calculated according to the following equation:

$$\Delta\eta = \frac{\eta_{grapheneCE} - \eta_{Pt}}{\eta_{Pt}} x100 \tag{3.3}$$

For EIS characterization, a ZENNIUM workstation (Ref. 2425-C, Zahner Elektrik, Germany) was used. These measurements were performed at room temperature at 0.8 V (close to typical open-circuit voltages), in dark conditions.

3.3. Results and discussion

Graphene with structural defects and oxygen-functional groups attached can be used as a stand-alone material for making DSC's CE. Graphene defects and functional groups promote the electrocatalysis [8-15] while the graphene platelets are good electronic conductors [16]. In this work, CE based on graphene oxide of two types, RGO and GO, were prepared and critically compared with a reference Pt CE.

The use of GO solutions, rather than using RGO, would render a less complex method of preparing CEs. Due to the good solubility properties of GO, it is easier to control the characteristics of the solution to be deposited (concentration, etc.) hence providing a tighter control in the final characteristics of the CE film. Furthermore, the tuning of the surface characteristics (such as morphology or wettability) is possible upon the use of different solvents [17] or treatments, such as exposure to an argon plasma [13]. Spray deposition of ethanolic suspensions yields the most reproducible results, allowing for a relatively easy deposition; this technique combines small droplet size with rapid evaporation avoiding the concentration process that takes place upon slow solvent loss [9, 18].

3.3.1. Transmittance measurements

Graphene films were deposited on FTO-coated glass and bare glass. Bare glass was used to assess possible interferences caused by the FTO surface on the graphene films. Transmittance of the different CEs was evaluated and the results are shown in Figure 3.1.

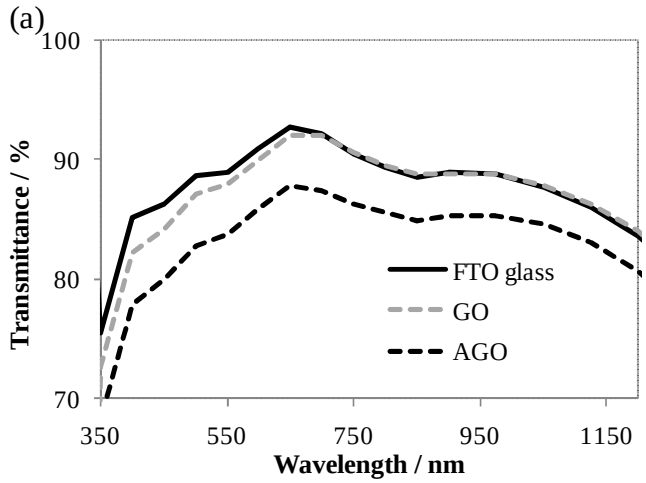
(a)
100
90
80
70
Transmittance / %
350
550
750
950
1150
Wavelength / nm
FTO glass
GO
AGO

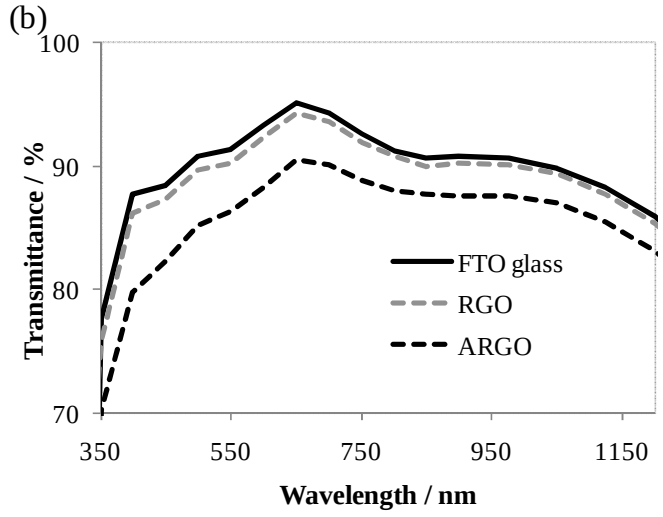
(b)
100
90
80
70
Transmittance / %
350
550
750
950
1150
Wavelength / nm
FTO glass
RGO
ARGO

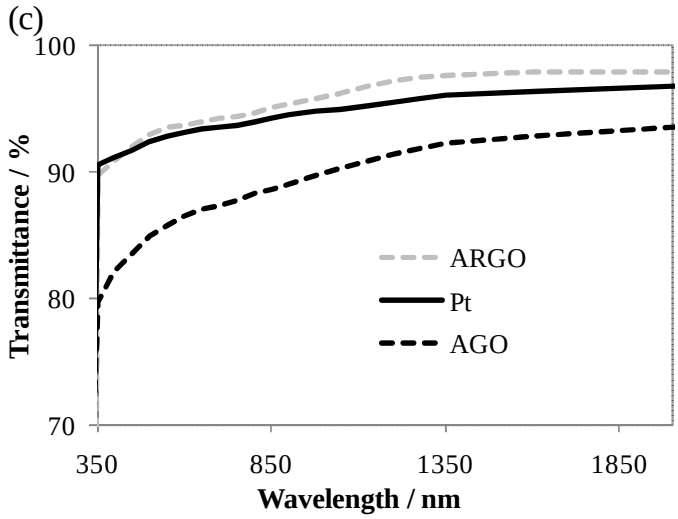

Figure 3.1 Transmittance spectra of the CEs made of different materials: (a) GO before and after annealing (AGO) on FTO-coated glass substrate; (b) chemically reduced GO (RGO) before and after annealing (ARGO) on FTO-coated glass substrate; (c) Pt, ARGO and RGO on bare glass.

Figure 3.1 (a) and (b) show the same trend for both types of graphene films concerning transparency, which decreased after annealing. Annealing the graphene films under inert atmospheres favours the elimination of oxygen functional groups due to thermal-induced decomposition, partially restituting the electronic conjugation [13, 19]. Furthermore, annealing enables a better ordering of graphene sheets; accordingly, the films become denser and smother, with a lower surface roughness [20], and thus less transparent. The graphene films were also proved to be very transparent for a very large wavelength region (Vis and near infrared) - Figure 3.1 (c). Table 3.1 summarises the results obtained for AGO, ARGO and Pt films prepared on bare and FTO-coated glass substrates, for transmittance measured at a wavelength of 550 nm, τ_{550nm} [9, 20]. Results indicate that FTO does not cause any kind of optical interference when graphene sheets are attached on top of it. Both graphene films exhibit a high transmittance compared to the Pt film, with the ARGO film being even more transparent than the reference CE. The ARGO film exhibits a higher

transparency compared with the AGO film. A possible reasoning is that as the GO platelets have a greater solubility, the material is less likely to form bundles when sprayed; the GO platelets would therefore be better dispersed, forming a more cohesive film with less openings through which light could travel through. Besides the restacking of the graphene sheets to a denser state that takes place during the annealing, the GO film also loses oxygen functional groups yielding sp^2 character which is more graphitized and ergo less transparent [20]. However, the exact extent of these two phenomena was not determined as it was not within the scope of this work.

Table 3.1 Transmittance measured at 550 nm, τ_{550nm}, for the tested CEs deposited on different substrates

	$\tau_{550\ nm}$ / %		
CE	**On bare**	**On FTO**	**$\Delta\tau_{550\ nm}$ / %**
Pt	93	85	---
ARGO	94	86	1.3
AGO	89	81	-4.4

3.3.2. Electrochemical impedance spectroscopy of half-cells

Electrochemical impedance spectroscopy (EIS) was used to assess the catalytic activity of ARGO, AGO and Pt CEs assembled in half-cells. Measurements were taken at room temperature, in the dark, at bias voltages of 0 V and 0.4 V. The reference CE made of Pt is normally characterized at 0 V because the sensitivity of the characterization method is maximum [7]. However, graphene CE has especial charge carrier mobility behaviour [16] that makes desirable to assess its catalytic activity closer to a DSC's real operating conditions, i.e. at a potential difference between 0.4 V and 0. 6 V (typical maximum power point). For example, Kavan *et al.*[21] reported half-cells made

of graphene CEs exhibiting a charge transfer resistance ca. 50 – 100 times higher than made of Pt CE, while the correspondent DSC had a relative difference in efficiency of only less 27.5 % (Pt based cell is more efficient).

The half-cell's EIS spectra were fitted to the electrical analogue shown in Figure 3.2, based on the Randles-type circuit:

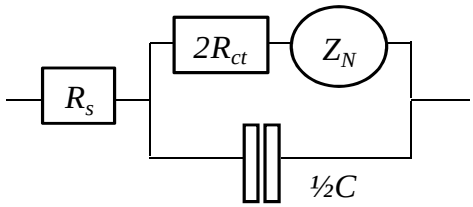

Figure 3.2 Electrical analogue used for fitting the electrochemical impedance spectra data of half-cells.

In Figure 3.2, R_s, is the series resistance, including the TCO's sheet resistance and the cell's contact resistances. The catalytic regeneration of triiodide at the counter-electrode is characterized by parameters R_{ct} and C, the charge transfer resistance and the capacitance of the electrical double layer at the electrodes, respectively. In the same electrical analogue is also represented the diffusion of triiodide within the electrolyte solution, described by the Nernst diffusion impedance Z_N. Due to non-idealities, the capacitance was replaced by a constant phase element, *CPE* [7]. Good agreement was achieved for all samples between the measured and fitted data. The fitting of the EIS experimental data was accomplished with ZView® software (Scribner Associates Inc.). Additionally, *I-V* measurements were carried out in order to observe the behaviour of the CEs at different voltages. An ideal CE should exhibit a great catalytic activity and high electroactivity/low overpotential and transparency. Experimentally, this means that the CEs should have a low charge transfer resistance (R_{ct}) since it is directly related to the ability of the material to catalyse the reduction of I_3^- at the CE/electrolyte interface; regarding the CE's

capacitance, since it represents the ability of the film to quickly reduce the electrolyte, it should be also as low as possible.

Figure 3.3 shows the Nyquist diagrams of CEs in half-cell configuration at two bias (0V and 0.4 V). Left-hand side semicircles correspond to high-frequency measurements (more than 10 Hz) and reflect the charge-transfer resistance and double layer capacitance of the counter-electrode; while right-hand side semicircles (when present) result from low-frequency measurements (less than 10 Hz) and are associated with the Nernst diffusion impedance. Contrary to the Pt CE, when no bias is applied the graphene CEs show no Nernst diffusion impedance (Z_N) [8, 21]. However, as bias increases, a second low range frequency semicircle, corresponding to the Nernst diffusion, becomes apparent [8].

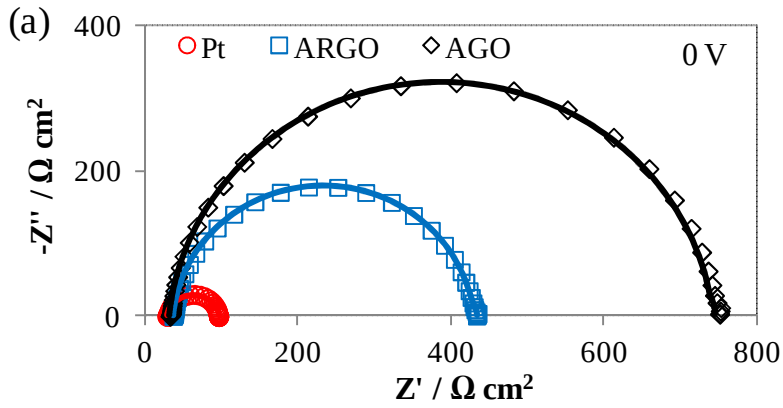

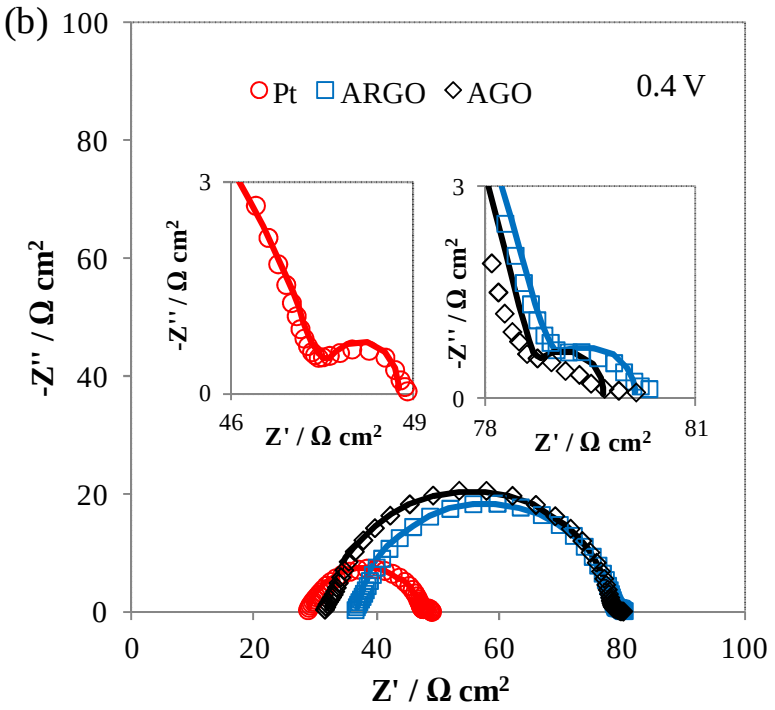

Figure 3.3 Nyquist diagrams obtained in the dark for Pt, ARGO and AGO CEs under (a) 0 V and; (b) 0.4 V bias. Represented onset Figure 3.3 (b) are the semicircles reflecting the Nernst diffusion for all tested CEs. Those right-hand side semicircles correspond to low-frequency measurements. Full symbols represent the experimental data and solid lines represent the model fitting (Figure 3.2).

Table 3.2 shows the model parameters obtained from fitting the EIS data of half-cells made of Pt, ARGO and AGO CEs, for 0 V and 0.4 V bias. Figure 3.4 shows the corresponding *I–V* curves.

Table 3.2 Model parameters for half-cells made with Pt, ARGO and AGO CEs at a bias of 0 V and 0.4 V.

		0 V			0.4 V		
CE	R_s / Ω	R_{ct} / Ω cm^2	*CPE:B* / μF cm^{-2}	*CPE:β*	R_{ct} / Ω cm^2	*CPE:B* / μF cm^{-2}	*CPE:β*
Pt	29.9	28.5	27.2	0.913	8.4	48.7	0.852
ARGO	36.3	151.1	11.5	0.933	18.6	14.4	0.916
AGO	32.7	258.5	17.6	0.923	21.7	23.3	0.893

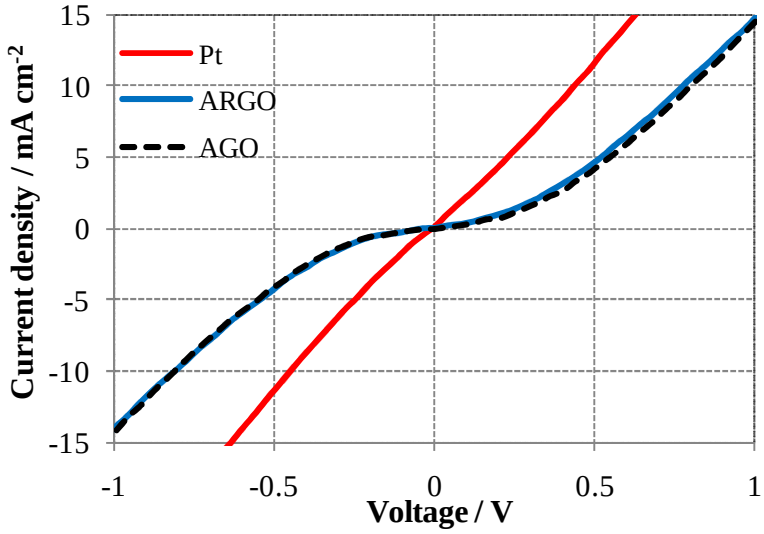

Figure 3.4 Current density–voltage measurements for half-cells assembled with Pt and graphene-based CEs.

From Table 3.2 it can be seen that for 0 V, the Pt CE's charge transfer resistance (R_{ct}) is well above the 10 Ω cm^2 threshold recommended for high performance cells [9]. However, because of the used half-cell configuration, the electrode area in contact with the electrolyte (3 cm^2) is much greater than traditionally used area (≤ 1 cm^2). As such, the total resistance of the half-cell become affected by the larger area used. Moreover, *I–V* measurements (Figure

3.4) for the Pt CE as well as for the graphene-based CEs are in accordance with previous works [21], where a methoxypropionitrile-based electrolyte was used.

The charge transfer resistance of half-cells made of non-annealed GO and RGO CEs showed to be very high, in the range of 10^6 and 10^5 Ω cm^2 respectively, at 0 V. GO films are then practically electric insulators [13] and electrons cannot successfully flow; as far as the RGO film is concerned, the high R_{ct} can be attributed to the insufficient reduction or low continuity of the film [20]. When such films are annealed under an inert atmosphere a dramatic decrease in the R_{ct} is produced, which should be related to oxygen containing functional groups removal from the basal plane of the graphene sheets. As these groups are removed, sp^2 bonds are regenerated causing a conductivity increase not only along but also between the platelets [20] . Additionally the electronic connection between the substrate and the film should also be improved. This annealing treatment allows preserving to some extent the catalytic sites, while increasing the flux of electrons traveling throughout the electrode and thus the overall catalytic activity.

Despite the increase of the catalytic activity by the graphene-based CEs from a bias of 0 to 0.4 V, they still exhibit a worse performance than the reference Pt CE – Figure 3.4 and Table 3.2. A tremendous reduction on the charge transfer resistance of the graphene electrodes can be observed from 0 V to 0.4 V bias. For both voltages, the ARGO CE displays a lower R_{ct} and capacitance than the AGO CE, probably caused by its higher conductivity [20]. Both graphene-based CEs exhibit lower capacitances than the Pt CE.

The series resistance, R_s, is only slightly higher for the graphene-based CEs when compared with Pt with the ARGO CE exhibiting the highest value. Also, the *I–V* measurements (Figure 3.4) show similar results for both AGO and ARGO CEs, indicating that the pre-reduced GO, which originated ARGO, is not needed for obtaining an efficient counter electrode, since non pre-reduced GO, which originated AGO, performs as well.

3.3.3. Dye-sensitized solar cells' I–V and EIS measurements

DSCs with the different graphene-based CEs were prepared (Figure 3.5) and their performance evaluated and critically compared with the reference Pt CE. Figure 3.6 shows the *I–V* characteristic curves for the DSCs. The corresponding photovoltaic parameters (short-circuit current density, J_{sc}; open-circuit voltage, V_{oc}; fill factor, *FF;* and efficiency, η) are summarized in Table 3.3. The EIS results presented in Figure 3.7 were obtained in dark conditions at an applied voltage of 0.7 V, which is approximately the open circuit voltage of a DSC cell.

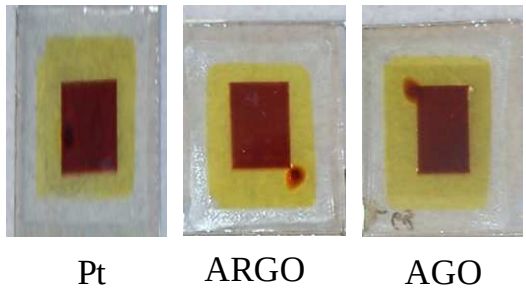

Figure 3.5 DSCs assembled with an ARGO, AGO and Pt CE.

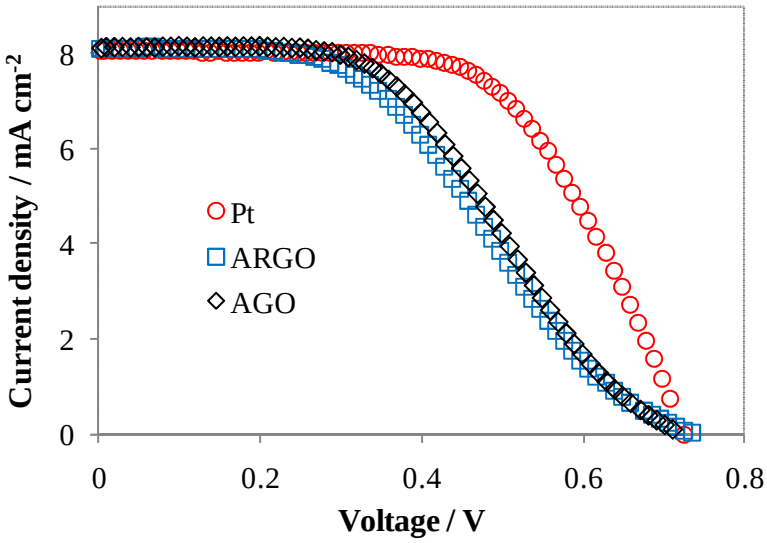

Figure 3.6 *I-V* characteristics measured at 1 sun (100 mW·m^{-2}; AM 1.5 G) of DSCs assembled with Pt, ARGO and AGO CEs.

Table 3.3 DSCs assembled with the ARGO, AGO and Pt CEs.

CE	V_{OC} / V	J_{SC} / mA cm^{-2}	*FF*	η / %	$\Delta\eta$ / %
Pt	0.74	8.03	0.61	3.50	---
ARGO	0.73	8.08	0.44	2.54	-27.5
AGO	0.72	8.11	0.46	2.64	-24.6

The DSCs with graphene-based CEs underperformed compared to the DSC equipped with the Pt CE. The results presented in Table 3.3 show that the relative difference in energy conversion efficiency, $\Delta\eta$, between the DSC made with graphene-based CEs and the Pt-DSC is ca. –25 % (–24.6 % for the AGO CE and –27.5 % for the ARGO CE). The main difference between the cells is the *FF* that for ARGO-DSC is 0.44 and for AGO-DSC is 0.46 while for Pt-DSC is 0.61, whilst J_{sc} and V_{oc} are similar. This is supported by Figure 3.7 (b) where the phase peak intensity at ~10 Hz, attributed to resistances in the semiconductor, is roughly the same for all three CEs. The left-hand side semicircle of the Nyquist diagram – Figure 3.7 (a) – corresponding to the high-frequency peak at ~1kHz – 10 kHz (see Bode diagram in Figure 3.7 (b)) reflects the catalysis and charge transfer resistance that takes place at the counter-electrode interface. For the graphene-based CEs it can be seen that for both, their high-frequency peak in the Bode diagram shifted towards a lower frequency value and correspondingly their left-hand semicircle in the Nyquist diagram enlarged, an indication of a higher charge-transfer resistance. Therefore, comparatively to the Pt CE, they have higher kinetic electron lifetimes and longer redox reaction times, thus yielding lower *FF*s [22]. The smaller *FF*s that the AGO and ARGO CE's exhibit could be attributed to an inefficient contact between the electrolyte and the catalyst layer or poor electronic connection between the graphene films and the TCO substrate.

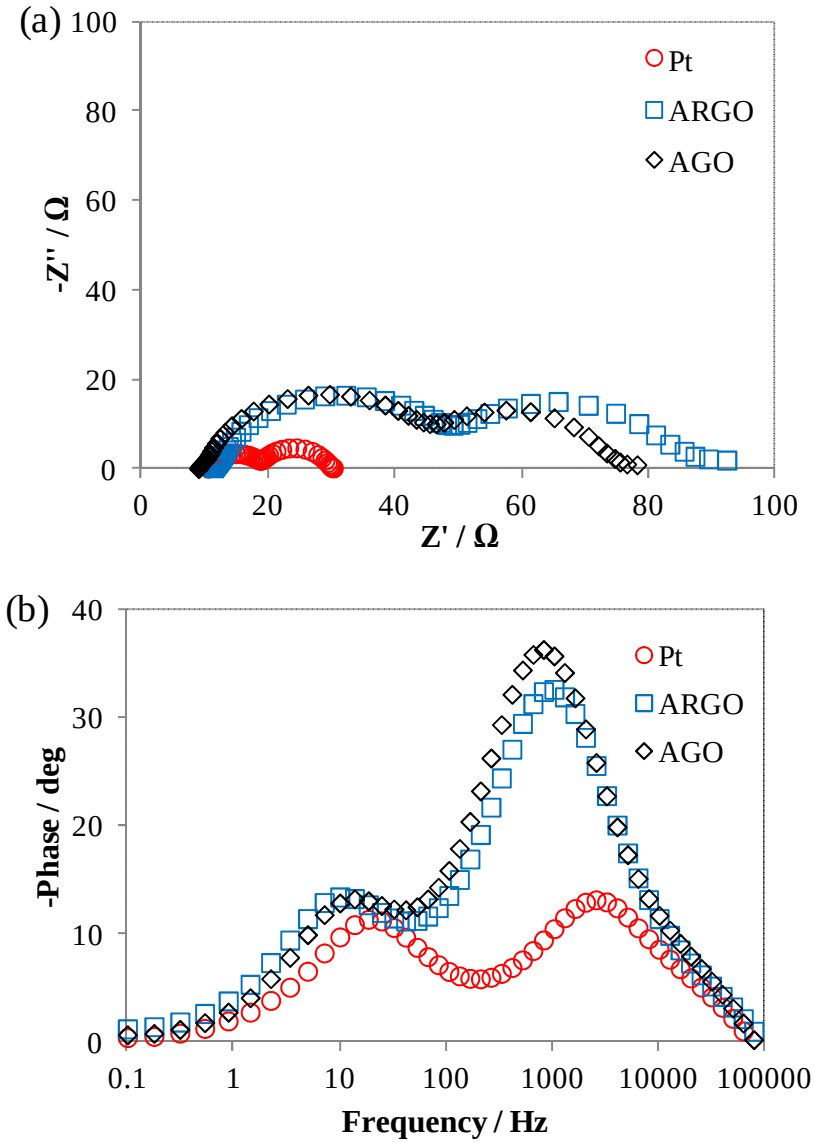

Figure 3.7 Nyquist (a) and Bode (b) diagrams obtained in the dark under 0.7 V bias for DSCs assembled with Pt, ARGO and AGO CEs.

Typically, when using impedance analysis of half-cells to access the CEs electrocatalytic activity, the evaluation is traditionally made based on the charge-transfer resistance (R_{ct}) measured at the CE/electrolyte interface. Half-cell's EIS results seemed to suggest that the ARGO CE should have yielded a

DSC with a better performance than the AGO CE (as consequence of the smaller R_{ct} and the higher current density); this can also be observed in Figure 3.7 (b) where for the DSC made with the ARGO CE its phase peak is at a higher frequency. However, the cell that originated higher efficiency was the one made with the AGO CE. The ARGO CE has a higher series resistances R_s – Figure 3.7 (b) and also as previously seen in Figure 3.3 (b) – most likely due to a higher ohmic resistance displayed by its catalytic layer, that undermines its superior catalytic ability (the lower R_{ct} and capacitance values) [23, 24]. Consequently it lowers the DSC's *FF* and its energy conversion efficiency. The assessment of the performance of graphene-based CEs using the electrochemical characterization of half-cells should therefore take in consideration all of the EIS parameters, as DSC is a very complex system. To accurately predict the CE impact on a DSC's performance, based on such electrochemical parameters, the use of DSC simulator is recommended [25].

The results that were achieved in this work compare favourably with the ones reported previously, concerning graphene-based CEs which are simultaneously transparent and efficient [21, 26, 27]. The relative efficiency of the DSC assembled with the ARGO CE is remarkably similar to a graphene CE reported by Kavan *et al.* [21]. However, ARGO CE is more transparent, $\tau_{550\ nm}$ = 94 % vs. $\tau_{550\ nm}$ = 85 % for Kavan *et al*. Furthermore, the AGO CE has marginally better efficiency and higher transparency, $\tau_{550\ nm}$ = 89 % vs. $\tau_{550\ nm}$ = 85 % for Kavan *et al*. The energy conversion efficiency obtained for the AGO CE is also comparable with results reported by Choi *et al.* [26] (2.64 % vs. 2.3 %, respectively), being also slightly more transparent, $\tau_{550\ nm}$ = 89 %, vs. $\tau_{550\ nm}$ = 85 % for Choi *et al*. Additionally, the AGO CE is based on GO deposition followed by annealing, making the CE fabrication a much simpler process.

The results that were obtained suggest that GO could be used to produce a transparent and efficient CE, averting the need to use chemically reduced GO.

However, the AGO CE should be optimised and the fabrication and morphology characteristics of the GO related to the performance of the resulted CE when inserted in a DSC.

3.4. Conclusions

Graphene-based films were prepared from graphene oxide nanoplatelets and their use as CEs in DSCs was investigated. The graphene-based CEs were produced by spray deposition of GO (AGO samples) or chemically reduced GO (ARGO samples) on FTO glass sheets, followed by thermal annealing. Conventional counter-electrodes of Pt were also prepared and used as reference.

The prepared CEs were used to make half-cells and characterized by electrochemical impedance spectroscopy. This characterization is normally performed at 0 V but, because of the special behaviour displayed by graphene, the characterization at 0.4 V was shown to be more meaningful.

The graphene oxide-based CEs were shown to have similar transparency to the Pt reference CE. Consistent with impedance data from half-cells, DSCs assembled with such graphene oxide-based CEs exhibited efficiencies of ca. 75 % compared to when using the Pt CE. Transparent ($\tau_{550\ nm}$ > 80%) and highly catalytically active CEs were obtained from spray deposition of GO nanoplatelets followed by annealing under an inert atmosphere. This novel method of producing graphene CEs preserves the activity catalytic sites while greatly increases the graphene sheets electrical conductivity. Consequently, the need of pre-reducing the graphene nanoplatelets prior to deposition is eliminated, making the CE manufacture significantly simpler. However further material and process optimization is needed to equal the performance of conventional Pt CEs.

Acknowledgments

Rui Cruz is grateful to the Portuguese Foundation for Science and Technology (FCT) and Efacec – Engenharia e Sistemas S.A. for his Ph.D grant (SFRH/BDE/33439/2008). This work was accomplished in the framework of the project WinDSC SI&IDT (ref. 21539/2011), co-financed by the European Regional Development Fund and the Portuguese Government through ADI – Agência de Inovação, under the framework of the QREN Initiative, through the Operational Programme for Competitiveness Factors. R. Cruz also acknowledges project SolarConcept (PTDC/EQU-EQU/120064/2010) for funding. Fruitful help from Dr. Arlete Apolinário is acknowledged.

References

1. O'Regan, B. and M. Grätzel, *A Low-Cost, High-Efficiency Solar-Cell Based on Dye-Sensitized Colloidal TiO_2 Films.* Nature, 1991. **353**(6346): p. 737-740.
2. Smestad, G., C. Bignozzi, and R. Argazzi, *Testing of dye sensitized TiO2 solar cells I: Experimental photocurrent output and conversion efficiencies.* Solar Energy Materials and Solar Cells, 1994. **32**(3): p. 259-272.
3. Grätzel, M., *The artificial leaf, bio-mimetic photocatalysis.* Cattech, 1999. **3**: p. 3–17.
4. Yamaguchi, T., Y. Uchida, S. Agatsuma, and H. Arakawa, *Series-connected tandem dye-sensitized solar cell for improving efficiency to more than 10%.* Solar Energy Materials and Solar Cells, 2009. **93**(6-7): p. 733-736.
5. Stankovich, S., D.A. Dikin, R.D. Piner, K.A. Kohlhaas, A. Kleinhammes, Y. Jia, Y. Wu, S.T. Nguyen, and R.S. Ruoff, *Synthesis of graphene-based nanosheets via chemical reduction of exfoliated graphite oxide.* Carbon, 2007. **45**(7): p. 1558-1565.
6. Hummers, W.S. and R.E. Offeman, *Preparation of Graphitic Oxide.* Journal of the American Chemical Society, 1958. **80**(6): p. 1339-1339.
7. Hauch, A. and A. Georg, *Diffusion in the electrolyte and charge-transfer reaction at the platinum electrode in dye-sensitized solar cells.* Electrochimica Acta, 2001. **46**(22): p. 3457-3466.
8. Roy-Mayhew, J.D., D.J. Bozym, C. Punckt, and I.A. Aksay, *Functionalized Graphene as a Catalytic Counter Electrode in Dye-Sensitized Solar Cells.* Acs Nano, 2010. **4**(10): p. 6203-6211.

9. Trancik, J.E., S.C. Barton, and J. Hone, *Transparent and catalytic carbon nanotube films.* Nano Letters, 2008. **8**(4): p. 982-987.
10. Hong, W.J., Y.X. Xu, G.W. Lu, C. Li, and G.Q. Shi, *Transparent graphene/PEDOT-PSS composite films as counter electrodes of dye-sensitized solar cells.* Electrochemistry Communications, 2008. **10**(10): p. 1555-1558.
11. Zhang, D.W., X.D. Li, S. Chen, H.B. Li, Z. Sun, X.J. Yin, and S.M. Huang. *Graphene Nanosheet Counter-Electrodes for Dye-Sensitized Solar Cells*. in *Nanoelectronics Conference (INEC), 2010 3rd International*. 2010. New York.
12. Murakami, T. and M. Grätzel, *Counter electrodes for DSC: Application of functional materials as catalysts.* Inorganica Chimica Acta, 2008. **361**(3): p. 572-580.
13. Wang, X., L.J. Zhi, and K. Mullen, *Transparent, conductive graphene electrodes for dye-sensitized solar cells.* Nano Letters, 2008. **8**(1): p. 323-327.
14. Xu, Y., H. Bai, G. Lu, C. Li, and G. Shi, *Flexible Graphene Films via the Filtration of Water-Soluble Noncovalent Functionalized Graphene Sheets.* Journal of the American Chemical Society, 2008. **130**(18): p. 5856-5857.
15. Wan, L., S. Wang, X. Wang, B. Dong, Z. Xu, X. Zhang, B. Yang, S. Peng, J. Wang, and C. Xu, *Room-temperature fabrication of graphene films on variable substrates and its use as counter electrodes for dye-sensitized solar cells.* Solid State Sciences, 2011. **13**(2): p. 468-475.
16. Geim, A.K. and K.S. Novoselov, *The rise of graphene.* Nature Materials, 2007. **6**(3): p. 183-191.

17. Rafiee, J., M.A. Rafiee, Z.-Z. Yu, and N. Koratkar, *Superhydrophobic to Superhydrophilic Wetting Control in Graphene Films.* Advanced Materials, 2010. **22**(19): p. 2151-2154.

18. Gilje, S., S. Han, M. Wang, K.L. Wang, and R.B. Kaner, *A Chemical Route to Graphene for Device Applications.* Nano Letters, 2007. **7**(11): p. 3394-3398.

19. Xu, Y.F., G.K. Long, L. Huang, Y. Huang, X.J. Wan, Y.F. Ma, and Y.S. Chen, *Polymer photovoltaic devices with transparent graphene electrodes produced by spin-casting.* Carbon, 2010. **48**(11): p. 3308-3311.

20. Wang, S.J., Y. Geng, Q. Zheng, and J.-K. Kim, *Fabrication of highly conducting and transparent graphene films.* Carbon, 2010. **48**(6): p. 1815-1823.

21. Kavan, L., J.H. Yum, and M. Grätzel, *Optically Transparent Cathode for Dye-Sensitized Solar Cells Based on Graphene Nanoplatelets.* Acs Nano, 2010. **5**(1): p. 165-172.

22. Toivola, M., L. Peltokorpi, J. Halme, and P. Lund, *Regenerative effects by temperature variations in dye-sensitized solar cells.* Solar Energy Materials and Solar Cells, 2007. **91**(18): p. 1733-1742.

23. Seo, S.H., S.Y. Kim, B.-K. Koo, S.-I. Cha, and D.Y. Lee, *Influence of electrolyte composition on the photovoltaic performance and stability of dye-sensitized solar cells with multiwalled carbon nanotube catalysts.* Langmuir, 2010. **26**(12): p. 10341-10346.

24. Aitola, K., J. Halme, N. Halonen, A. Kaskela, M. Toivola, A.G. Nasibulin, K. Kordás, G. Tóth, E.I. Kauppinen, and P.D. Lund, *Comparison of dye solar cell counter electrodes based on different carbon nanostructures.* Thin Solid Films, 2011. **519**(22): p. 8125-8134.

25. Andrade, L., J. Sousa, H.A. Ribeiro, and A. Mendes, *Phenomenological modeling of dye-sensitized solar cells under transient conditions.* Solar Energy, 2011. **85**(5): p. 781-793.

26. Choi, H., S. Hwang, H. Bae, S. Kim, H. Kim, and M. Jeon, *Electrophoretic graphene for transparent counter electrodes in dye-sensitised solar cells.* Electronics Letters, 2011. **47**: p. 281-283.

27. Huh, S.H., S.-H. Choi, and H.-M. Ju, *Thickness-dependent solar power conversion efficiencies of catalytic graphene oxide films in dye-sensitized solar cells.* Current Applied Physics, 2011. **11**(3, Supplement): p. S352-S355.

Chapter 4

Transparent Graphene/Nickel Composite Counter-electrode for Iodide/Triiodide Electrolytes in Dye-sensitized Solar Cells

Rui Cruz, Luisa Andrade, Adélio Mendes

(to be submitted, 2013)

Abstract

A novel semitransparent graphene-based counter-electrode (CE) was developed for the iodide electrolyte (I_3^-/I^- as the redox couple) used in dye-sensitized solar cells. The new CE (mGOM5/Ni) comprises oxidized commercial graphene nanoplatelets spray-deposited onto a FTO substrate decorated with electrophoretically deposited nickel particles. Ni particles seemed to restore electronic conduction on the graphene platelets during annealing under an inert atmosphere; mGOM5/Ni CE exhibited a high electrocatalytic activity, low charge-transfer resistance and high exchange current. Dye-sensitized solar cells (DSCs) assembled with the mGOM5/Ni CE yield similar efficiencies to the traditionally used electrocatalyst, platinum, with an energy conversion efficiency of 7.5 %.

Keywords: Dye-sensitized solar cell; Graphene oxide; Nickel; Composite counter-electrode; Transparent counter-electrode.

4.1. Introduction

Dye-sensitised solar cell (DSC), a photoelectrochemical device, has been regarded as a promising cheaper alternative to conventional photovoltaic systems [1, 2]. Efforts have been made to replace platinum as the catalytic material for the electrocatalysis that takes place at the counter – electrode (CE) side (cathode) of the DSC due to its scarce nature and high price [3]. To date, there is no other material capable of matching Pt electrocatalytic activity for the I_3^-/I^- redox couple (the most used and the only commercially available electrolyte system), associated with a high optical transparency of the electrode [4, 5]. Altough transparecy is not mandotaroy for a DSC, it is highly appreciated as it increases the product value by enabling its use in building integrated applications (BIPV) as well as in other tecnologies such as tandem cells [6-8]. It is therefore an important challenge to find a proper substitute for Pt as the CE material of a DSC.

Graphene has been gathering interest as a potential candidate for the replacement of traditional platinum as a counter-electrode material in a DSC. Graphene, an atomically thick sheet composed of sp^2 carbon atoms arranged in a flat honeycomb structure [9], is a material with intrinsic high surface area, high optical transmittance and good electrocatalytic properties [10-12]. Moreover, it is a relatively cheap, abundant and non-toxic material [13-16] and resistant to electrocorrosion [11]. For electrocatalysis of iodide-based electrolytes in DSCs, it is preferable to use modified versions of graphene. The necessary modifications should comprehend the inclusion in its structure of lattice defects and oxygen-functional groups attached to its sheets as these are responsible for electrocatalysis [11, 17-23]. However, a sufficient high electrical conductivity should also be maintained in order to have an efficient CE [9].

Recently, it was shown that the thermal reduction of exfoliated graphene oxide could yield somewhat promisingly efficient CEs for the I_3^-/I^- redox

reaction, while having high transparency (transmittance higher than 80 % at 550 nm) [24]. The presented procedure enabled averting the need to pre-reduce oxidized and defected graphene nanoplatelets prior to film deposition, thus reducing the manufacturing complexity. Nevertheless, there was a shortcoming of efficiency due to high charge-transfer resistances mainly caused by poor electronic connection between the platelets or between the catalytic film and the substrate, which is translated into low fill factors. To overcome this problem, a new approach was devised. Maintaining the same deposition method and thermal reduction methods, oxidized graphene nanoplatelets were deposited on top of glass covered-fluor-doped tin oxide (FTO) substrate decorated with electrophoretically deposited nickel particles. Developed graphene/Ni-based CE was observed to equal and even surpass the electrocatalytic activity for the I_3^-/I^- redox couple shown by the traditional Pt CE under comparable conditions. Additionally, as the composite graphene/Ni-based CE exhibited a fairly high transparency (transmittance at 550 nm above 80 %), it is believed that it may be the front-runner candidate for the replacement of Pt counter-electrode material for DSCs in iodide electrolyte systems.

4.2. Material and Methods

4.2.1. Preparation of modified (oxidized) graphene from commercial graphene nanoplatelets – mGOM5

The production of oxidised graphene was carried out using the modified Hummer's method [25, 26]. The source material was commercial graphene nanoplatelets - Grade M5, from XG Sciences – hereinafter denominated as GnPM5. Graphene was added to a solution of H_2SO_4 at room temperature; the solution was cooled at 0 °C using an ice bath and then $KMnO_4$ was gradually added (3 wt% relatively to graphene). The mixture was heated at 35 °C and stirred for 2 h. After that, water was added into the mixture at 0 °C (ice bath).

Then H_2O_2 (30 %) was added until no gas is produced. After resting overnight, the resultant dispersion was decanted and the solid recovered. It was then centrifuged multiple times at 4000 rpm, during 15 minutes using distilled water, until pH > 4. The final resulting dispersion was decanted and the resulting solid material freeze-dried for 48 h. The resulting material was exfoliated in water, for 4 h in a basic pH (ca. 9), with the help of NH_3, 6 M, using an ultrasonic bath. After, part of this colloid was centrifuged twice at 5000 rpm for 30 min to remove aggregates and larger sheets and the supernatant was recovered and freeze-dried for 48 h. This material is referred hereinafter as mGOM5.

For assembling all CEs, conductive fluorine-doped tin oxide (FTO) coated glass substrates (2 mm-thick, 2.5 cm × 2.5 cm, sheet resistance 15 $\Omega \cdot square^{-1}$, Dyesol) were used. Prior to use, FTO-coated glass substrates were washed in an ultrasonic bath with detergent (Alconox, VWR) for 60 min and then ethanol for 45 min.

4.2.2. Nickel electrophoretic deposition

Pre-treated FTO substrates were immersed in a nickel solution comprised of 1.14 M $NiSO_4 \cdot 6H_2O$, 0.19 M $NiCl_2 \cdot 6H_2O$ and 0.73 M H_3BO_3 (pH ~ 4.5), at a temperature of 30 ºC. The electrophoretic deposition of nickel was performed at a constant potential of -1 V, using a reference electrode of Ag/AgCl (in 4 M KCl) and a platinum wire mesh as the CE. The deposition time was optimized to 5 seconds (for a Ni^{2+} electrical charge of ca. 0.02 C). The resulting substrates are referred hereinafter as FTO/Ni.

4.2.3. Gold sputtering deposition

Gold particles were deposited onto pre-treated FTO substrates by sputtering; base pressure of $\sim 5 \times 10^{-2}$ bar, working pressure of $\sim 2.5 \times 10^{-1}$ bar, sputter current of 20 mA. Sputtering was carried out for a period of 2 - 5 seconds so that the amount of Au particles deposited was similar to the amount of Ni deposited by electrophoresis (nickel ca 4.5 x 10-8 mol cm^{-2} and gold ca 8.0 x 10-7 mol cm^{-2}).

4.2.4. Counter-electrode and half-cell (symmetric dummy cell) fabrication

The Pt CE was prepared by depositing a Pt paste (Pt-Catalyst T / SP, Solaronix) onto the entire surface of the pre-treated conductive glass using doctor-blade technique, followed by heat treatment at 400 °C for 15 min. Graphene-based CEs were prepared by spray deposition, using a Revell 39101 airbrush, with the aid of a compressed flow of reconstituted air. Distance between the substrate and the spray nozzle was approximately 10 cm.

It was prepared aqueous colloids of mGOM5 with an approximate concentration of 0.1 mg catalytic material per gram of suspension. These suspensions exhibited a negligible sedimentation. The suspensions were sprayed onto the FTO or FTO/Ni glass substrates placed on a pre-heated hot-plate at *ca.* 120 ºC. The films were then annealed for 15 min at 550 ºC under an inert atmosphere and then slowly cooled (< 10 ºC s^{-1}). The mGOM5 loads that were applied to each electrode (ca. 5 – 15 µg·cm-2) were such that their transmittance value at a wavelength of 550 nm was above 80 %.

A half-cell configuration, consisting of two identical FTO-coated glass substrates coated with the catalytic materials [27], was used for the electrochemical impedance spectroscopy (EIS) study. The half-cell was sealed with a 25-µm thick Surlyn frame (Solaronix) at 100 ºC for 10 s. After sealing, the cells were filled with an iodide based electrolyte solution (organic iodide salt, 10 - 30 wt%, alkyl pyridine 10 wt%, iodine 10 wt%, inorganic iodide salt 10 wt%, guanidine thiocyanate 10 wt% in acetonitrile 60 wt% and valeronitrile 10 – 30 wt%, EL-HPE, Dyesol) through a pre-drilled 1 mm diameter hole. These holes were then sealed using a melted Surlyn disc and a thin glass lamella. The active area, *i.e.* the area of the electrode in contact with the electrolyte, was 2 cm^2. Half-cells were assembled in duplicate for each catalytic material and reproducibility assessed.

4.2.5. Dye-sensitized solar cell fabrication

DSCs with an active area of 0.4 cm^2 were fabricated according to the following procedure: FTO-coated glass substrates (2 mm-thick, 2.5 cm × 1.8 cm) were washed in an ultrasonic bath first with detergent (Alconox, VWR) and then with ethanol. A 4-6 μm-thick transparent film of TiO_2 (20-nm sized TiO_2 particles, T/SP - Solaronix) was printed on the FTO glass electrode by the doctor blade technique (photoanode). The deposited paste was sintered in air at 450 °C for 30 min. After cooling to 70 °C, the TiO_2 electrode was sensitized by immersing it in a N719 dye solution (0.3 mM in ethanol, Solaronix) at room temperature for more than 12 h. Afterwards the dye-sensitized electrode was rinsed with ethanol and dried in moisture-free environment. Pt and graphene-based CEs were prepared as described above (in section 4.2.4). Each specimen was prepared in duplicate. The photoanode and the counter-electrode were sealed with a 25-μm thick Surlyn frame at 100 °C for 10 s. After sealing, the cells were filled with an electrolyte solution (iodide based, EL-HPE, Dyesol) through a pre-drilled 1 mm diameter hole done in the counter-electrode side. The hole was sealed using a melted Surlyn disc and a thin glass lamella. Reproducibility was achieved for all DSCs.

To further access the potential of the described graphene-based CEs, more efficient cells were assembled. The assembling procedure was very similar to the aforementioned, with the exception of the photoanode. The photoanode was modified to have a thickness of ~ 10 μm of 20-nm sized TiO_2 particles and ~ 4 μm of 400-nm sized TiO_2 particles and it was immersed in a N719 dye solution (1 mM in ethanol, Solaronix) at room temperature for more than 12 h.

4.2.6. Structural properties characterisation

Differential thermal (DTA/TG) and thermogravimetric analysis (TGA), (SETARAM Labsys 1600 DTA/TG-DSC) were used to access the structural behaviour of the different materials. They were characterized under an oxygen

atmosphere. It was used an input flow rate of 30 mL min^{-1} and a heating ramp of 3 ºC min^{-1} up to 850 ºC. Particle size and particle size distribution (PSD) of the graphene materials were determined using a Coulter Counter equipment (Coulter LS Particle Size Analyser 230). The morphology of the graphene films placed on top of FTO and FTO/Ni substrates was accessed through Scanning Electron Microscopy (SEM), equipped with Energy Dispersive Spectroscopy (SEM-EDS, Hitachi SU-70 with Bruker EDS detector). Raman imaging and spectroscopy (LabRAM HR Evolution, Horiba Scientific, excitation laser energy 2.33 eV/ 532 nm) was also performed on the aforementioned films. The surface roughness of the films was evaluated using atomic force microscopy (AFM, Digital Instruments). Transmittance measurements of the different CEs were carried out using an UV/VIS/NIR spectrophotometer (Lambda 750, Perkin Elmer). Graphene and Pt films were deposited on bare and FTO-coated glass substrates. Measurements were taken from the coated side.

4.2.7. Half-cell and dye-sensitized solar cell characterization

The half-cells (HCs) were characterized by electrochemical impedance spectroscopy (EIS). EIS experiments were carried out with a ZENNIUM workstation (Ref. 2425-C, Zahner Elektrik, Germany). The frequency range was 100 mHz-100 kHz and the magnitude of the modulation signal was 10 mV. All the measurements were performed at room temperature in the dark at 0 V. ZView software (Scribner Associates Inc.) was used to process the EIS data. Current density–voltage (*I-V*) and Tafel-polarization measurements were also carried out in the dark with a scan rate of 100 mV s^{-1}, ranging from – 1 V to 1 V.

Density-voltage (*I-V*) characteristics and EIS spectra were obtained for each prepared DSC. A 150 W xenon light source (Oriel class A solar simulator, Newport USA) irradiating 100 mW cm^{-2} (1 sun light-intensity) at the surface of the DSC and equipped with an air mass filter of 1.5 (Newport, USA) was used for obtaining the *I-V* characterization. The simulator was calibrated using a

single crystal Si photodiode (Newport, USA). The *I-V* characteristics were obtained applying an external potential bias and measuring the generated photocurrent. The photovoltaic parameters (short-circuit current density, J_{sc}; open-circuit voltage, V_{oc}; fill factor, *FF*) were extracted from the *I-V* curve and used to calculate the efficiency, η:

$$\eta = \frac{V_{OC} J_{SC} FF}{I_S} x100 \tag{4.1}$$

where I_S is the intensity of the incident light. The relative difference in energy conversion efficiency, $\Delta\eta$, between the DSC prepared with a graphene-based CE and the Pt-based DSC was calculated according to the following equation:

$$\Delta\eta = \frac{\eta_{grapheneCE} - \eta_{Pt}}{\eta_{Pt}} x100 \tag{4.2}$$

EIS characterization was accomplished using a ZENNIUM workstation (Ref. 2425-C, Zahner Elektrik, Germany). These measurements were performed at room temperature at 0.7 V (close to typical open-circuit voltages), under dark conditions. ZView software (Scribner Associates Inc.) was used to process the EIS data.

4.3. Results and discussion

4.3.1. Composite CE characterization

Modified (oxidized) graphene platelets used as a catalytic film in a dye-sensitized solar cell were characterized. Hummers' method was used to accomplish the graphene oxidation due to its simplicity. This was performed in order to introduce the needed oxygen moieties and defects for catalysis. The relevance of the type of graphene oxide used became clear when analyzing their corresponding SEM images - Figure 4.1. It can be seen that graphene oxide produced from graphite [24] is randomly organized, aggregating in bundles,

contrary to a very planar shape displayed by the oxidized graphene nanoplatelets. This difference becomes significant when trying to form a film using such structures. The oxidized graphene nanoplatelets cover the FTO surface much evenly, better fitting to its rough surface and thus facilitating the establishment of electrical contact points. From SEM analysis it was also accessed that each nanoplatelet was ~ 8 nm in thickness - Figure 4.1 (b).

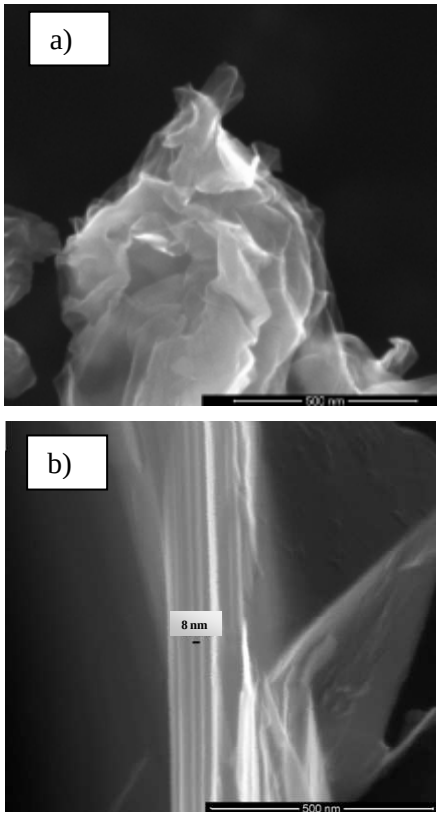

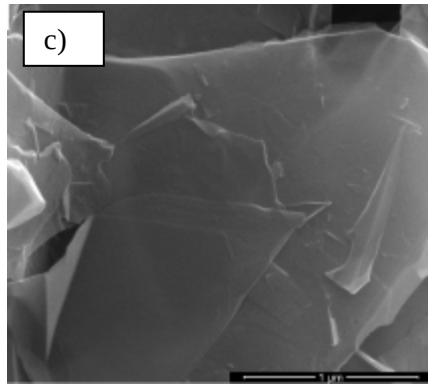

Figure 4.1 SEM images of graphene oxide produced from: a) graphite; and from b)-c) commercial graphene nanoplatelets, after exfoliation and drying.

Atomic force microscopy (AFM) and SEM images in Figure 4.2 depict films of oxidized graphene nanoplatelets (mGOM5) that were deposited on top of the FTO surface before and after being thermal annealed. Before annealing the mGOM5 film appears to be only on top of the FTO surface. On the other hand, after annealing the film seems to sink into the typical "mountain-crests" shapes of the FTO, moulding its structure to that landscape - Figure 4.2 (c). Such perception was validated by surface roughness measurements. The roughness of the surface was measured to be R_a ~ 13.5 nm for the FTO surface, R_a ~ 9.7 nm for the non-annealed mGOM5-5kup film and R_a ~ 13.4 nm for the annealed one.

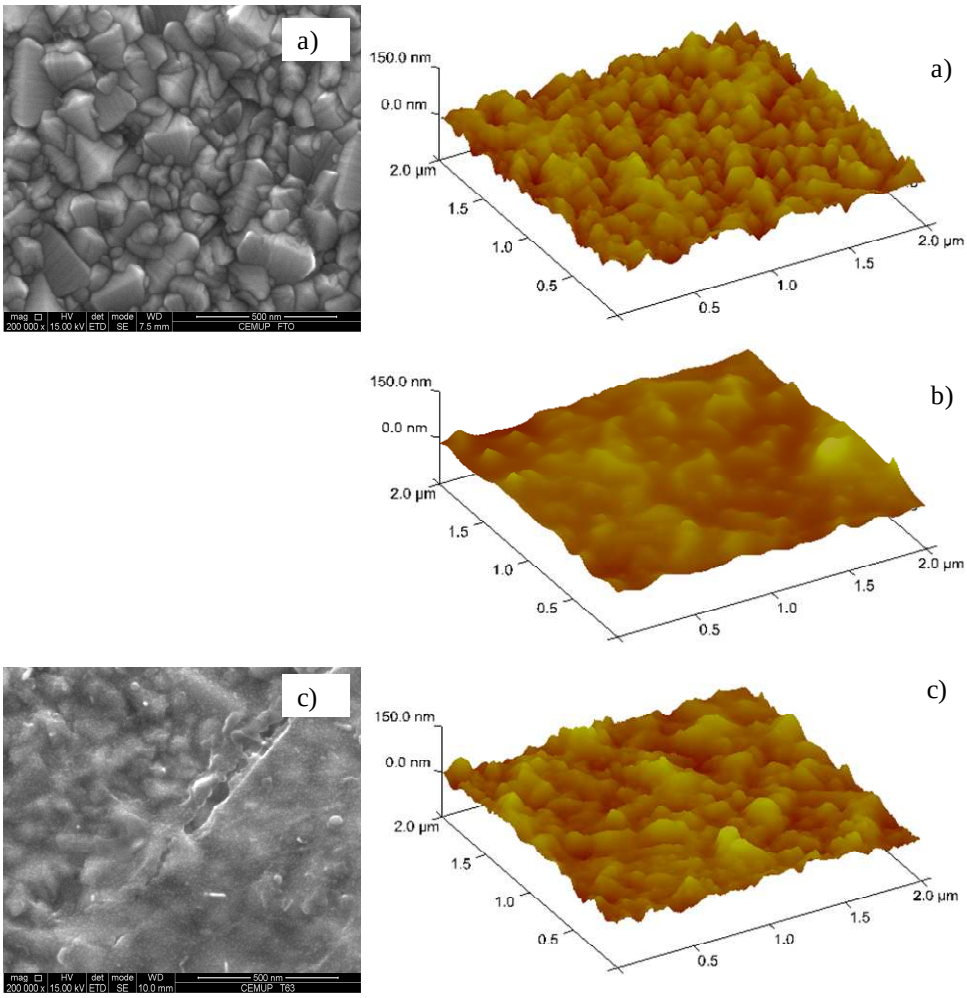

Figure 4.2 AFM and SEM images of the FTO surface – a), a film of oxidized graphene nanoplatelets (mGOM5) deposited on top of the FTO surface prior to thermal annealing – b) and after annealing – c). Notice the "sinking" effect of the graphene platelets after being thermally annealed.

Differential thermal (DTA/TG) and thermogravimetric analysis (TGA) techniques were carried out to access the structure of the oxidized graphene platelets (mGOM5) and pristine commercial graphene nanoplatelets (GnPM5). Figure 4.3 shows the exothermic heat flow and weight loss as a function of the burning temperature for both aforementioned materials. Table 4.1 summarises the quantification of the different structures present on both materials and the

corresponding degradation temperatures. The initial weight loss was due to absorbed water. The weight loss observed below 450 ºC reflects the presence of oxygen-containing functional groups on both materials [25, 28-30]. The weight loss at ~ 620 ºC for GnPM5 (83.6 %) and at ~ 490 ºC for mGOM5 (17.1 %) can be attributed to combustion of the graphene lattice. This shows that, due to the oxidation process, mGOM5 became less stable than its source material as the burning temperature of corresponding graphene structure (sp^2 bonds) is higher and the amount of the graphene bonds is lower. The overall oxygen-containing functional groups present in mGOM5 increased to 71.4 %. For mGOM5, the lower degradation temperatures (167 ºC and 227 ºC) should correspond to the removal of –OH and –COOH groups, thus appearing that the oxidation process has introduced a large number of epoxy moieties (~ 48%) [29].

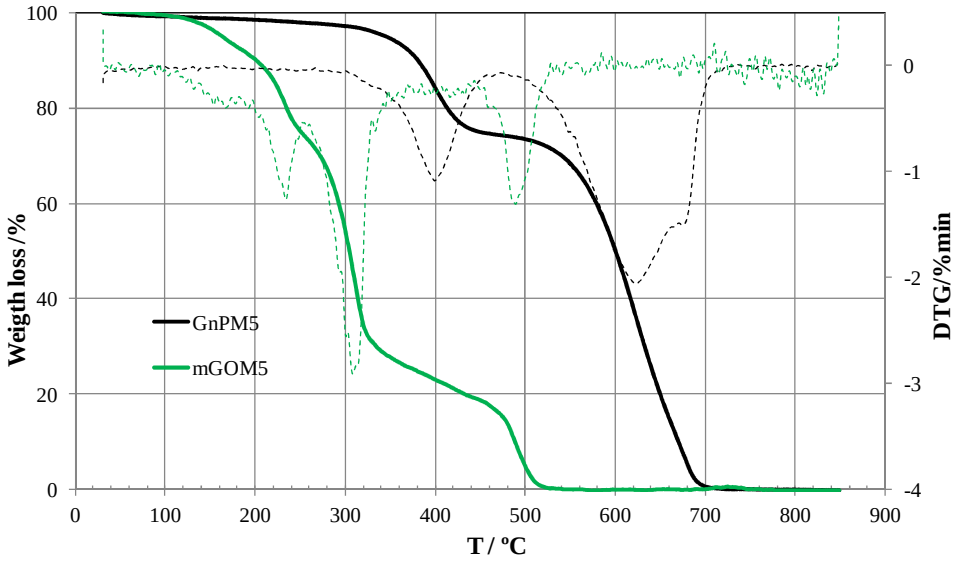

Figure 4.3 Differential thermal (DTA/TG) and thermogravimetric analysis (TGA) of the commercial graphene nanoplatelets (GnPM5) and their oxidized form (mGOM5).

Table 4.1 Quantification of weight loss and corresponding degradation temperatures suffered by GnPM5 and mGOM5 during the thermogravimetric and differential thermal analysis.

Sample	**GnPM5**		**mGOM5**	
	***T* / ºC**	***Weigh loss* / %**	***T* / ºC**	***Weigh loss* / %**
H_2O	--	3.0	--	0.9
C-O groups	--	--	166.7	8.1
	--	--	234.2	15.3
	399.2	13.4	308.4	47.9
Graphene	623.4	83.6	489.2	17.1

Particle size was also accessed for GnPM5 and mGOM5 using a Counter Coulter instrument - Figure 4.4. GnPM5 particles had a particle size of ~20 µm. The oxidation process appeared to have created two broad particle sizes, around 0.6 and 2 µm. Nonetheless, particle size of the modified graphene (mGOM5) is much smaller than the source material.

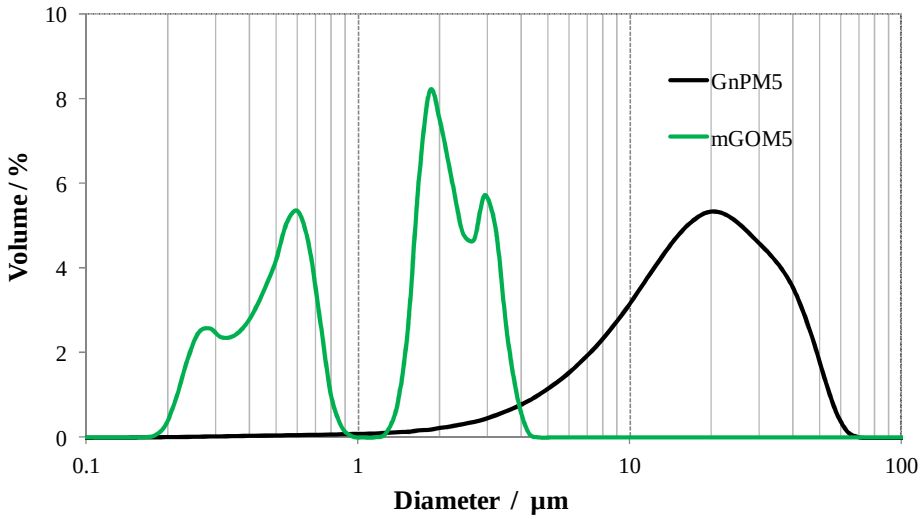

Figure 4.4 Particle size distribution for GnPM5 and mGOM5.

The newly developed CE composite of modified (oxidized) commercial graphene platelets/nickel was prepared in two steps. First, a little amount of very small nickel particles (FTO/Ni) were deposited onto FTO-covered glass by electrophoretic deposition (EDP) - Figure 4.5 b). This deposition technique is widely used in industry since it has the advantage of being an automated and high throughput process [31, 32]. In the second step, an aqueous colloid of oxidized commercial graphene nanoplatelets, mGOM5, was sprayed onto the FTO/Ni substrate with a very small load (~5 – 15 $\mu g \cdot cm^{-2}$). The mGOM5 load used in the different depositions was more accurately assessed by measuring its transmittance value at a wavelength of 550 nm, τ_{550nm}. Depositions were carried out such that the mGOM5 films had τ_{550nm} above 80 %. Afterwards, this composite CE was annealed under an inert atmosphere. The morphology of the composite CE fabricated with mGOM5 and the FTO/Ni substrate, hereafter coded as mGOM5/Ni, is shown in Figure 4.5.

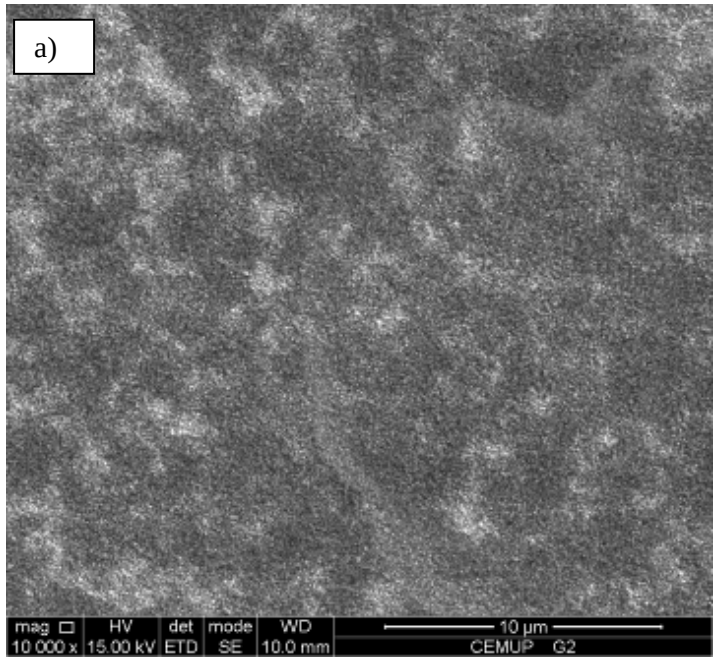

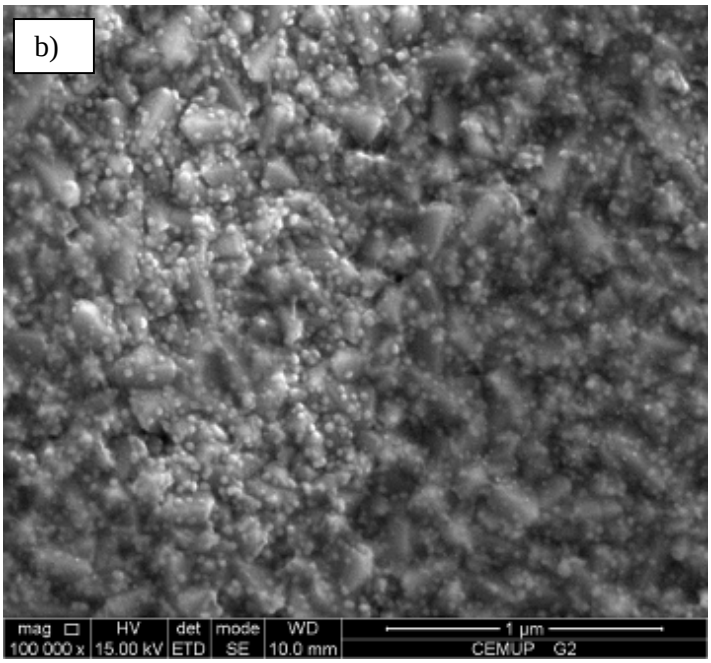

Figure 4.5 SEM images of the mGOM5/Ni CE after being thermally annealed. In b) it can be seen that the graphene sheet is so transparent that the nickel particles underneath are still clearly perceived.

From Figure 4.5 it can be seen that the film created by spray deposited of mGOM5 did not covered complety the FTO/Ni substrate leaving some Ni particles exposed. Energy Dispersive Spectroscopy (EDS) scanning perfomed on the darker areas signaled the presence of carbon. The graphene sheet is so transparent that the nickel particles underneath are still clearly perceived - Figure 4.5 (b). Although some Ni particles are exposed to the electrolyte, neither corrosion nor leaching of Ni should occur [33, 34].

Raman spectroscopy was performed in order to monitor the effect of the nickel particles on the structure of the mGOM5 films during the annealing stage. “Damaged” graphene materials (in which are included oxidized forms) display two prominent bands on their Raman spectra [35-39]: a D band at a wavenumber of ca. 1356 cm^{-1} and a G band at a wavenumber of ca. 1582 cm^{-1} (for an excitation laser energy of 2.33 eV). The D band corresponds to a double resonance Raman scattering near the K point of the Brillouin zone and is an

indication of the presence of defects in the structure. The G band corresponds to a doubly degenerate in-plane optical vibration (E_{2g}) and is a representation of the sp^2 hybridized bonds common to all sp^2 nanocarbons (graphene, nanotubes, nanohorns, highly oriented pyrolitic graphite) [35-39]. The intensity ratio of the D band (I_D) to the G band (I_G), I_D/I_G, is often used as an indication of the number and size of sp^2 domains and the quantity of defects present in the structure of graphite-based materials [35-41]. In Table 4.2 are represented the intensity ratio of I_D/I_G of several graphene-based films. Measurements were also performed on equivalent CEs that did not suffer annealing (referred to as "25ºC").

Table 4.2 Intensity ratio of D and G bands for the graphene-based materials.

CE	I_D/I_G
mGOM5, 25ºC	1.153
mGOM5	1.070
mGOM5/Ni, 25ºC	1.181
mGOM5/Ni	0.954

The intensity ratio I_D/I_G for mGOM5 and mGOM5/Ni CEs at 25 ºC was found to be very similar (ca. 1.2). When they were subjected to annealing under an inert atmosphere both CEs suffered a reduction of I_D/I_G, indicating that double bonds had been restored probably due to the elimination of oxygen-containing functional groups [21, 41, 42]. Interestingly, for the electrode with the Ni particles - mGOM5/Ni, a further decrease of I_D/I_G is observed relative to the mGOM5 CE (0.945 vs 1.070, respectively). This may imply that the Ni particles were responsible for further restoration of the sp^2 domains either trough elimination of more oxygen functional groups or restoration of structural defects on the bottom surface of the graphene platelets.

4.3.2. Analysis of half-cells

The electrocataltyc activity of the CEs can be accessed from half-cells (or symmetric dummy cells). A hall-cell consists of two identical FTO-coated glass substrates coated with the catalytic materials, [27] mimicking the phenomena in a DSC, but allowing to evaluate the CE catalytic activity without interference of the photoanode. All catalytic films tested (Pt and mGOM5-based CEs) had τ_{550nm} above 80 % (95 % for Pt, 87% for mGOM5 and 86 % for mGOM5/Ni).

The quantification of the electrocatalytic activity of the CEs was carried out by electrochemical impedance spectroscopy (EIS) analysis on the half-cells. Measurements were taken at room temperature, in the dark, at a bias voltage of 0 V. The electrocatalytic activity towards the I_3^-/I^- redox couple was studied using an acetonitrile-base medium electrolyte. The EIS spectra of the prepared half-cell were fitted to the electrical analogue shown in Figure 4.6, based on the Randles-type circuit, where R_s is the series resistance, including the sheet resistance of the TCO and the resistance of the contacts; R_{ct} is the charge transfer resistance of the CE; C is the capacitance of the electrical double layer; and Z_N is the Nernst diffusion impedance in the bulk electrolyte. Due to non-idealities, the capacitance was replaced by a constant phase element, *CPE* [27].

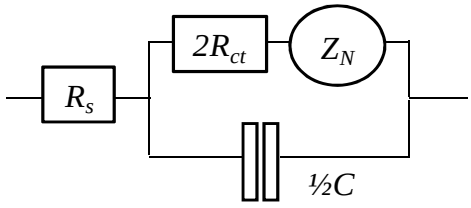

Figure 4.6 Electrical analogue used for fitting the electrochemical impedance spectra data of half-cells.

The fitting of the EIS experimental data was accomplished with ZView® software (Scribner Associates Inc.). The R_{ct} parameter is particularly relevant for the evaluation of a CE. R_{ct} is directly related to the ability of the material to

catalyse the reduction of I_3^- at the CE/electrolyte interface. R_{ct} is also related to the exchange current density through the equation [43]:

$$j_0 = \frac{RT}{nFR_{ct}} \tag{4.3}$$

where R is the gas constant, T is the temperature, F is the Faraday constant and n is the stoichiometric number of electrons involved in a reaction. Since an efficient CE should have a j_o similar to the photocurrent density of the DSC photoanode, the R_{ct} value should be as low as possible in order to reduce the electrolyte as quickly as possible [43-46]. Regarding the capacitance of the CE, as it represents the accumulation of charge, it should be also as low as possible [47]. Additionally, *I-V* and Tafel-polarization measurements were carried out in order to observe the behaviour of the CEs at different voltages.

Figure 4.7 shows the Nyquist diagrams of CEs of the half-cells at 0 V. Left-hand side semicircles correspond to high-frequency measurements (more than 10 Hz) and reflect the charge-transfer resistance and double layer capacitance of the CE, while right-hand side semicircles result from low-frequency measurements (less than 10 Hz) associated with the Nernst diffusion impedance.[4, 11] Table 4.3 shows the model parameters obtained from fitting the EIS data of the half-cells made of Pt, mGOM5 and mGOM5/Ni CEs, for 0 V. Figure 4.8 and Figure 4.9 show the corresponding *I–V* and Tafel-polarization curves.

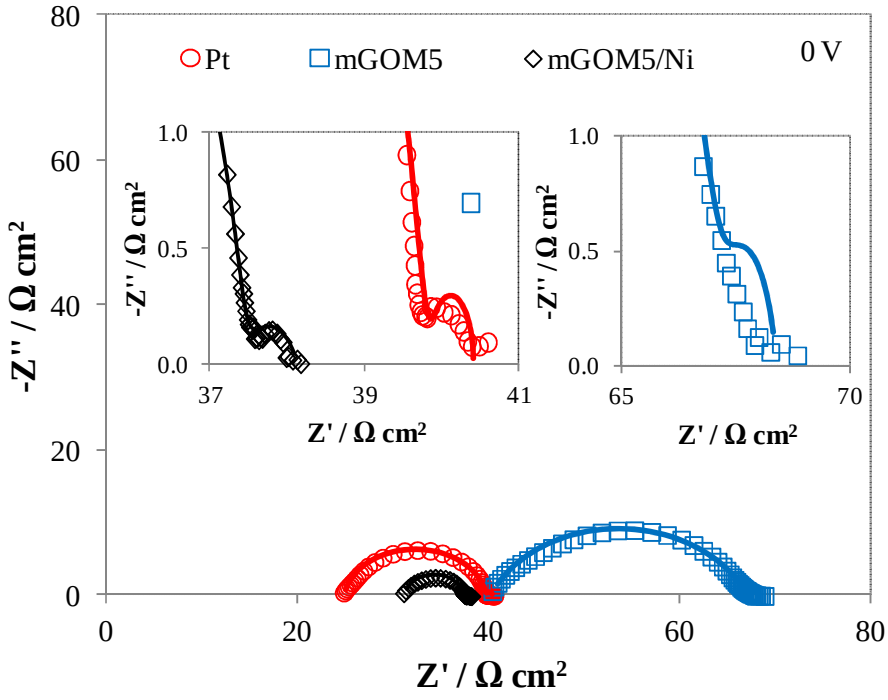

Figure 4.7 Nyquist diagrams obtained in the dark for half-cells with Pt, mGOM5 and mGOM5/Ni CEs under 0 V from 100 mHz to 100 kHz. In the insets are the semicircles reflecting the Nernst diffusion for all tested CEs at low-frequencies. Full symbols represent the experimental data and solid lines represent the model fitting.

Table 4.3 Model parameters for half-cells made of Pt, mGOM5 and mGOM5/Ni CEs at a bias of 0 V in the dark.

CE	$\tau_{550\ nm}$ / %	R_s / Ω	R_s / Ω cm^2	R_{ct} / Ω cm^2	*CPE:B* / μF cm^{-2}	*CPE:β*	C_{CE} / μF cm^{-2}	$R_{ct}C_{CE}$ / *ms*
Pt	95	12.9	25.1	7.3	16.9	0.903	6.45	0.047
mGOM5	87	19.8	40.2	13.4	48.7	0.755	4.50	0.060
mGOM5/Ni	86	15.0	31.3	3.0	9.2	0.923	4.02	0.012

When comparing the mGOM5 CE with mGOM5/Ni CE it can be seen that the inclusion of Ni particles in the FTO substrate had a profound effect in the electrocatalytic activity of the mGOM5 film - Table 4.3 and Figure 4.7. A reduction of the series resistance, R_s, was observed (from 40.2 Ω cm^2 to 31.3 Ω cm^2), although it is still higher than that of the reference Pt CE (25.1 Ω cm^2). The most notorious difference was achieved in the charge transfer resistance of the mGOM5/Ni CE (3.0 Ω cm^2), which greatly dropped below the value of R_{ct} of the Pt CE (7.3 Ω cm^2). Both CEs had R_{ct} values below 10 Ω cm^2, the threshold recommended for high performance cells [27]. The mGOM5/Ni CE also displays a lower capacitance than the Pt CE (9.2 µF cm^{-2} vs. 16.9 µF cm^{-2}, respectively). This means that less charge is accumulated at the mGOM5/Ni CE/electrolyte interface during the reduction of I_3^- ions, presumably due to its better catalytic nature. Considering that the graphene-based CEs had roughly the same thickness (because they had similar transmittances) and therefore the same available surface area for catalysis, the fact that the mGOM5 CE showed a high capacitance and high R_{ct} seems to indicate that Ni particles might play a role for the increased electrocatalytic activity. When graphene films are annealed in an inert atmosphere, partial restitution of the electronic conjugation takes place because of the elimination of oxygen functional groups due to thermal-induced decomposition; additionally the graphene sheets become more ordered [21, 41, 42] and the films smoother. As a result, the mGOM5 platelets would have "sunk" into the FTO during the thermal annealing as previously shown - Figure 4.2. The mGOM5 platelets deposited on top of the FTO/Ni would then have been in close contact with the Ni particles during the thermal annealing. It is well known that graphene can be synthesized from Ni foils through thermal chemical vapour deposition (CVD) [48, 49]. Although higher temperatures are used in CVD processes than the ones used here in the annealing step, nucleation (heteroepitaxial growth of graphene on Ni [48]) might have taken place in a minor extension but sufficient to restore some sp^2 domains disrupted during

oxidation. This would allow electrons to be injected much quicker into the electrolyte and reduce the I_3^- ions. The number of new restored sp^2 connections coupled with a sufficient number of catalytic sites that still remained after annealing were instrumental to yield a mGOM5 CE with such a low electrocatalytic activity (low R_{ct}). As well as further restoring the electronic conductivity between and along the mGOM5 platelets, the Ni particles connected to the graphene platelets would allow for a lower electronic resistance in the FTO/Ni/mGOM5 interface (lowering the R_s).

For better quantitative comparison of such thin films, the product $R_{ct}C_{CE}$ was used as a figure of merit for their catalytic activity. For that it was assumed that the area-specific capacitance of the CEs only depends on the capacitance of the Helmholtz double layer per microscopic surface area, which is similar in carbon materials of metallic nature.[44]. As the capacitance had been previously replaced by a constant phase element for fitting the Nyquist curves, it was necessary to calculate the overall capacitance, C_{CE} [50] (with R_{ct} having units of Ω cm^2 and *CPE:B* having units of F cm^{-2}):

$$C_{CE} = \frac{\left(R_{ct} CPE:B\right)^{\frac{1}{CPE:\beta}}}{R_{ct}} \tag{4.4}$$

The results in Table 4.3 show that the mGOM5/Ni CE has a $R_{ct}C_{CE}$ of 0.012 ms, much lower than the one obtained for the Pt CE – 0.047 ms. The mGOM5 CE exhibit the worst $R_{ct}C_{CE}$ value (0.06 ms). These results further confirm the higher catalytic activity yield by the mGOM5/Ni CE.

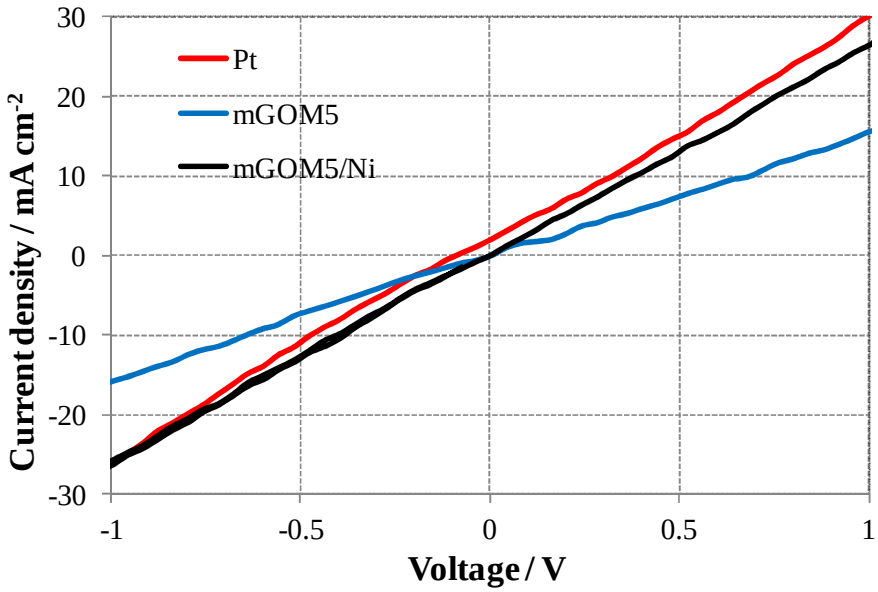

Figure 4.8 Current density–voltage measurements for half-cells assembled with Pt and mGOM5-based CEs.

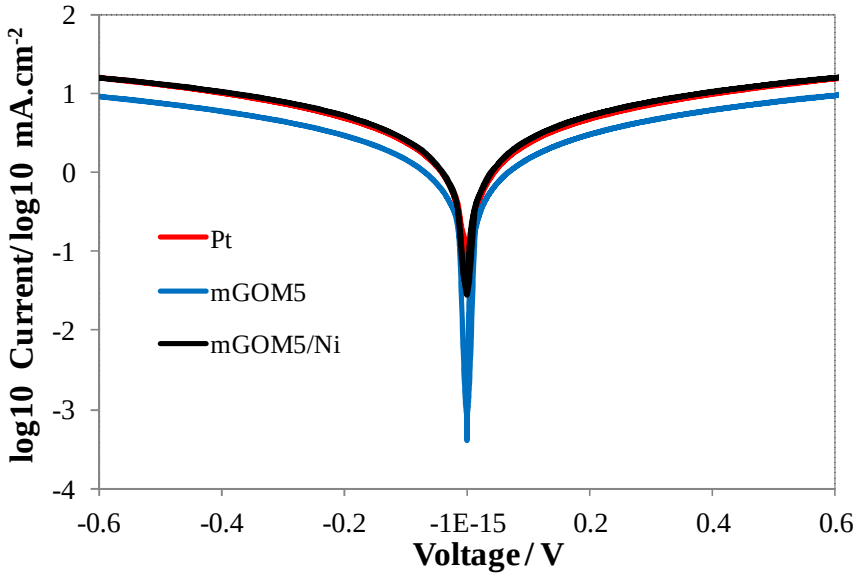

Figure 4.9 Tafel-polarization measurements for half-cells assembled with Pt and mGOM5-based CEs.

I-V measurements on half-cells (Figure 4.8) show that the Pt and mGOM5/Ni CEs had similar slopes and behaviours as voltage increased, indicating a similar catalytic behaviour. The mGOM5 CE yielded a curve with a lower slope demonstrating worse electrocatalytic behaviour.

Information regarding the exchange current density can be extracted from the higher potentials on the Tafel-polarization curves - Figure 4.9 [51, 52]. Both Pt and mGOM5/Ni CEs showed similar slopes at those potentials (> |0.4 V|), thus indicating similar j_o and therefore high electrocatalytic activity, and steeper than the mGOM5 CE. These results are consistent with the EIS and *I–V* results of the half-cells. The results obtained from the analysis of half-cells indicate that the mGOM5/Ni CE has the ability to match or even outperform the Pt CE regarding the catalysis of I_3^-/I^- redox couple, although being slightly less transparent.

4.3.3. Analysis of dye-sensitized solar cells

Complete DSCs were assembled with the different graphene-based counter-electrodes and then compared with the typical behaviour of the Pt CE - Figure 4.10.

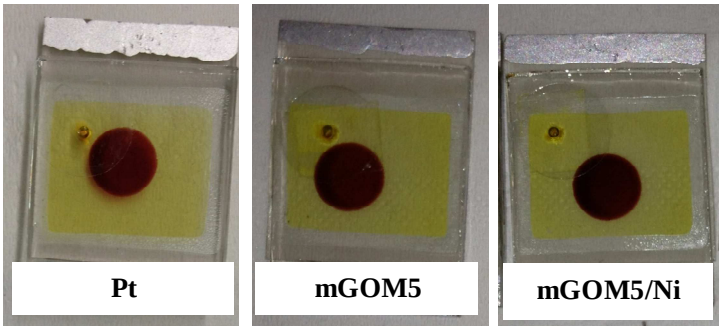

Figure 4.10 DSCs assembled with a mGOM5, mGOM5/Ni and Pt CEs.

The mGOM5/Ni CE was less transparent than the Pt CE ($\tau_{550\ nm}$ = 80.6 % vs. 92.0 %) and slightly less transparent than the mGOM5/Ni CE used in the half-cell configuration ($\tau_{550\ nm}$ = 80.6 % vs. 86 %) – section 4.3.2. Figure 4.11 shows the *I*–*V* characteristic curves for these DSCs and their corresponding photovoltaic parameters (short-circuit current density, *J*sc; open-circuit voltage, *V*oc; fill factor, *FF*; and efficiency, η) are summarized in Table 4.4.

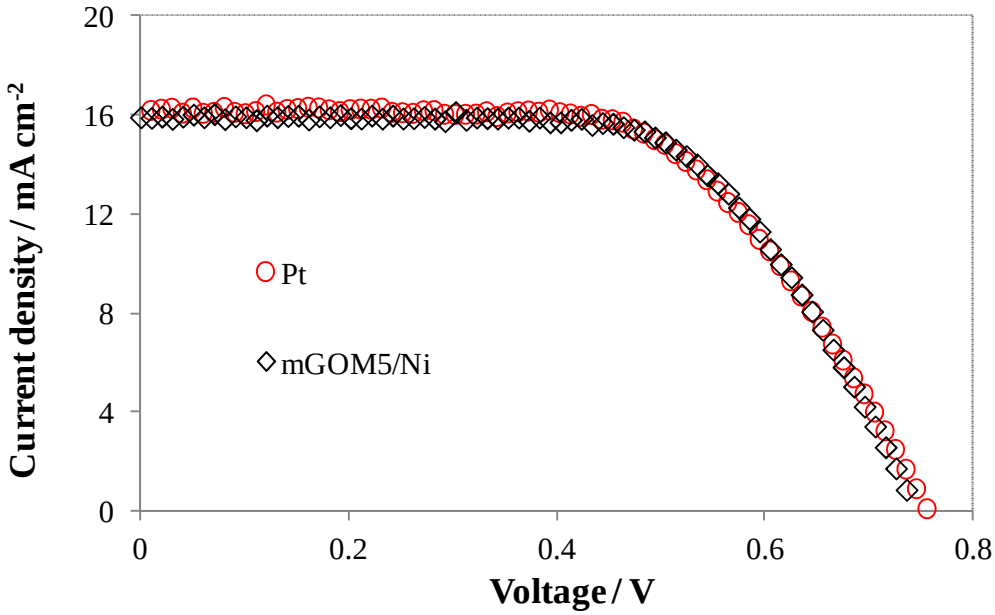

Figure 4.11 *I-V* characteristics measured at 1 sun (100 mW·m^{-2}; AM 1.5 G) of higher efficiency DSCs assembled with mGOM5/Ni and Pt CEs.

Table 4.4 *I-V* parameters of higher efficiency DSCs assembled with mGOM5/Ni and Pt CE.

CE	V_{OC} / V	J_{SC} / mA cm^{-2}	*FF*	η / %	$\Delta\eta$ / %	$\tau_{550\ nm}$ / %
Pt	0.76	16.2	0.61	7.45	---	92.0
mGOM5/Ni	0.74	15.8	0.64	7.51	0.76	80.6

From Table 4.4 it can be seen that the DSC prepared with the mGOM5/Ni CE have an efficiency of 7.51 %, very similar to the DSC with the platinum CE – 7.45%. The mGOM5/Ni CE yielded a higher *FF* than the Pt CE (0.64 vs. 0.61) a possible indication of the lower electronic resistance in the CE created by the Ni particles on the graphene platelets during the annealing stage.

The fabricated DSCs were also analysed by electrochemical impedance spectroscopy. EIS results presented in Figure 4.13 were obtained in dark conditions at an applied voltage corresponding to the typical DSC open-circuit voltage (0.7 V). In Nyquist plot, the left-hand side semicircle (corresponding to the high-frequency peak at ~1 kHz in the Bode diagram) reflects the electrocatalytic behaviour of the counter-electrode/electrolyte interface. The right-hand side semicircle in the Nyquist plot (medium-frequency peak in the Bode diagram, ~10 Hz) represents the phenomena occurring in the photoelectrode (charge transport/recombination) and is overlapped with the Nernst diffusion within the electrolyte. To better interpret the DSCs results, the EIS data was fitted according to a simplified transmission line electrical analogue model, as shown in Figure 4.12 [53, 54]. The model was used assuming that at the measured open-circuit voltages the electronic transport resistance in the semiconductor was negligible and thus the transmission line only takes in consideration the recombination resistance between electrons at the TiO_2 and the electrolyte [53, 54]. The respective fitted parameters are shown in Table 4.5.

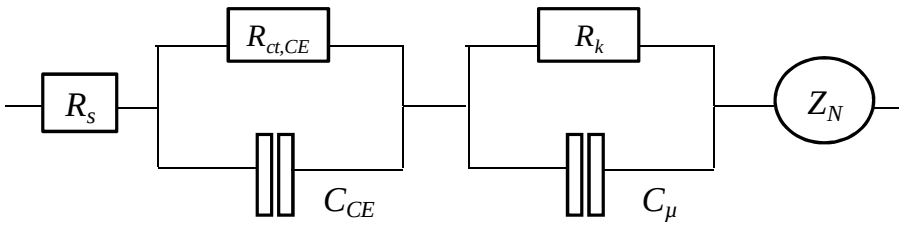

Figure 4.12 Electrical analogue used for fitting the electrochemical impedance spectra data of DSCs.

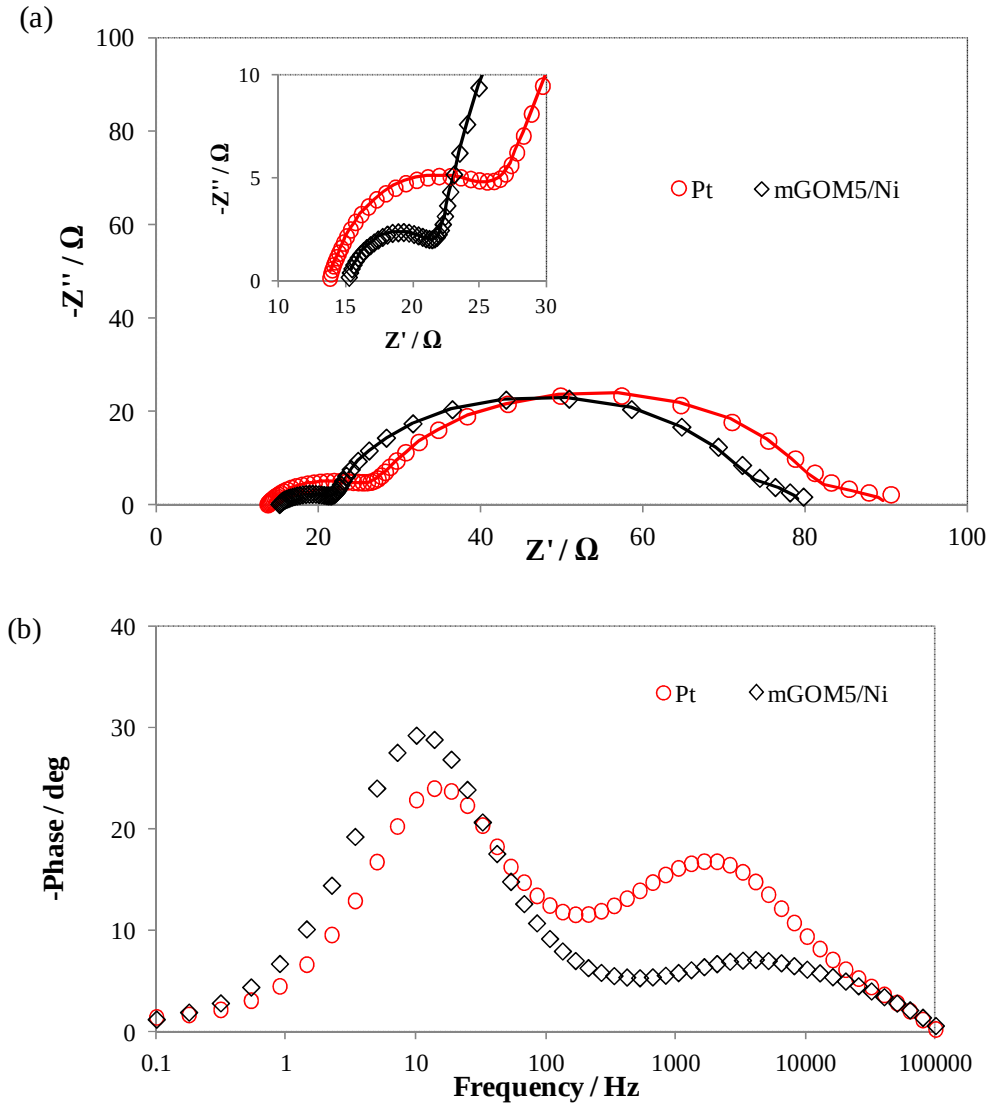

Figure 4.13 Nyquist (a) and Bode (b) diagrams obtained in the dark under a bias corresponding to the DSC's open-circuit voltage, of higher efficiency DSCs assembled with mGOM5/Ni and Pt CEs. For Nyquist diagram (a) full symbols represent the experimental data and solid lines represent the model fitting. On the inset of the Nyquist diagrams (a) is represented the close-up of the semicircle corresponding to the CE's resistances.

Table 4.5 EIS fitted parameters of higher efficiency DSCs assembled with mGOM5/Ni and Pt CE.

CE	R_s / Ω	$R_{ct,CE}$ / Ω cm^2	j_0 / mA cm^{-2}	$\tau\mu_{TiO2}$ / ms	*Redox frequency*/ Hz
Pt	13.7	5.34	4.89	19.7	1648
mGOM5/Ni	15.1	2.76	9.45	28.0	4104

The mGOM5/Ni CE exhibited a lower R_{ct} and as consequence a higher FF (indicative of a higher electrocatalytic activity) than the Pt CE - Table 4.5. R_{ct} and R_s values obtained from the EIS fittings for DSCs prepared with the graphene-based and Pt CEs - Table 4.5, were very similar to those obtained from the half-cells configuration - Table 4.3. Some studies have shown dependence of performance with the thickness of graphene films (and therefore with their transparency) [4, 11]. However, in this case, due to aforementioned similar resistances, the influence caused by the difference in transmittance of mGOM5/Ni CEs used in both types of DSCs (~5 % for $\tau_{550\ nm}$) can be neglected. The $\Delta\eta$ between the DSCs fabricated with mGOM5/Ni CE and Pt CEs is only 0.76 % (smaller than the results of the half-cells could suggest - section 4.3.2). It is possible that for mGOM5/Ni CE, the effect of its lower R_{ct} was undermined by the higher R_s (15.1 Ω vs 13.7 Ω for the Pt CE). The higher ohmic resistance would have hindered the flow of electrons through the cell limiting its overall efficiency [44, 55]. Nevertheless the mGOM5/Ni CE has shown a tremendous potential for the replacement of Pt as an equally efficient material for the electrocatalytic activity of the I_3^-/I^- redox reaction while being able to simultaneously provide a high optical transparency to the electrode.

Additionally, to further understand the great performance displayed by the mGOM5/Ni CE it were constructed DSCs with two other CEs that suffered the same thermal annealing as the graphene-based CEs: Ni (or FTO/Ni) CE and

mGOM5/Au CE. The latter CE had deposited on the FTO surface gold particles instead of nickel particles. The amount of Au particles that were deposited by sputtering was similar to the amount of Ni particles deposited by electrophoretic deposition (see transmittances values in Table 4.4). Additionally DSCs with the mGOM5 and Pt CEs were fabricated for comparison. Fabricated DSCs for this comparative analysis had less efficient TiO_2 photoanodes thus resulting in lower solar efficiency conversions. Once again it was used an acetonitrile-base medium electrolyte to study the electrocatalytic activity of the graphene-based CES towards the I_3^-/I^- redox couple. The fabricated mGOM5/Ni CE was slightly more transparent than the one used in the higher efficiency DSCs ($\tau_{550\ nm}$ = 85.7% vs. 80.6 %), but similar to that used for the half-cell tests (86 %).

Figure 4.14 shows the *I–V* characteristic curves for the different DSCs prepared. The corresponding photovoltaic parameters are summarized in Table 4.6.

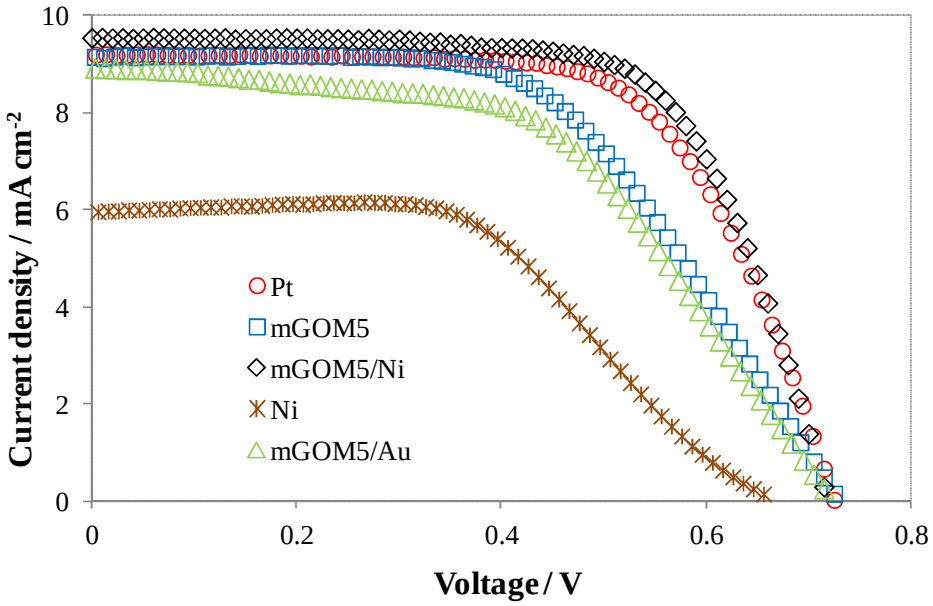

Figure 4.14 *I-V* characteristics measured at 1 sun (100 mW·m^{-2}; AM 1.5 G) of DSCs assembled with mGOM5, mGOM5/Ni, Pt, Ni and mGOM5/Au CEs.

Table 4.6 *I-V* parameters for DSCs fabricated with mGOM5, mGOM5/Ni, Pt, Ni and mGOM5/Au CEs.

CE	V_{OC} / V	J_{SC} / mA cm^{-2}	*FF*	η / %	$\Delta\eta$ / %	$\tau_{550\ nm}$ / %
Pt	0.73	9.31	0.65	4.38	---	95.5
mGOM5	0.72	8.95	0.57	3.74	-14.7	86.5
mGOM5/Ni	0.71	9.42	0.69	4.65	6.20	85.7
Ni	0.67	5.97	0.54	2.16	-50.6	99.5
mGOM5/Au	0.72	8.80	0.56	3.57	-18.5	88.3

The fabricated DSCs were also analysed by electrochemical impedance spectroscopy - Figure 4.15. The EIS fitting parameters are summarized in Table 4.7.

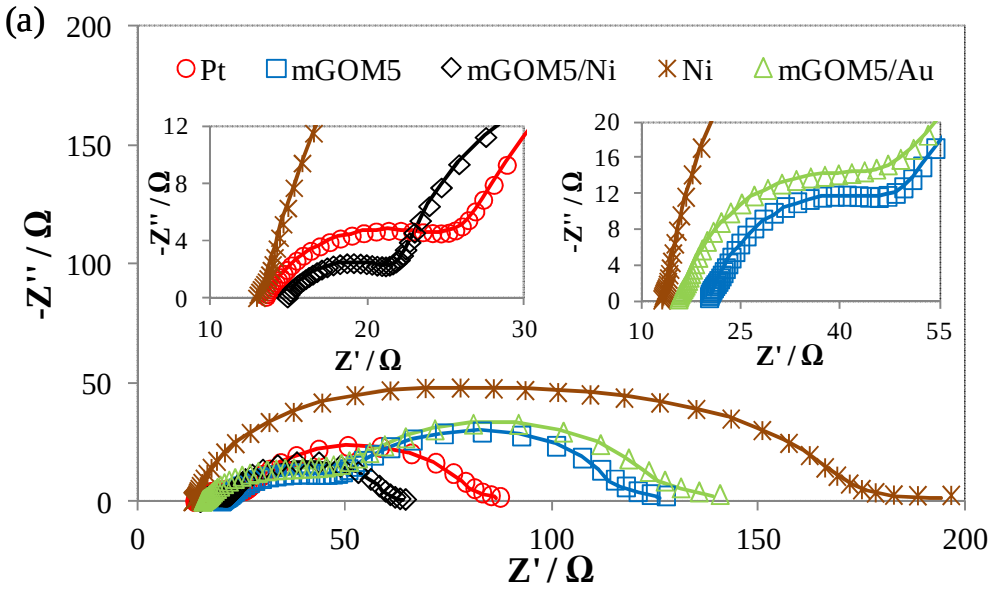

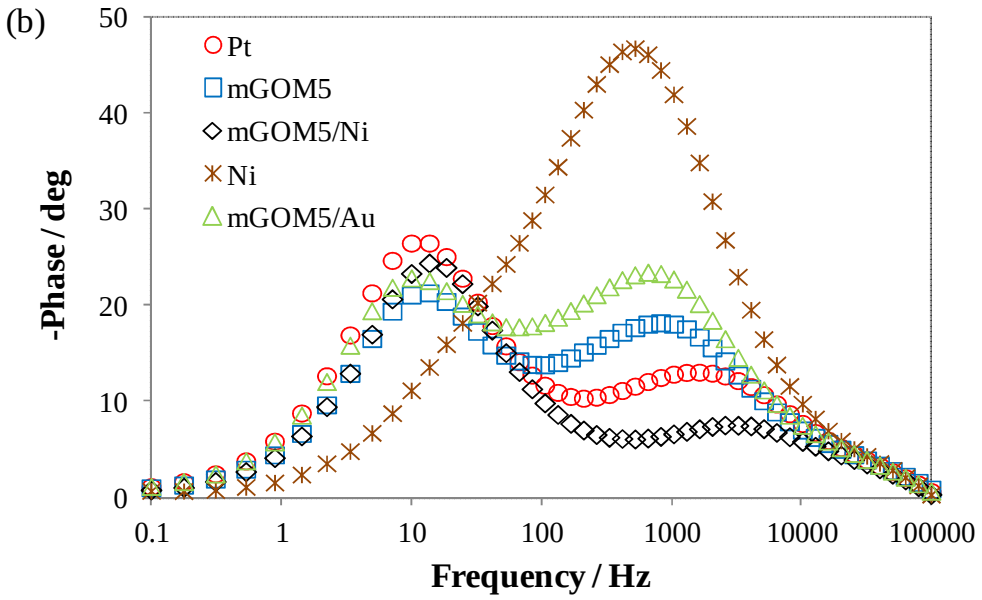

Figure 4.15 Nyquist (a) and Bode (b) diagrams obtained in the dark under a bias corresponding to the DSC's open-circuit voltage (0.7 V), for DSCs assembled with mGOM5, mGOM5/Ni, Pt, Ni and mGOM5/Au CEs. Symbols represent the experimental data and solid lines represent the model fitting. On the insets of the Nyquist diagrams are represented the close-up of the semicircle corresponding to the CE resistance.

Table 4.7 EIS fitted parameters for DSCs fabricated with mGOM5, mGOM5/Ni, Pt, Ni and mGOM5/Au CEs.

CE	R_s / Ω	$R_{ct,CE}$ / Ω cm^2	j_0 / mA cm^{-2}	$\tau\mu_{TiO2}$ / ms	*Redox frequency*/ Hz
Pt	13.5	5.13	5.08	25.6	1648
mGOM5	20.2	12.3	2.12	22.7	831.5
mGOM5/ni	14.8	2.86	9.10	19.2	2601
Ni	13.1	16.9	1.55	4.56	527.0
mGOM5/Au	15.6	13.5	1.93	28.2	662.0

The DSC constructed with mGOM5/Ni CE outperformed the Pt CE, having an efficiency of 4.65 % vs. 4.38 %, respectively. This represented a relative difference in energy conversion efficiency of $\Delta\eta$, of 6.2 %. The main difference resided in the fill factor value that was higher for the mGOM5/Ni CE DSC (0.69 vs 0.65 for the Pt CE). This is a clear indication of the lower electronic resistance in the CE created by the Ni particles on the graphene platelets during the annealing stage. Conversely, the mGOM5 CE had a lower efficiency mainly due to a lower *FF* (0.57), a direct consequence of the higher charge-transfer resistance.

R_{ct} and R_s values obtained from the EIS fittings for the DSCs fabricated with the mGOM5/Ni and Pt CEs – Table 4.7, were mostly the same as before - Table 4.5. It can be seen that mGOM5/Ni CE had the lowest R_{ct}, corresponding to a higher electrocatalytic activity. This is also supported from the higher (redox) frequency peak in the Bode diagram (2601 s^{-1} for mGOM5/Ni CE vs 1648 $s^{-}1$ for Pt CE), another indication of the lower charge-transfer resistance [56]. Notice that the mGOM5 CE was the only CE yielding a j_o (9.1 mA cm^{-2}) similar to the photocurrent density of the DSC's photoanode (9.4 mA cm^{-2}), another indication of an efficient CE [43-46]. It is also important to notice that the DSC prepared with the mGOM5/Ni CE, despite having a lower electron life time, τ_μ - 19.2 ms vs 25.6 ms for the DSC that had the Pt CE, and therefore more recombination of electrons in the TiO_2, still yields a higher efficiency.

The DSC constructed with the Ni CE yielded a very poor efficiency, 2.16 % ($\Delta\eta$ of -50.6 %), consequence of a lower FF (higher R_{ct} and lower frequency peak in the Bode diagram), lower V_{oc} and J_{sc}, suggesting that the Ni particles were not responsible for the increase of catalytic activity observed in the mGOM5/Ni CE. Curiously, the Ni CE had a lower R_s than the mGOM5/Ni CE, indicating a lower ohmic resistance between the FTO and the catalytic material. The Ni CE displayed a transmittance of 99.5 %, an indication that only a very small amount of Ni was electrophoretically deposited.

The mGOM5/Au CE yielded a DSC with efficiency similar to the mGOM5 CE (3.57 % and 3.74 % respectively). It displayed similar *FF* (0.56 vs 0.57), translated into similar R_{ct}, and therefore similar j_o. However, the mGOM5/Au CE had improved R_s (15.6 Ω vs 20.2 Ω for the mGOM5 CE). It appeared that the gold particles decreased the ohmic resistances between the FTO substrate and the graphene platelets but did not improve their intrinsic catalytic behaviour, furthermore supporting the idea of restoration of electronic double bonds along the platelets, caused by the nickel particles.

In summary it was shown that the mGOM5/Ni CE was able to combine high transparency with high electrocatalytic activity of the I_3^-/I^- redox reaction, making it a front-runner candidate to replace Pt.

4.3.4. Preliminary stability tests

Preliminary stability tests were performed on some of the aforementioned DSCs in section 4.3.3, specifically DSCs fabricated with the mGOM5, mGOM5/Ni and Pt CEs. These cells were placed under dark at room temperature and *I-V* and EIS measurements were taken as a function of time for more than 1000 h - Figure 4.16. In Figure 4.16 (a) to (e) are represented the relative values of the *I-V* parameters of each cell measured at standard conditions (1 Sun, AM=1.5, 20 ºC), in regard to their initial value. Figure 4.16 (f) and (g) show the absolute values of the EIS parameters of the same cells obtained in the dark under a bias corresponding to the DSC's open-circuit voltage (0.7 V). The initial values of the *I-V* and EIS parameters can be checked in Table 4.6 and Table 4.7 respectively.

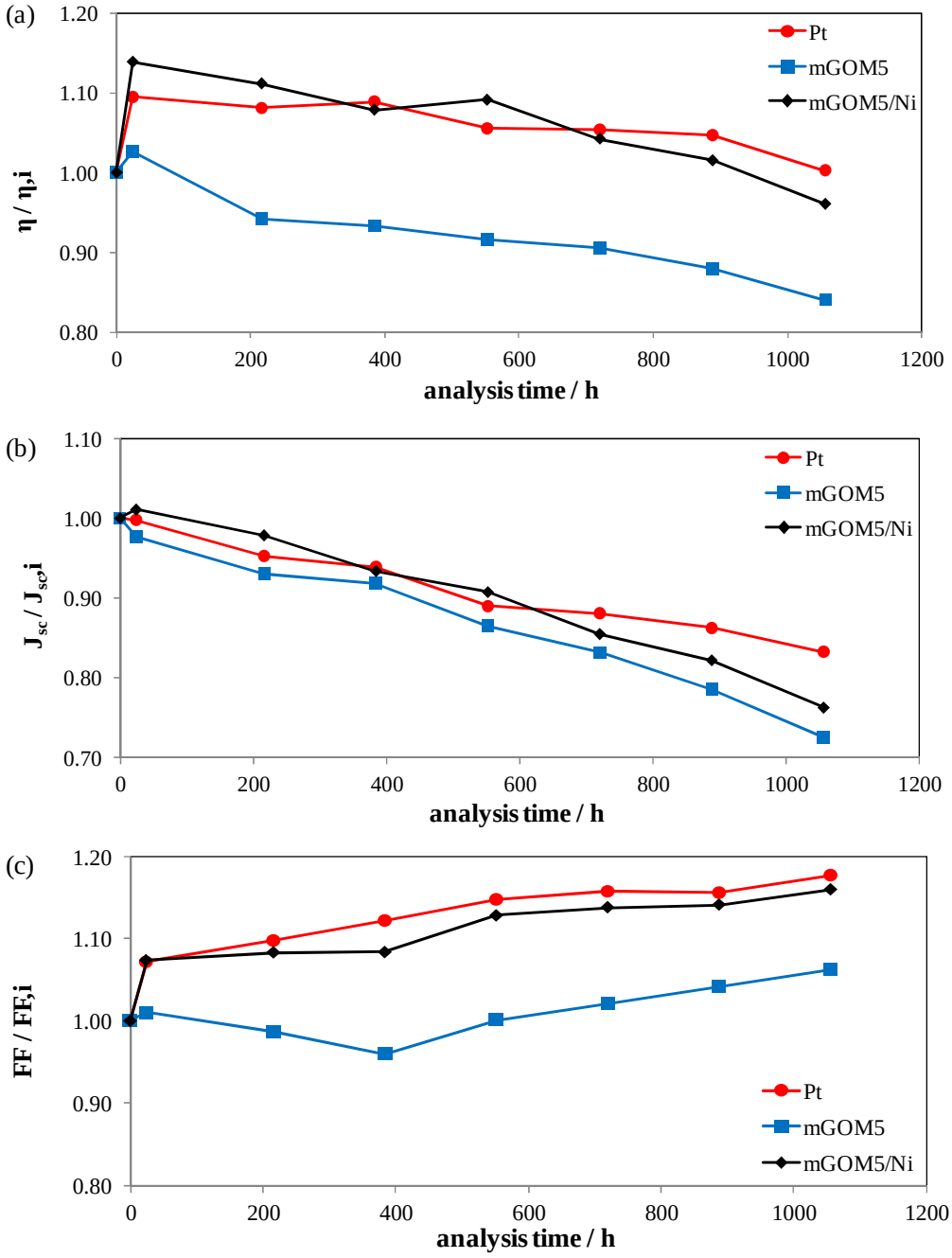
(a)
1.20
1.10
1.00
0.90
0.80
η / η,i
0
200
400
600
800
1000
1200
analysis time / h
Pt
mGOM5
mGOM5/Ni
(b)
1.10
1.00
0.90
0.80
0.70
Jsc / Jsc,i
0
200
400
600
800
1000
1200
analysis time / h
Pt
mGOM5
mGOM5/Ni
(c)
1.20
1.10
1.00
0.90
0.80
FF / FF,i
0
200
400
600
800
1000
1200
analysis time / h
Pt
mGOM5
mGOM5/Ni

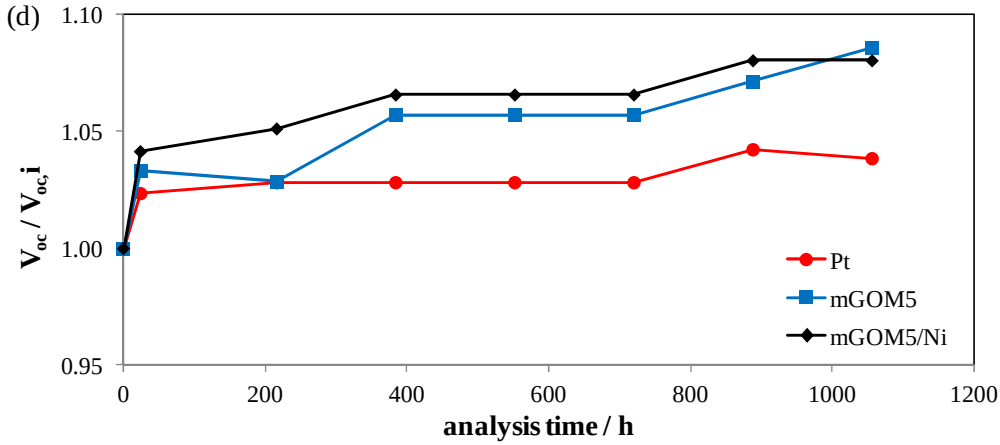
(d)
1.10
1.05
1.00
0.95
V_{oc} / $V_{oc,i}$
0
200
400
600
800
1000
1200
analysis time / h
Pt
mGOM5
mGOM5/Ni

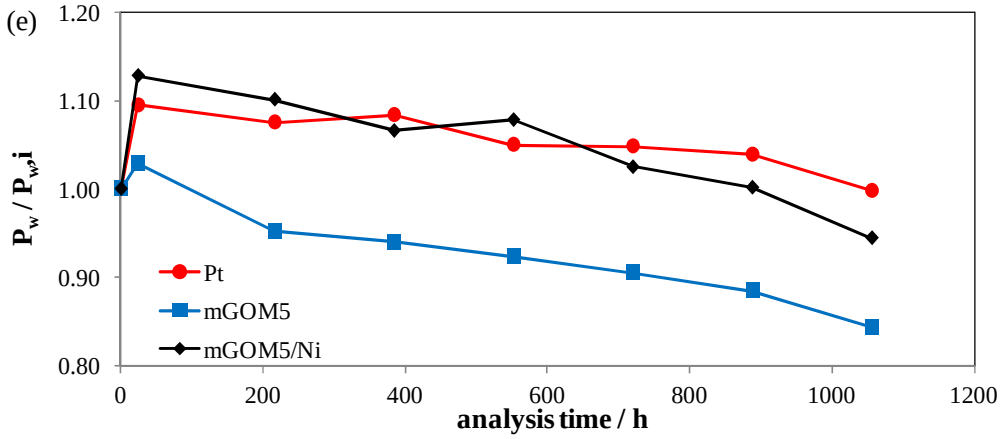
(e)
1.20
1.10
1.00
0.90
0.80
P_w / $P_{w,i}$
0
200
400
600
800
1000
1200
analysis time / h
Pt
mGOM5
mGOM5/Ni

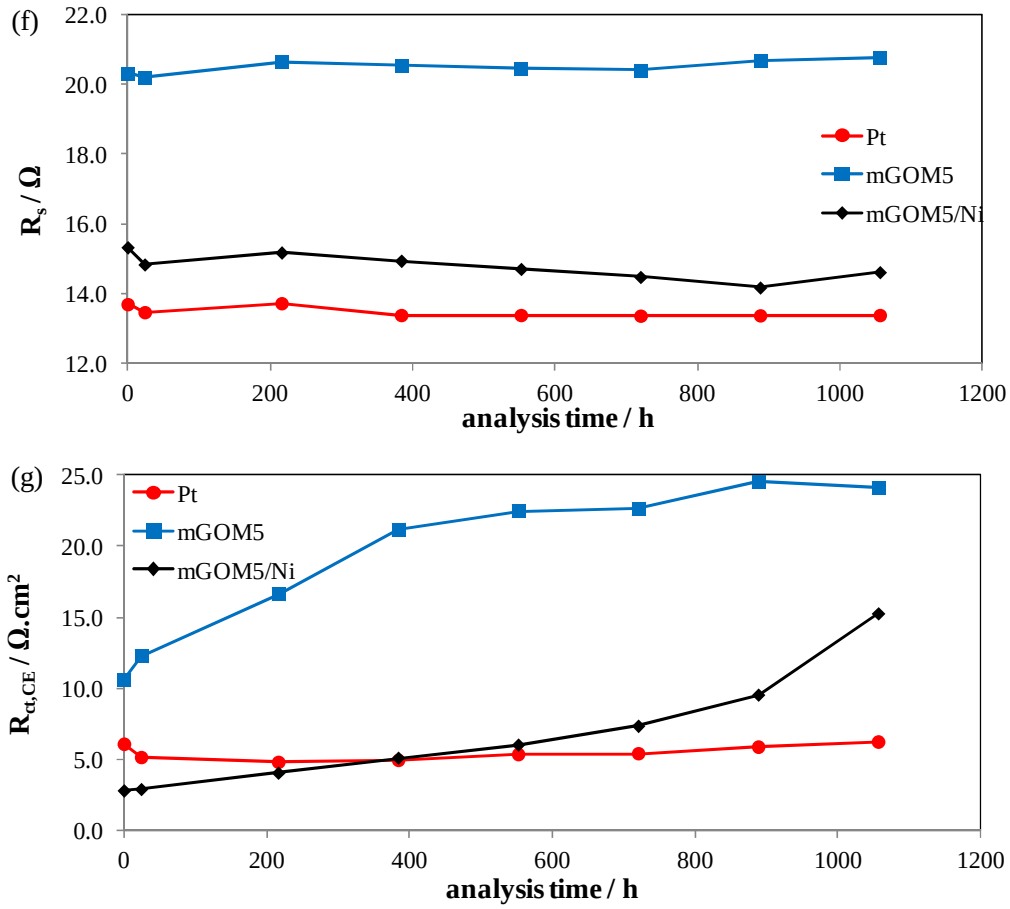

Figure 4.16 Stability test: *I-V* and EIS measurements taken from DSCs assembled with mGOM5, mGOM5/Ni and Pt CEs and placed under dark at room temperature for more than 1000 h: a) efficiency, *η;* b) short-current density, *J*sc; c) fill factor, *FF*; d) open-circuit voltage, *V*oc; e) point of maximum power, P_w; f) series resistance, R_s; g) charge transfer resistance, R_{ct}. *I-V* performed at 1 sun (100 mW·m^{-2}; AM 1.5 G) and EIS obtained in the dark under a bias corresponding to the DSC's open-circuit voltage (0.7 V). (a) to (e) display the relative values of the I-V parameters of each cell measured at standard conditions (1 Sun, AM=1.5, 20 ºC), in regard to their initial value; (f) and (g) show the absolute values of the EIS parameters of the same cells.

From Figure 4.16 it can be seen than there was a loss of efficiency as a function of time for all CEs and these efficiency losses display the same trend for each CE; this is a consequence of degradation occurring in the cells. Since

the electrolyte solvent is acetonitrile based, DSCs are not stable for a long period of time. It can be seen that the degradation is mostly due to continuous damage in the photoanode, as the J_{sc} sharply decreases over time - Figure 4.16, b). This is a consequence of dye desorption caused by acetonitrile or water contamination [57-60]. Curiously both graphene-based CEs display a relative efficiency loss from their maximum point of ~ 18%, an indication that Ni particles are not related to this loss. Although not directly visible from Figure 4.16, after 900 h the platinum CE based DSC's efficiency surpassed the one with mGOM5/Ni CE. After 1000 h, whilst DSC with mGOM5 CE lost more than 15% of its original efficiency, the one DSC with mGOM5/Ni CE had only lost 4% of its efficiency and maximum power relative to the initial value (the IEC61646 standard requires that degradation of maximum power at standard testing conditions should not exceed 5 % [61]). R_s is almost constant throughout all experiments suggesting that the structure of the film must not had been modified. However, the major difference can be seen in the R_{ct} - Figure 4.16, g). While the R_{ct} of Pt CE remained unchanged, the R_{ct} of mGOM5/Ni CE increased over time surpassing the Pt CE value at the instant ~500 h. As the same behaviour was seen for mGOM5 CE, it is possible that it might have occurred some contamination from dye molecules that were desorbed from the TiO_2 interface or as consequence of adsorption of iodine or iodide molecules onto the graphene surface [27, 62]. Nevertheless, the results hint that the mGOM5/Ni CE is apparently as stable as Pt for iodide / triiodide electrolytes, although further tests must be performed.

4.4. Conclusions

A new counter-electrode to be used in dye-sensitized solar cells employing the I_3^-/I^- redox couple was developed. This novel CE (mGOM5/Ni) was produced by spray deposition of oxidized commercial graphene nanoplatelets onto FTO substrates decorated with a very small amount of electrophoretically

deposited nickel particles, followed by thermal annealing in an inert atmosphere. Electrochemical impedance spectroscopy (EIS) results of half-cells and DSCs showed a low charge-transfer resistance (R_{ct}) for the mGOM5/Ni CE. As consequence, DSCs assembled with such CEs exhibited efficiencies equal or superior to the Pt CE, mainly derived from an increase in *FF* (consequence of internal resistances decrease). SEM, AFM and Raman analysis suggest that Ni particles had been responsible for partial restitution of electronic conduction in the oxidized graphene platelets during the thermal annealing, essential for the high electrocatalytic activity demonstrated by the mGOM5/Ni CE. The mGOM5/Ni CE also offers high transparency (transmission at 550 nm > 80 %) making it the front-runner replacement of Pt for I_3^-/I^- based electrolytes. Preliminary stability studies suggest that the mGOM5/Ni CE has similar stability as the Pt CE. Future studies will focus on extending the use of this novel CE to other redox couple systems (ferrocene [63] or cobalt complexes [45]). Further detailed stability experiments must also be completed.

Acknowledgments

Rui Cruz is grateful to the Portuguese Foundation for Science and Technology (FCT) and Efacec – Engenharia e Sistemas S.A. for his Ph.D grant (SFRH/BDE/33439/2008). This work was accomplished in the framework of the project WinDSC SI&IDT (ref. 21539/2011), co-financed by the European Regional Development Fund and the Portuguese Government through ADI – Agência de Inovação, under the framework of the QREN Initiative, through the Operational Programme for Competitiveness Factors. R. Cruz also acknowledges project SolarConcept (PTDC/EQU-EQU/120064/2010) for funding.

References

1. O'Regan, B. and M. Grätzel, *A Low-Cost, High-Efficiency Solar-Cell Based on Dye-Sensitized Colloidal TiO_2 Films.* Nature, 1991. **353**(6346): p. 737-740.
2. Grätzel, M., *Photoelectrochemical cells.* Nature, 2001. **414**(6861): p. 338-344.
3. Smestad, G., C. Bignozzi, and R. Argazzi, *Testing of dye sensitized TiO2 solar cells I: Experimental photocurrent output and conversion efficiencies.* Solar Energy Materials and Solar Cells, 1994. **32**(3): p. 259-272.
4. Kavan, L., J.H. Yum, and M. Grätzel, *Optically Transparent Cathode for Dye-Sensitized Solar Cells Based on Graphene Nanoplatelets.* Acs Nano, 2010. **5**(1): p. 165-172.
5. Hamann, T.W. and J.W. Ondersma, *Dye-sensitized solar cell redox shuttles.* Energy & Environmental Science, 2011. **4**(2): p. 370-381.
6. Grätzel, M., *The artificial leaf, bio-mimetic photocatalysis.* Cattech, 1999. **3**: p. 3–17.
7. Yamaguchi, T., Y. Uchida, S. Agatsuma, and H. Arakawa, *Series-connected tandem dye-sensitized solar cell for improving efficiency to more than 10%.* Solar Energy Materials and Solar Cells, 2009. **93**(6-7): p. 733-736.
8. Andrade, L., R. Cruz, H.A. Ribeiro, and A. Mendes, *Impedance characterization of dye-sensitized solar cells in a tandem arrangement for hydrogen production by water splitting.* International Journal of Hydrogen Energy, 2010. **35**(17): p. 8876-8883.
9. Geim, A.K. and K.S. Novoselov, *The rise of graphene.* Nature Materials, 2007. **6**(3): p. 183-191.

10. Nair, R.R., P. Blake, A.N. Grigorenko, K.S. Novoselov, T.J. Booth, T. Stauber, N.M.R. Peres, and A.K. Geim, *Fine Structure Constant Defines Visual Transparency of Graphene.* Science, 2008. **320**(5881): p. 1308-1308.
11. Roy-Mayhew, J.D., D.J. Bozym, C. Punckt, and I.A. Aksay, *Functionalized Graphene as a Catalytic Counter Electrode in Dye-Sensitized Solar Cells.* Acs Nano, 2010. **4**(10): p. 6203-6211.
12. Tang, L., Y. Wang, Y. Li, H. Feng, J. Lu, and J. Li, *Preparation, Structure, and Electrochemical Properties of Reduced Graphene Sheet Films.* Advanced Functional Materials, 2009. **19**(17): p. 2782-2789.
13. Begum, P., R. Ikhtiari, and B. Fugetsu, *Graphene phytotoxicity in the seedling stage of cabbage, tomato, red spinach, and lettuce.* Carbon, 2011. **49**(12): p. 3907-3919.
14. Chang, Y., S.-T. Yang, J.-H. Liu, E. Dong, Y. Wang, A. Cao, Y. Liu, and H. Wang, *In vitro toxicity evaluation of graphene oxide on A549 cells.* Toxicology Letters, 2011. **200**(3): p. 201-210.
15. Fisher, C., A. E. Rider, Z. Jun Han, S. Kumar, I. Levchenko, and K. Ostrikov, *Applications and Nanotoxicity of Carbon Nanotubes and Graphene in Biomedicine.* Journal of Nanomaterials, 2012. **2012**: p. 1-19.
16. Khodakovskaya, M.V., K. de Silva, D.A. Nedosekin, E. Dervishi, A.S. Biris, E.V. Shashkov, E.I. Galanzha, and V.P. Zharov, *Complex genetic, photothermal, and photoacoustic analysis of nanoparticle-plant interactions.* Proceedings of the National Academy of Sciences of the United States of America, 2011. **108**(3): p. 1028-1033.
17. Trancik, J.E., S.C. Barton, and J. Hone, *Transparent and catalytic carbon nanotube films.* Nano Letters, 2008. **8**(4): p. 982-987.

18. Hong, W.J., Y.X. Xu, G.W. Lu, C. Li, and G.Q. Shi, *Transparent graphene/PEDOT-PSS composite films as counter electrodes of dye-sensitized solar cells.* Electrochemistry Communications, 2008. **10**(10): p. 1555-1558.

19. Zhang, D.W., X.D. Li, S. Chen, H.B. Li, Z. Sun, X.J. Yin, and S.M. Huang. *Graphene Nanosheet Counter-Electrodes for Dye-Sensitized Solar Cells*. in *Nanoelectronics Conference (INEC), 2010 3rd International*. 2010. New York.

20. Murakami, T. and M. Grätzel, *Counter electrodes for DSC: Application of functional materials as catalysts.* Inorganica Chimica Acta, 2008. **361**(3): p. 572-580.

21. Wang, X., L.J. Zhi, and K. Mullen, *Transparent, conductive graphene electrodes for dye-sensitized solar cells.* Nano Letters, 2008. **8**(1): p. 323-327.

22. Xu, Y., H. Bai, G. Lu, C. Li, and G. Shi, *Flexible Graphene Films via the Filtration of Water-Soluble Noncovalent Functionalized Graphene Sheets.* Journal of the American Chemical Society, 2008. **130**(18): p. 5856-5857.

23. Wan, L., S. Wang, X. Wang, B. Dong, Z. Xu, X. Zhang, B. Yang, S. Peng, J. Wang, and C. Xu, *Room-temperature fabrication of graphene films on variable substrates and its use as counter electrodes for dye-sensitized solar cells.* Solid State Sciences, 2011. **13**(2): p. 468-475.

24. Cruz, R., D.A. Pacheco Tanaka, and A. Mendes, *Reduced graphene oxide films as transparent counter-electrodes for dye-sensitized solar cells.* Solar Energy, 2012. **86**(2): p. 716-724.

25. Stankovich, S., D.A. Dikin, R.D. Piner, K.A. Kohlhaas, A. Kleinhammes, Y. Jia, Y. Wu, S.T. Nguyen, and R.S. Ruoff, *Synthesis of*

graphene-based nanosheets via chemical reduction of exfoliated graphite oxide. Carbon, 2007. **45**(7): p. 1558-1565.

26. Hummers, W.S. and R.E. Offeman, *Preparation of Graphitic Oxide.* Journal of the American Chemical Society, 1958. **80**(6): p. 1339-1339.
27. Hauch, A. and A. Georg, *Diffusion in the electrolyte and charge-transfer reaction at the platinum electrode in dye-sensitized solar cells.* Electrochimica Acta, 2001. **46**(22): p. 3457-3466.
28. Yen, M.Y., C.C. Teng, M.C. Hsiao, P.I. Liu, W.P. Chuang, C.C.M. Ma, C.K. Hsieh, M.C. Tsai, and C.H. Tsai, *Platinum nanoparticles/graphene composite catalyst as a novel composite counter electrode for high performance dye-sensitized solar cells.* Journal of Materials Chemistry, 2011. **21**(34): p. 12880-12888.
29. Kim, C.J., W. Khan, and S.Y. Park, *Structural evolution of graphite oxide during heat treatment.* Chemical Physics Letters, 2011. **511**(1-3): p. 110-115.
30. Xu, C., X. Wang, and J. Zhu, *Graphene−Metal Particle Nanocomposites.* The Journal of Physical Chemistry C, 2008. **112**(50): p. 19841-19845.
31. Wu, Z.-S., S. Pei, W. Ren, D. Tang, L. Gao, B. Liu, F. Li, C. Liu, and H.-M. Cheng, *Field Emission of Single-Layer Graphene Films Prepared by Electrophoretic Deposition.* Advanced Materials, 2009. **21**(17): p. 1756-1760.
32. Van der Biest, O.O. and L.J. Vandeperre, *Electrophoretic deposition of materials.* Annual Review of Materials Science, 1999. **29**(1): p. 327-352.
33. Ma, T., X. Fang, M. Akiyama, K. Inoue, H. Noma, and E. Abe, *Properties of several types of novel counter electrodes for dye-sensitized*

solar cells. Journal of Electroanalytical Chemistry, 2004. **574**(1): p. 77-83.

34. Okada, K., H. Matsui, T. Kawashima, T. Ezure, and N. Tanabe, *100 mm × 100 mm large-sized dye sensitized solar cells.* Journal of Photochemistry and Photobiology A: Chemistry, 2004. **164**(1-3): p. 193-198.
35. Dresselhaus, M.S., A. Jorio, M. Hofmann, G. Dresselhaus, and R. Saito, *Perspectives on Carbon Nanotubes and Graphene Raman Spectroscopy.* Nano Letters, 2010. **10**(3): p. 751-758.
36. Charlier, J.C., P.C. Eklund, J. Zhu, and A.C. Ferrari, *Electron and Phonon Properties of Graphene: Their Relationship with Carbon Nanotubes*, in *Carbon Nanotubes*. 2008, Springer Berlin Heidelberg. p. 673-709.
37. Ferrari, A.C., J.C. Meyer, V. Scardaci, C. Casiraghi, M. Lazzeri, F. Mauri, S. Piscanec, D. Jiang, K.S. Novoselov, S. Roth, and A.K. Geim, *Raman Spectrum of Graphene and Graphene Layers.* Physical Review Letters, 2006. **97**(18): p. 187401.
38. Pimenta, M.A., G. Dresselhaus, M.S. Dresselhaus, L.G. Cancado, A. Jorio, and R. Saito, *Studying disorder in graphite-based systems by Raman spectroscopy.* Physical Chemistry Chemical Physics, 2007. **9**(11): p. 1276-1290.
39. Dikin, D.A., S. Stankovich, E.J. Zimney, R.D. Piner, G.H.B. Dommett, G. Evmenenko, S.T. Nguyen, and R.S. Ruoff, *Preparation and characterization of graphene oxide paper.* Nature, 2007. **448**(7152): p. 457-460.
40. Zhan, D., Z. Ni, W. Chen, L. Sun, Z. Luo, L. Lai, T. Yu, A.T.S. Wee, and Z. Shen, *Electronic structure of graphite oxide and thermally reduced graphite oxide.* Carbon, 2011. **49**(4): p. 1362-1366.

41. Wang, S.J., Y. Geng, Q. Zheng, and J.-K. Kim, *Fabrication of highly conducting and transparent graphene films.* Carbon, 2010. **48**(6): p. 1815-1823.

42. Xu, Y.F., G.K. Long, L. Huang, Y. Huang, X.J. Wan, Y.F. Ma, and Y.S. Chen, *Polymer photovoltaic devices with transparent graphene electrodes produced by spin-casting.* Carbon, 2010. **48**(11): p. 3308-3311.

43. Hagfeldt, A., G. Boschloo, L. Sun, L. Kloo, and H. Pettersson, *Dye-Sensitized Solar Cells.* Chemical Reviews, 2010. **110**(11): p. 6595-6663.

44. Aitola, K., J. Halme, N. Halonen, A. Kaskela, M. Toivola, A.G. Nasibulin, K. Kordás, G. Tóth, E.I. Kauppinen, and P.D. Lund, *Comparison of dye solar cell counter electrodes based on different carbon nanostructures.* Thin Solid Films, 2011. **519**(22): p. 8125-8134.

45. Kavan, L., J.-H. Yum, and M. Grätzel, *Graphene Nanoplatelets Outperforming Platinum as the Electrocatalyst in Co-Bipyridine-Mediated Dye-Sensitized Solar Cells.* Nano Letters, 2011. **11**(12): p. 5501-5506.

46. Papageorgiou, N., W. Maier, and M. Grätzel, *An Iodine/Triiodide Reduction Electrocatalyst for Aqueous and Organic Media.* Journal of The Electrochemical Society, 1997. **144**(3): p. 876-884.

47. Velten, J., A.J. Mozer, D. Li, D. Officer, G. Wallace, R. Baughman, and A. Zakhidov, *Carbon nanotube/graphene nanocomposite as efficient counter electrodes in dye-sensitized solar cells.* Nanotechnology, 2012. **23**(8).

48. Choi, W., I. Lahiri, R. Seelaboyina, and Y.S. Kang, *Synthesis of Graphene and Its Applications: A Review.* Critical Reviews in Solid State and Materials Sciences, 2010. **35**(1): p. 52-71.

49. Somani, P.R., S.P. Somani, and M. Umeno, Chem. Phys. Lett., 2006. **430**: p. 56.

50. Halme, J., P. Vahermaa, K. Miettunen, and P. Lund, *Device Physics of Dye Solar Cells.* Advanced Materials, 2010. **22**(35): p. E210-E234.

51. Wu, M., J. Bai, Y. Wang, A. Wang, X. Lin, L. Wang, Y. Shen, Z. Wang, A. Hagfeldt, and T. Ma, *High-performance phosphide/carbon counter electrode for both iodide and organic redox couples in dye-sensitized solar cells.* Journal of Materials Chemistry, 2012. **22**(22): p. 11121-11127.

52. Wu, M.X., X. Lin, T.H. Wang, J.S. Qiu, and T.L. Ma, *Low-cost dye-sensitized solar cell based on nine kinds of carbon counter electrodes.* Energy & Environmental Science, 2011. **4**(6): p. 2308-2315.

53. Kern, R., R. Sastrawan, J. Ferber, R. Stangl, and J. Luther, *Modeling and interpretation of electrical impedance spectra of dye solar cells operated under open-circuit conditions.* Electrochimica Acta, 2002. **47**(26): p. 4213-4225.

54. Andrade, L., J. Sousa, H.A. Ribeiro, and A. Mendes, *Phenomenological modeling of dye-sensitized solar cells under transient conditions.* Solar Energy, 2011. **85**(5): p. 781-793.

55. Seo, S.H., S.Y. Kim, B.-K. Koo, S.-I. Cha, and D.Y. Lee, *Influence of electrolyte composition on the photovoltaic performance and stability of dye-sensitized solar cells with multiwalled carbon nanotube catalysts.* Langmuir, 2010. **26**(12): p. 10341-10346.

56. Choi, H., H. Kim, S. Hwang, Y. Han, and M. Jeon, *Graphene counter electrodes for dye-sensitized solar cells prepared by electrophoretic deposition.* Journal of Materials Chemistry, 2011. **21**(21): p. 7548-7551.

57. Toivola, M., J. Halme, L. Peltokorpi, and P. Lund, *Investigation of Temperature and Aging Effects in Nanostructured Dye Solar Cells*

Studied by Electrochemical Impedance Spectroscopy. International Journal of Photoenergy, 2009: p. 15.

58. Bari, D., N. Wrachien, R. Tagliaferro, S. Penna, T.M. Brown, A. Reale, A. Di Carlo, G. Meneghesso, and A. Cester, *Thermal stress effects on Dye-Sensitized Solar Cells (DSSCs).* Microelectronics Reliability, 2011. **51**(9-11): p. 1762-1766.
59. Kato, N., K. Higuchi, H. Tanaka, J. Nakajima, T. Sano, and T. Toyoda, *Improvement in long-term stability of dye-sensitized solar cell for outdoor use.* Solar Energy Materials and Solar Cells, 2011. **95**(1): p. 301-305.
60. Kitamura, T., K. Okada, H. Matsui, and N. Tanabe, *Durability of Dye-Sensitized Solar Cells and Modules.* Journal of Solar Energy Engineering-Transactions of the Asme, 2010. **132**(2).
61. Harikisun, R. and H. Desilvestro, *Long-term stability of dye solar cells.* Solar Energy, 2011. **85**(6): p. 1179-1188.
62. Syrrokostas, G., A. Siokou, G. Leftheriotis, and P. Yianoulis, *Degradation mechanisms of Pt counter electrodes for dye sensitized solar cells.* Solar Energy Materials and Solar Cells, 2012. **103**: p. 119-127.
63. Daeneke, T., T.-H. Kwon, A.B. Holmes, N.W. Duffy, U. Bach, and L. Spiccia, *High-efficiency dye-sensitized solar cells with ferrocene-based electrolytes.* Nat Chem, 2011. **3**(3): p. 211-215.

Chapter 5

Glass-glass laser-assisted glass frit bonding

Rui Cruz, João Alexandre da Cruz Ranita, José Maçaira, Fernando Ribeiro, Ana Margarida Batista da Silva, José M. Oliveira, Maria Helena F. V. Fernandes, Helena Aguilar Ribeiro, Joaquim Gabriel Mendes and Adélio Mendes

(Ieee Transactions on Components Packaging and Manufacturing Technology, 2012. 2(12): p. 1949-1956, DOI: 10.1109/tcpmt.2012.2212195)

Abstract

A novel sealing method is proposed for encapsulating devices comprised of glass substrates. This sealing method is based on applying a glass frit paste cord onto the substrate and then using a laser beam to locally supply the necessary energy to allow the formation of a hermetic bonding layer. A detailed description of the laser bonding technique, the necessary equipment and method, and a preliminary study is carried out. The need to apply mechanical pressure during the bonding step is averted, thus facilitating the manufacturing process. The glass bonding cord obtained by the laser-assisted process was found to have an excellent contact with both substrates and no gas inclusions or voids were detected, indicating that an effective sealing was achieved. Preliminary hermeticity tests of the laser-bonded cells yielded encouraging results. The developed laser-assisted glass frit bonding process is a promising technique for obtaining hermetic sealing of photoelectronic and electrochemical devices, as it allows temperature-sensitive materials to be used inside them.

Keywords: Laser joining, glass substrate, lead-free glass frit.

5.1. Introduction

Over the years different joining techniques have been developed for the encapsulation of miniature micromechanical, optical and electronic devices that require a hermetic sealing with long-term stability. For example it is important for microelectromechanical systems (MEMS) [1, 2] to have an air tight sealing to prevent failure caused by the presence of moisture inside these devices. A commonly used joining technique is the glass frit bonding. In addition to ensure the formation of a hermetic seal it offers many other advantages as high bonding strength and process yield, low stress at the bonding interface, good process reproducibility and not requiring perfectly flat bonding surfaces [3]. Glass frit bonding can be applied in a vast number of applications such as microsensors [4] gyroscopes [3], complementary metal-oxide-semiconductor (CMOS) wafers [5] leadless chip carrier packages [6] and plasma display panels (PDPs) [7].

The glass frit bonding is a thermo-compressive process [3, 5]; it creates a bonding through the use of an intermediate layer placed between two substrates and subjected to pressure and heating (in the order of hundreds of degrees celsius), even for substrates with moderately rough surfaces. However, since it is required for the whole device to be heated, this can limit the use of multistep manufacturing processing and the use of temperature-sensitive processes and materials inside the devices, which may increase the complexity of the manufacturing process.

To cope with this issue more localized joining techniques have been developed, among them laser joining techniques. These techniques allow for dissimilar materials, such as borosilicate glass and fused silica substrates [8] or aluminium and steel [9], to be joined together through the creation of a direct bond without using an intermediate layer. However, they require the use of very clean and smooth surfaces and high bonding temperatures.

Combining glass frit bonding and laser joining techniques results in what may be defined as a “laser-assisted glass frit bonding technique” that shares the advantages of both aforementioned techniques. Accordingly, this new technique would allow localized heating of the sealing material thus protecting any temperature-sensitive materials located inside the devices. Additionally it would allow for a much faster and easier sealing process. In 2010, Wu *et al*. [6] described a technique that follows the laser-assisted glass frit bonding principle. These authors bonded different ceramic, silicon and aluminium-based materials using a low-melting temperature glass frit. To accomplish that, the glass frit was heated indirectly, up to the required bonding temperature, through heat conduction as a result of the laser beam being fired at metallic or silicon pieces placed above the frit. The authors have further demonstrated their technique [10].

In this paper, a novel laser-assisted glass frit bonding technique and its use for the encapsulation of devices based on soda-lime glass substrates is reported. Thermo-compressive glass frit bonding is used in a vastly array of photoelectronic and electrochemical applications that employ glass as supporting substrates, such as organic liquid emitting diodes (OLEDs) and dye-sensitized solar cells (DSCs) [11-13]. However the thermo-compressive method requires the use of high processing temperatures, which damages the components of the devices or increase the manufacturing process complexity as an attempt to minimize such damage. Our developed laser-assisted glass frit bonding technique allows for the preservation of the performance of the device by not subjecting its inner components to excessive heat. This is accomplished by only firing the laser beam directly at the frit, thus providing the necessary heat for it to melt and form a hermetic layer. Furthermore it was possible to avert using a glazing step and mechanical pressure during the bonding step enabling a simpler and faster sealing process. This novel laser-assisted glass frit bonding technique could be of particular importance for sealing, for example, DSCs; glass frit sealed DSC devices are expected to maintain their performance

for a much longer period of time than DSC devices sealed with state of the art polymers such as Surlyn® [11].

5.2. Material and Methods

5.2.1. Glass frit

To achieve a successful glass frit bonding it is important to select the proper glass frit. Frequently, so as to facilitate the application of the frit onto one of the joining surfaces, the glass frit powder is mixed with organic binders and solvents to form a printable paste. In this work, a lead-free, bismuth borosilicate - based glass frit paste (from AGC – ASAHI GLASS Co, Ltd.) was used. The amorphous frit has a melting temperature in the range of 475 ºC - 510 ºC and according to the supplier specifications a thermal expansion coefficient of 7.6 x 10^{-6} $°C^{-1}$, characteristic similar to that of the soda-lime glass substrates used, ca. 9.0 x 10^{-6} $°C^{-1}$ for 200 ºC - 500 ºC, obtained by Dilatometric analysis (not shown). The use of materials with similar thermal expansion coefficients is important because it helps to reduce thermo-mechanical stress in the bonding interface. The glass paste used also contains zinc oxide that acts as a wetting agent thus favouring a good bonding with the substrates.

The substrates used were 2.2 mm-thick, 30 x 15 mm^2, soda-lime glass substrates coated with a thin film (ca. 500 nm) of fluorine doped tin dioxide (SnO_2:F) – FTO, (TEC15-22 from Dyesol). Before deposition of the glass frit cord, the substrates were cleaned in an ultrasonic bath with a proper cleaning agent and then ethanol, and dried in air in a dust free chamber. Afterwards they were treated in a UV-O_3 system.

Before deposition, the glass frit paste was subjected to a homogenization process on a mixer mill using zirconium oxide grinding jars (with zirconium oxide balls), for 30 min. Then the paste was screen-printed onto the FTO glass

substrates, using a screen-printer with a 200 mesh/in stainless steel screen. Rectangular glass frit cords of 18.5 x 8.5 mm^2 (external diameter) were screen-printed. The wet screen-printed glass frit cord was 0.8 mm wide and ca. 100 µm thick. Both bonding processes took place in air.

5.2.2. Glass frit characterization

Particle size and particle size distribution of the glass frit paste were determined using a Coulter Counter equipment. Morphological features and elemental composition of the frit were assessed by Scanning Electron Microscopy equipped with Energy Dispersive Spectroscopy (SEM-EDS, Hitachi SU-70 with Bruker EDS detector). Thermal behavior of the frit was determined by Thermogravimetry and Differential Thermal Analysis (SETARAM Labsys 1600 DTA/TG-DSC) at a heating rate of 20 °C min^{-1} from room temperature to 600 °C in air, using alumina (Al_2O_3) as reference and by Dilatometric analysis in a Bahr DIL801L dilatometer.

5.2.3. Thermo-compressive glass frit bonding process

The thermo-compressive glass frit bonding process is based on the use of a low melting temperature glass as the bonding layer. It comprises three main steps: screen printing, thermal conditioning and the thermo-compressive bonding itself [3, 5]. First, glass frit paste cords were applied over the FTO surface of two glass substrates, as described in section 5.2.1. Afterwards, the printed cords were thermally conditioned according to the temperature history depicted in Figure 5.1, using an infrared oven. This thermal treatment makes the organic solvents and binders to burnout and the glass frit cords to be glazed, which helps preventing the formation of voids inside the bonding cord.

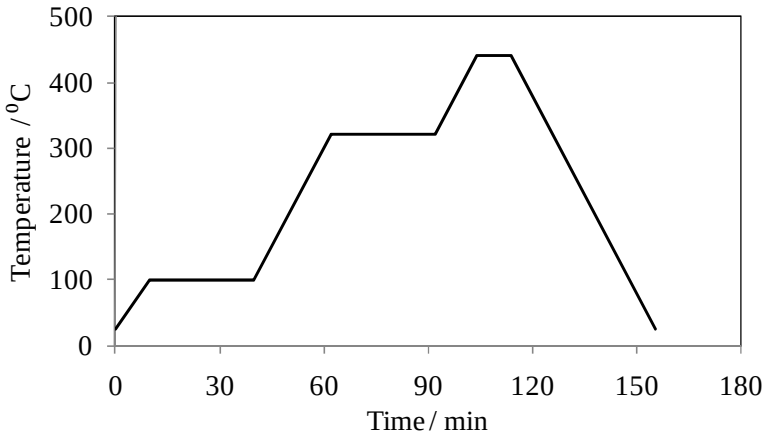

Figure 5.1 Temperature history of the thermal conditioning step used in the thermo-compressive glass frit bonding process.

Then, after cooling to room temperature, one of the two glass plates was carefully placed on top of the other and pressure was applied - Figure 5.2. The formed cell was then placed again inside the oven and heated at 10 °C/min up to 440 °C (above the frit's softening temperature), kept at this temperature for 10 min, and left to cool down to room temperature. The applied pressure facilitates the wetting of the surfaces of the substrates and the bonding of the two glass frit cord.

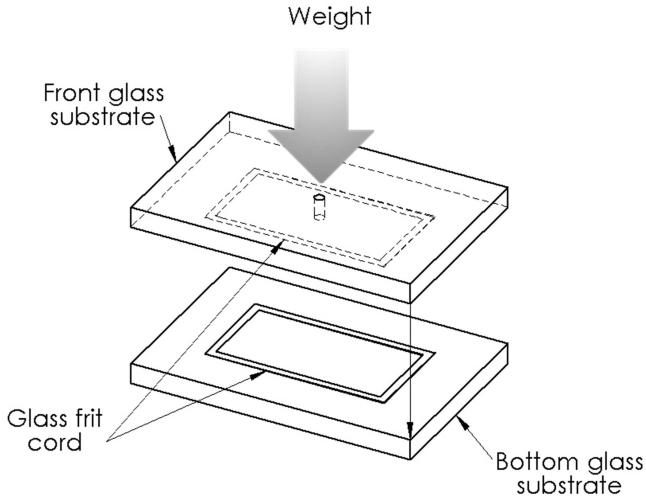

Figure 5.2 Schematic of the thermo-compressive bonding process.

5.2.4. Laser-assisted glass frit bonding process

The laser-assisted glass frit bonding method required the development of an experimental setup based on a laser scan head and a heating plate. This experimental setup, named “LaserBox” and the sealing methodology are described hereafter.

5.2.4.1. Experimental setup

The LaserBox is a closed chamber enclosing a laser scan head and a temperature controlled plate - Figure 5.3. The laser used is an ytterbium fiber-delivery diode array. The 2D scan head directs the beam through f-theta-ronar lens (focal distance = 330 mm) providing a focus spot of 64.53 μm diameter at a maximum scan length of 306.7 mm. The spot can be moved at high speed across the workpiece. The LaserBox components are controlled by two applications, a 2D scan software supplied by the manufacturer and an in-house developed LabVIEW^{TM} application used to set the firing time and the laser power. The heating plate works independently of the rest of the LaserBox and allows heating the samples even when the laser is not working. The schematic diagram of the experimental setup is shown in Figure 5.3.

For safety reasons, firing the laser beam in the LaserBox is only possible after hardware validation through several locks that ensure the operator is in a safe position. The safety controller (Sick FX3-CPU0) monitors the signals of the door switches, *Emergency Stop* button and the *Emission On* signal coming from the laser controller. The wired connection between the 2D scan controller and the laser controller, allows for the *guide enable* function to be used by the 2D scan software.

Figure 5.3 Experimental setup - LaserBox, used in the laser-assisted glass frit bonding process.

The other main hardware component of the LaserBox is the temperature controlled heating plate. This heating plate works independently of the rest of the LaserBox and allows heating the samples even when the laser is not working. The temperature is controlled by a relay temperature controller (Eurotherm® 3216).

The software functions were implemented in Windows® operating system. The LaserBox is controlled by two applications, the 2D scan software and an in-house developed LabVIEW™ application used to set the firing time and power of the laser. The 2D Scan software allows the operator to choose the following parameters: scan pattern, power set, velocity, guide (on / off). The LabVIEW™ application allows the operator to choose the laser power, laser firing time, laser status (on / off) and guide (on / off).

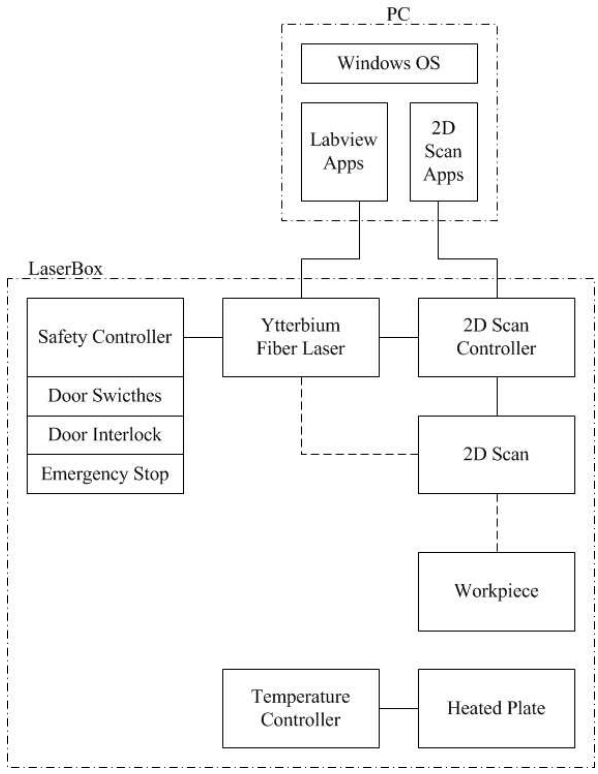

Figure 5.4 Schematic diagram of the LaserBox: ─ ─ Laser; ── data / signal.

The LaserBox state diagram is depicted in Figure 5.5. The input functions are: *Emission On* command (LabVIEW™ application), I_0; *Start* button on the laser panel, I_1; *Emergency Stop* button (NC contact) on the LaserBox panel, I_2; the switches (NC contact) on the LaserBox doors I_3 and I_4.

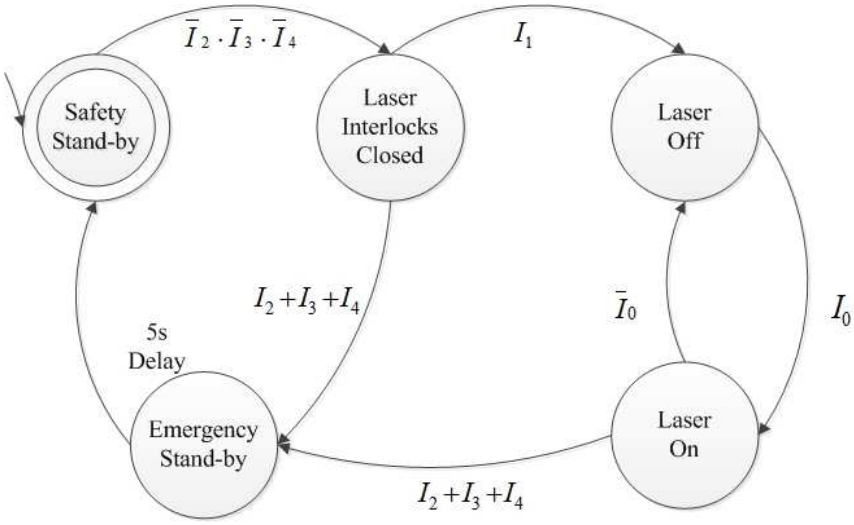

Figure 5.5 State diagram used in the LaserBox. I_0 - *Emission On* command; I_1 - *Start* button; I_2 - *Emergency Stop* button; I_3 and I_4 - LaserBox's close door switches.

The LaserBox state diagram has five main states to prevent an accidental laser firing. On the first scan, the system activates the *Safety Stand-by* state. On this state, the 2D's scan and scan controller are on, the door can be closed, or it can be open if the *Emergency Stop* is activated.

If the door is closed and the *Emergency Stop* is not pressed, the machine activates the *Laser Interlocks Closed* state. On this state, the safety controller closes the two redundant laser circuits and the ytterbium fiber laser is ready to be set (powered and fired). The operator can only open the door 5 s after one of the door switches is open, or the *Emergency Stop* is activated, to allow enough time for any pending action. On the *Emergency Stand-by* state, the door is closed and the laser interlocks are open to ensure that laser does not fire when the door is open.

The system moves to the *Laser Off* state if the *Laser Interlocks Closed* state is on and the operator press the *Start* button on the laser panel. On this state, the laser loads the settings and is ready to fire upon an operator command. The

operator can then turn the laser on / off through the PC based application. When the laser turns on, the firing pattern is defined by the 2D scan software. The system goes to the *Emergency Stand-by* state if one of the locks is violated or the operator presses *the Emergency Stop* button.

5.2.4.2. Experimental procedure

Similarly to the thermo-compressive glass frit bonding procedure, the developed laser-assisted glass frit bonding process comprises three main steps: screen printing, conditioning of the glass frit cord and the laser-assisted bonding itself. This process is depicted in Figure 5.6. It is based on the bonding principle of the thermo-compressive process [5], where a low melting temperature glass frit is used to form a hermetic bonding layer between two substrates. In this case, however, the heat necessary for the frit to melt and wet the substrates (phenomenon that occurs during the bonding step) is applied locally by a laser beam.

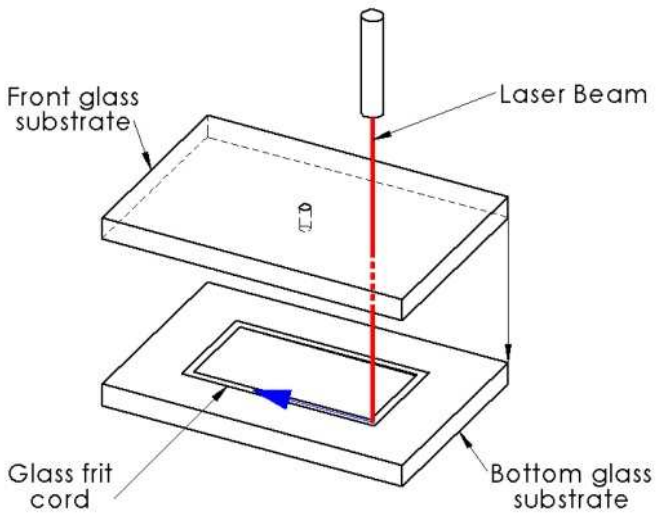

Figure 5.6 Laser-assisted glass frit bonding process schematic.

According to the procedure described in 5.2., the glass frit cord was screen-printed into one of the FTO-covered glass substrates, *i.e.*, the bottom substrate. The printed cord was then left to dry at room temperature in a clean room to allow solvents of glass paste cord to partially evaporate, helping to prevent the formation of gas inclusions. Afterwards, the pristine front glass substrate was placed on top of the bottom substrate and pressure was applied at room temperature. This was done to ensure that a proper wetting of both surfaces occurred. The samples were then transferred to the LaserBox, where they were conditioned without applied pressure. Using a heating plate, the samples were conditioned according to the temperature history depicted in Figure 5.7, and then allowed to cool to the room temperature. This heating profile allowed the burnout of the organic components (solvents and binder). Indeed it was found that only a burnout binder stage was necessary in order to achieve successful bonding, thus averting the use of a glazing step. This is an advantage since it reduces the necessary thermal energy and sealing time of the overall process.

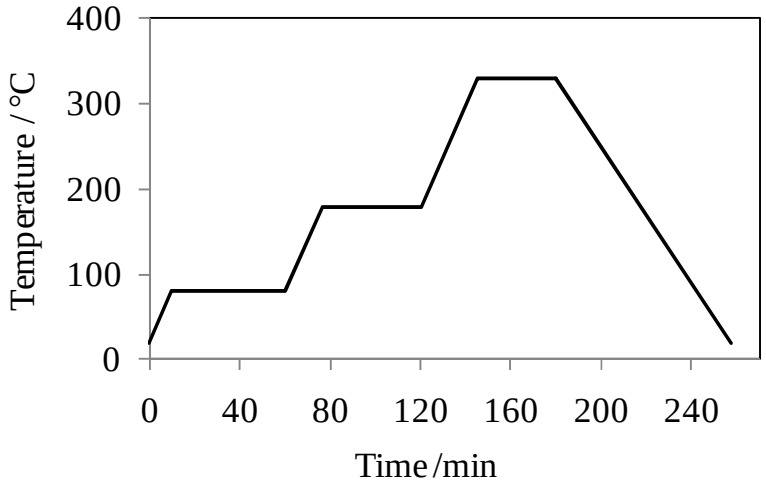

Figure 5.7 Temperature history of the thermal conditioning step used in the laser-assisted glass frit bonding process.

Afterwards, the laser-assisted bonding step took place. The laser beam was aimed at the sample and fired directly at the glass frit cord positioned between the two substrates, providing the local heating of the material. The sealing of cells was unsuccessfully attempted at room temperature as the glass substrates could not withstand the heating/cooling rates induced by the laser beam, yielding fractured samples. It was necessary to heat up the samples above 180 °C during the laser-assisted bonding step to reduce thermal-induced cracking and obtain fracture-free sealed cells. With the developed laser-assisted glass frit bonding process it was possible to avert using mechanical pressure during the bonding step. Owing to that, the possible misalignment of the substrates due to poor mismatches of the sealing cords is reduced, resulting in a simpler sealing process.

5.2.4.3. Rectangular scan pattern

The laser beam should heat the glass frit cord up to its melting temperature and allow it to bond both substrates. A rectangular scan pattern - Figure 5.8 - that provides a slower temperature increase was devised. The laser beam is directed to a starting point, fired and moved along the cord, completing several loops.

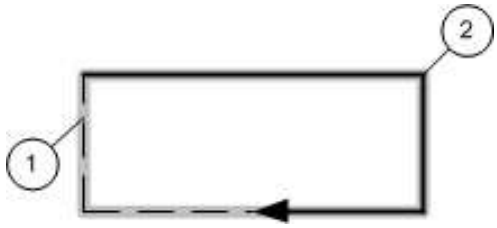

Figure 5.8 Rectangular scan pattern: 1 - Glass frit cord; 2 - Laser trajectory.

The operating parameters were then optimised within the ranges shown in Table 5.1. The operating conditions tested were the temperature of the metal plate where the glass sample was placed - *T*, the laser power used - *P*, the

velocity at which the laser scan traveled along the cord -*υ*, and the firing time of the laser - *ft*.

Table 5.1 Experimental conditions tested for the laser-assisted glass frit bonding process

Parameters	Range
Laser Power (W)	70 – 80
Laser scan velocity (mm s^{-1})	400 – 500
Plate Temperature (°C)	180 – 280
Firing time (s)	5 – 20

5.3. Results and discussion

5.3.1. Glass frit characterization

The characterization of the glass frit was preceded by a heat treatment at 320 °C for 30 minutes in air of a homogenised paste sample, aiming to burnout the organic components of the paste. The particle size distribution of the glass frit is shown in Figure 5.9. A bimodal distribution was obtained. The particles are smaller than 15 µm, the maximum recommendable particle size for thermo-compressive glass frit bonding [3].

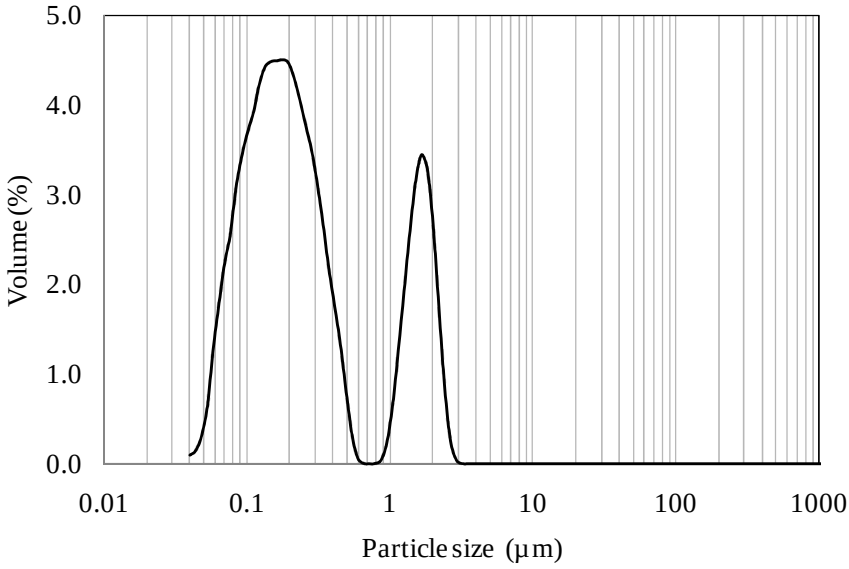

Figure 5.9 Particle size distribution of the glass frit - differential volume.

Thermogravimetric (TG) results (not shown) indicated that no significant weight changes (<1.5 wt.%) took place within the temperature range tested. Differential Thermal Analysis (DTA) of the glass frit powder gave the results depicted in Figure 5.10. DTA is a thermoanalytic technique that can provide information on transformations of a material involving heat demanding/release (ex. glass transitions, crystallization, melting) when the temperature is made to increase. This is achieved by subjecting the material to thermal treatments of controlled heating rate and then comparing changes (endothermic or exothermic) with those occurring in an inert reference. Such studies are of great practical importance since they can give valuable contributions for the understanding of the materials behaviour especially at high temperatures**.**

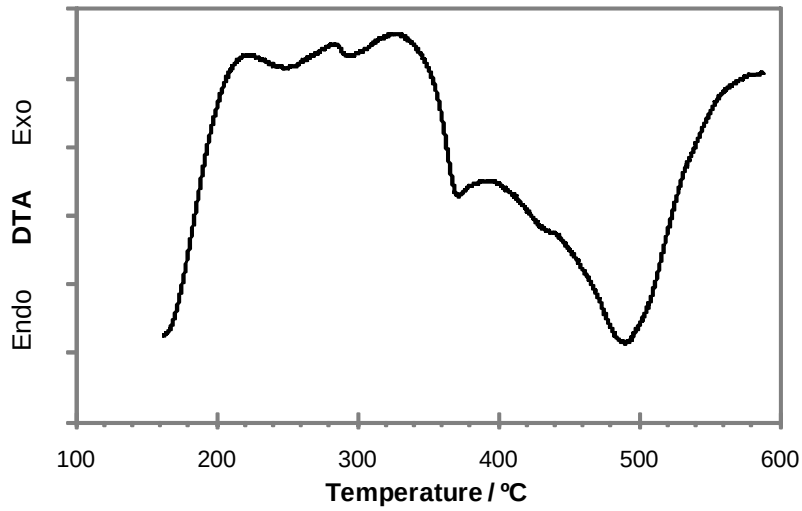

Figure 5.10 DTA of the glass frit.

Concerning the glass frit, the first relevant endothermic peak occurs at ca. 370 ºC and should be attributed to the glass transition temperature, $T_{g.}$. Melting of the glass frit occurs in the range 475 ºC - 510 ºC. The exothermic peak with the maximum at ~285 ºC is assumed to be caused by the thermal decomposition of residual organic components in the heat treated paste. Dilatometric analysis in Figure 5.11 shows that softening of the glass frit starts at 380 ºC and is accompanied by a strong sample retraction and a progressive lowering of the glass viscosity due to the disruption of the main glass structure. Wetting of the substrates by the glass frit should thus take place above this temperature and below 475 ºC, the beginning of the frit melting.

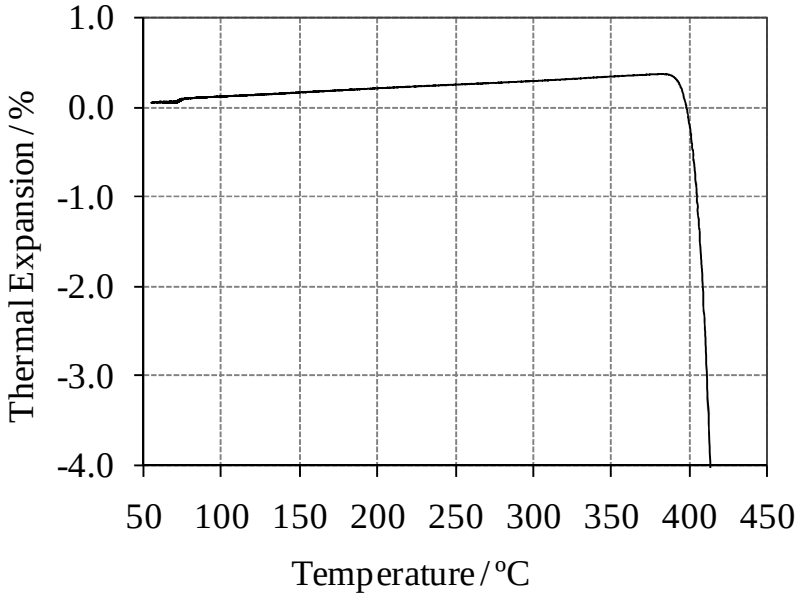

Figure 5.11 Dilatometry of the glass frit.

The feasibility of the laser-assisted glass frit bonding process was assessed by comparing a bonding cord obtained by such technique with one obtained by the traditional glass frit thermo-compressive process.

5.3.2. Thermo-compressive glass frit bonding

Figure 5.12 shows a SEM photo of a transversal cross-section of the glass frit bonding layer obtained by the thermo-compressive glass frit bonding process. The obtained glass frit cord is 22 µm-thick and exhibits, as expected [5, 6, 14], an excellent contact with both substrates and is free of gas inclusions or voids. Elemental analysis was performed by EDS to examine the glass frit cord composition. The glass frit cord is mainly composed of a bismuth oxide matrix filled with particles containing silicon and aluminum oxides.

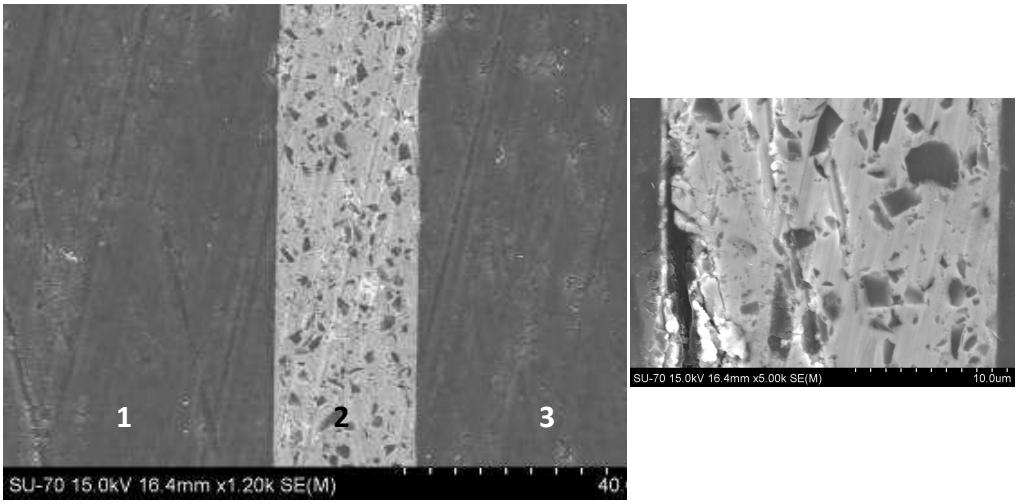

Figure 5.12 SEM micrographs (two magnifications) of a cross section of a glass frit bonding layer using the thermo-compressive process. 1 - Front glass substrate; 2 - Glass frit bonding layer; 3 - Bottom glass substrate.

5.3.3. Laser-assisted glass frit bonding

The laser-assisted glass frit bonding of two FTO coated glass plates was empirically optimised changing the operating conditions within the ranges given in Table 5.1. The quality of the bonding was assessed visually and the best specimen were further characterised. Generally, it was concluded that crack-free samples were obtained at higher temperatures of the heating plate, preferably around 280 °C; the best combinations were for the lowest laser power (P = 70 W) and above a scan velocity of 400 mm·s^{-1}; the best laser fire time was 5 s < ft < 7 s. Since the laser concentrates very high energy in a very small dot, the best operating conditions were those that originated a broader heat distribution along the glass frit cord. The high temperature of the heating plate helps to accommodate the thermal shocks, thus avoiding the formation of micro-cracks across the bonding cord and glass substrates.

Figure 5.13 shows a SEM photo of a transversal cross-section of a glass frit bonding cord obtained with the following operating conditions: laser power,

P = 70 W; temperature of the heating plate, T = 280 ºC; scan velocity, υ = 400 mm s^{-1}; and firing time of the laser, ft = 6 s.

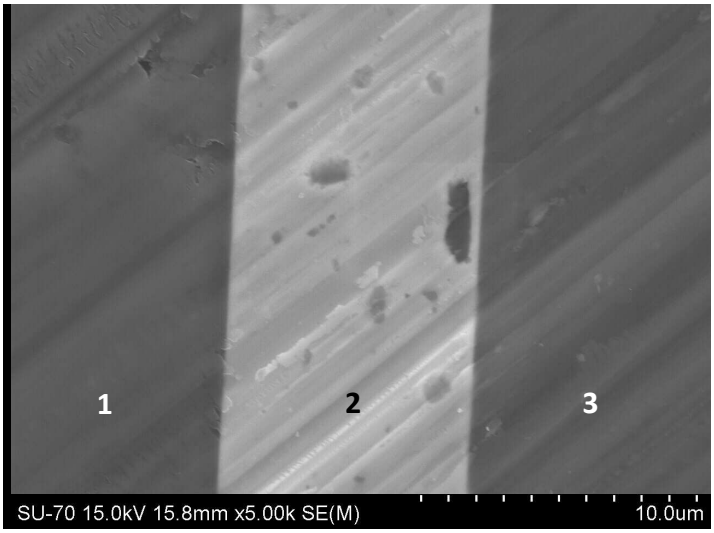

Figure 5.13 SEM micrograph of a cross section of a glass frit bonding layer using the laser-assisted process with a rectangular scan pattern. 1 - Front glass substrate; 2 - Glass frit bonding layer; 3 - Bottom glass substrate.

The glass frit cord obtained by the laser-assisted process shows a different morphology of the glass frit cord obtained by thermo-compressive process (Figure 5.12). Despite that, this glass frit cord, with a thickness of ca. 11 µm, shows also an excellent contact with both substrates and is free of gas inclusions or voids, an indication of an effective sealing. The smaller thickness should be related to the use of a single printed glass frit cord, contrary to the thermo-compressive process where a glass frit cord was printed on each of the two substrates. Elemental analysis on the filler particles that can still be seen in Figure 5.13 (although in less number than in Figure 5.12) showed that they had similar compositions (silica and aluminum oxide). The different morphology of the glass frit cord obtained by the laser-assisted process could be the result of a higher bonding temperature imposed by the laser beam. If this temperature lies in the range between the softening point and the melting point of the glass frit,

the wetting of the substrate by the glass should be favoured and a sealed cord much more homogeneous than in the thermocompressive process can be obtained.

Preliminary hermeticity tests of the laser-bonded cells yielded promising results; the tests were performed by using a low-tension liquid - ethanol - coloured with a dye (indigo carmine) injected through a pre-drilled hole (Figure 5.6). Despite its simplicity is still an effective method to find very small leaks. After injection no leakage was observed for the best specimen.

Despite the encouraging results, the laser-assisted glass frit bonding process should be further studied and improved. The temperature of the glass cord should be controlled and new laser scanning patterns considered and systematically studied. Nevertheless the developed laser-assisted bonding principle presents itself as a promising technique for efficient hermetic encapsulation of photoelectronic and electrochemical devices that use glass as supporting substrates, such as OLEDs or DSCs.

5.4. Conclusions

This paper describes a new laser-assisted glass frit bonding process that can be used for encapsulating and packaging devices based on glass substrates (glass / glass packages). This process is based on the glass frit bonding principle, with the bonding step being carried out by a laser beam that is fired directly onto the frit cord causing it to melt and to form a bonding layer.

The proposed laser-assisted glass frit bonding process yielded glass frit bonding layers that exhibited excellent contact with both substrates and were free of gas inclusions or voids - an indication of an effective sealing.

Preliminary hermeticity tests using a coloured ethanolic solution revealed no leaks.

The proposed laser-assisted glass frit bonding does not require the use of a glazing step and the application of pressure during the bonding step. This reduces the risk of misalignment of the substrates and lowers the thermal energy needed and sealing time of the overall process. The heat is also applied locally, thus protecting any temperature-sensitive materials placed inside the device.

The developed laser-assisted glass frit bonding process is a promising technique for obtaining hermetic sealing of photoelectronic and electrochemical devices, such as dye-sensitized solar cells.

Acknowledgments

R. Cruz is grateful to the Portuguese Foundation for Science and Techonology (FCT) and Efacec – Engenharia e Sistemas S.A. for its Ph.D grant (reference: SFRH/BDE/33439/2008). This work was accomplished under the project SolarSel - SI IDT - 3423/2008, co-financed by the European Union and the Portuguese Government through ADI – Agência de Inovação, in the framework of the QREN Initiative and the European Regional Development Fund through the Operational Programe for Competitiveness Factors. The authors also acknowledge Efacec – Engenharia e Sistemas S.A. for providing the much appreciated facilities and financial support.

References

1. Patel, S., D. Delaney, D.X. Xu, G. Murphy, H. Denton, and H. Hughes, *Characterization of glass on electronics in MEMS*, in *Materials and Device Characterization in Micromachining Ii*, Y. Vladimirsky and C.R. Friedrich, Editors. 1999, Spie-Int Soc Optical Engineering: Bellingham. p. 73-78.
2. Lampen, J., S. Majumder, R. Morrison, A. Chaudhry, and J. Maciel, *A wafer-capped, high-lifetime ohmic MEMS RF switch.* International Journal of Rf and Microwave Computer-Aided Engineering, 2004. **14**(4): p. 338-344.
3. Knechtel, R., *Glass frit bonding: an universal technology for wafer level encapsulation and packaging.* Microsystem Technologies-Micro-and Nanosystems-Information Storage and Processing Systems, 2005. **12**(1-2): p. 63-68.
4. Notzold, K., C. Dresbach, J. Graf, and B. Bottge, *Temperature dependent fracture toughness of glass frit bonding layers.* Dtip 2009: Symposium on Design, Test, Integration and Packaging of Mems/Moems, 2009: p. 378-383.
5. Knechtel, R., M. Wiemer, and J. Fromel, *Wafer level encapsulation of microsystems using glass frit bonding.* Microsystem Technologies-Micro-and Nanosystems-Information Storage and Processing Systems, 2006. **12**(5): p. 468-472.
6. Wu, Q., N. Lorenz, K.M. Cannon, and D.P. Hand, *Glass Frit as a Hermetic Joining Layer in Laser Based Joining of Miniature Devices.* Ieee Transactions on Components and Packaging Technologies, 2010. **33**(2): p. 470-477.

7. Lee, M., M.G. Pecht, and W. Lee, *Thermal assessment of glass-metal composition plasma display panels using design of experiments.* Ieee Transactions on Components and Packaging Technologies, 2004. **27**(1): p. 210-216.
8. Watanabe, W., S. Onda, T. Tamaki, and K. Itoh, *Direct joining of glass substrates by 1 kHz femtosecond laser pulses.* Applied Physics B: Lasers and Optics, 2007. **87**(1): p. 85-89.
9. Mathieu, A., R. Shabadi, A. Deschamps, M. Suery, S. Matteï, D. Grevey, and E. Cicala, *Dissimilar material joining using laser (aluminum to steel using zinc-based filler wire).* Optics & Laser Technology, 2007. **39**(3): p. 652-661.
10. Lorenz, N., S. Millar, M. Desmulliez, and D.P. Hand, *Hermetic glass frit packaging in air and vacuum with localized laser joining.* Journal of Micromechanics and Microengineering, 2011. **21**(4): p. 045039.
11. Sastrawan, R., J. Beier, U. Belledin, S. Hemming, A. Hinsch, R. Kern, C. Vetter, F.M. Petrat, A. Prodi-Schwab, P. Lechner, and W. Hoffmann, *A glass frit-sealed dye solar cell module with integrated series connections.* Solar Energy Materials and Solar Cells, 2006. **90**(11): p. 1680-1691.
12. Lee, W.J., E. Ramasamy, D.Y. Lee, and J.S. Song, *Glass frit overcoated silver grid lines for nano-crystalline dye sensitized solar cells.* Journal of Photochemistry and Photobiology a-Chemistry, 2006. **183**(1-2): p. 133-137.
13. Yeon, D.H., K.K. Kim, N.G. Park, and Y.S. Cho, *Bismuth Borosilicate-Based Thick Film Passivation of Ag Grid for Large-Area Dye-Sensitized Solar Cells.* Journal of the American Ceramic Society, 2010. **93**(6): p. 1554-1556.

14. Notzold, K., J. Graf, and R. Muller-Fiedler, *A four-point-bending-test for the stability assessment of glass frit bonded molded microsensors.* Microelectronics Reliability, 2008. **48**(8-9): p. 1562-1566.

Chapter 6

Integration of graphene-based CEs with laser-assisted glass frit sealing in pre-submodule DSCs

Upon developing the laser-assisted glass frit bonding technique described in Chapter 5, an initial assessment of graphene-based counter-electrodes (CEs) in scaled-up dye-sensitized solar cells (DSCs), in a submodule configuration was carried out. The objective of this work was to validate the use of the developed graphene-based CE with the developed sealing technique, in order to ensure a proper operation of the cell.

6.1. Module configuration of DSCs

As in other photovoltaics technologies, module production of DSCs is carried out using an integrated series connection. This is preferred to an external connection of individual cells due to cost-efficiency, simpler processing manufacturing and aesthetic appearance. As expected due to its distinct operational principle, the design of the modules of DSCs is different from other thin-films technologies. Figure 0.1 shows the manufacturing procedure for a series connected Z-type module of DSCs, one of the most used configurations. For its assembly, first the TCO is structured by laser scribing. Then the catalyst, the metal grid, TiO_2 and glass frit layers are screen-printed on top of the TCO. After sintering the components, the counter-electrode is placed toping the photoelectrode and a hermetic seal is created through a laser beam as described in Chapter 5. The TiO_2 is then died through recirculation and finally the electrolyte is injected through previously drilled holes. Sealing of such holes is

achieved through a thermoplastic gasket. This configuration allows for a clear separation of each individual cell. This is important as they should remain kept insulated not only electrically from each other, but chemically as well, as photoinduced electrophoresis can occur. The metal grid responsible for extracting the generated current is also protected against the corrosive nature of the electrolyte. By using this configuration it is also expected that no shunt conductances are to be inherently built-in the modules [1, 2]. In this configuration, all photoanodes face one side of the module, thus avoiding current mismatch.

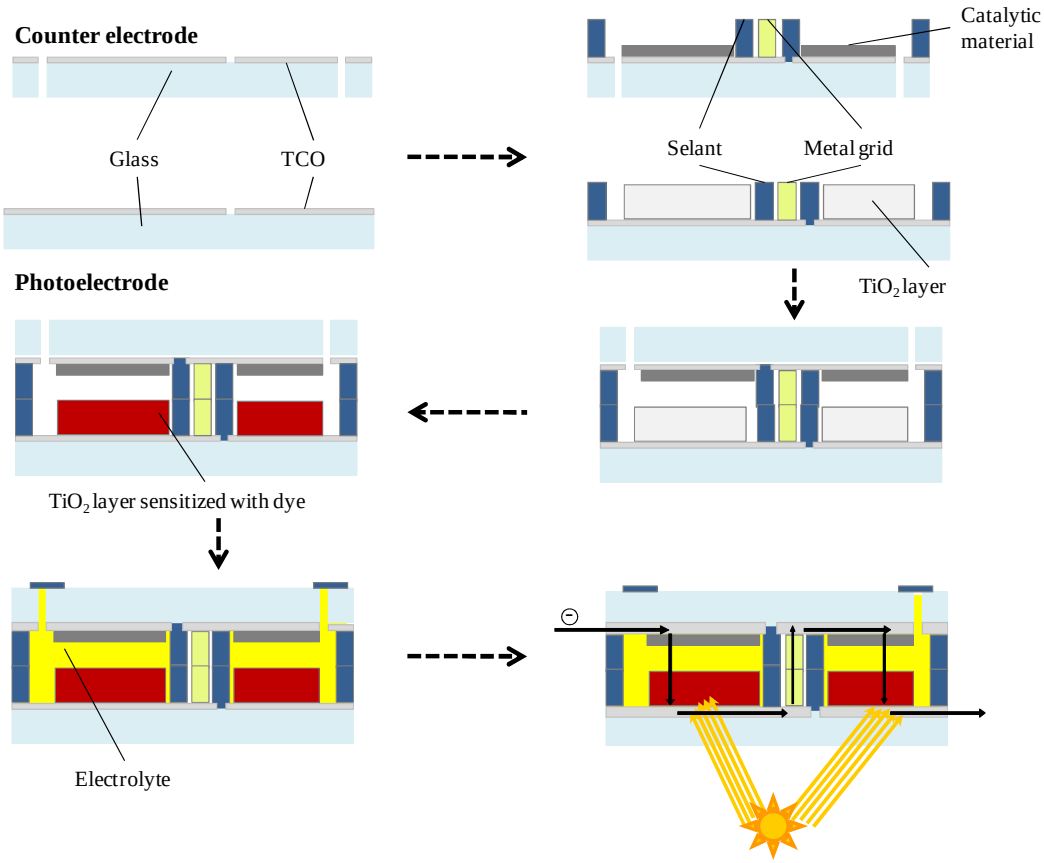

Figure 6.1 Schematic of the assembly procedure for an integrated series connection of a Z- type module. The last figure shows the electron path through the different cells.

The integrated series connection of DSC modules can also be designed in two other ways, a W-type configuration and a monolithic type [3]. The W-type configuration - Figure 6.2, is very similar to the Z-type in its construction; however, the metal grid is not needed as the electrical contact is achieved by placing the cells alternatively in an inverted pattern. This reduces the cost of the module but can lead to mismatch current problems.

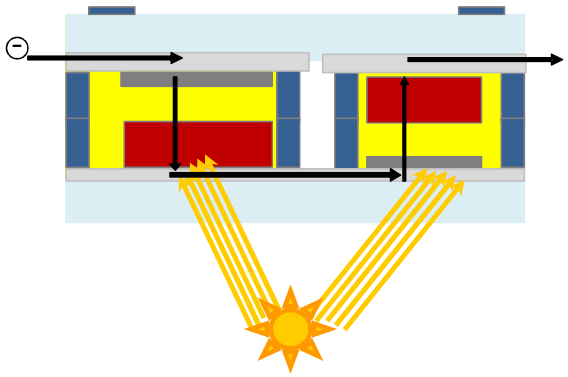

Figure 6.2 Schematic an integrated series connection of a W- type module showing the electron path through the different cells.

Another used module design is the monolithic configuration. The monolithic configuration is frequently used in solid-state DSCs. Its use is often discarded as they yield lower efficiencies [4]. Additionally the manufacturing process is more complex. Also it is not possible to fabricate semi-transparent cells with this configuration as a scattering layer (eg. ZrO_2) must be applied as spacer on top of the TiO_2 semiconductor, and a carbon-based thick layer (typically graphite) is placed in the space occupied by the electrolyte serving simultaneously as the catalyst and as a medium for the redox mediator species. Both ZrO_2 and graphite layers are porous so that the electrolyte can penetrate through them. The use of the graphite layer often implies discarding the use of the second TCO glass substrate in the counter-electrode, which could translate into a cheaper cell (since TCO is one of the greatest cost factors in a DSC) [4].

This configuration does not require any metal grid lines, furthermore reducing the final cost of the DSC module [4, 5].

6.2. Proof of principle of module manufacturing

The Z-connection configuration seems to be the most appealing. In order to evaluate the behaviour of the developed graphene-based CEs with the laser-assisted glass frit bonding, modular Z-type were fabricated, but without the application of the current collector metal grid. This kind of architecture is often referred to as a masterplate [6]. In a masterplate the current generated from each individual cell is collected externally, permitting for each cell to be individually checked. It is often employed when assessing a proof of principle and module efficiency is not particularly relevant, as it allows testing the materials without having to optimize the module parameters (active area width, cell thickness and width, metal grid width, etc).

It is important to notice that the materials (commercial materials from Solaronix) and operating conditions used to prepare these devices were not optimized since the main goal was not to prepare very efficient cells/modules but rather to validate the laser assisted sealing technique with the use of graphene-based CEs. Furthermore it is also worth mention that the graphene-based CEs were prepared as described in Chapter 3, although using non-optimized films of oxidized graphene from commercial graphene nanoplatelets, albeit transparent.

For that, individual lab-size cells (0.75 cm^2) were fabricated with Pt and graphene-based CEs, in a similar fashion as described in Chapter 3, albeit being laser-sealed. Additionally, half-cells of different areas (0.75 cm^2 and 4 cm^2) were also fabricated using the aforementioned CEs, but sealed with *Surlyn*. A masterplate of 7×7 cm^2 with 4 individual cells was constructed for each type of CE, using the laser-assisted tecnhique. Each cell had an external perimeter of

2.5 × 2.5 cm and an active area of 2 × 2 cm^2 (4 cm^2). Laser sealing conditions of all aforementioned cells are based on those described in Chapter 5 and elsewhere [7].

6.3. Results and discussion

Figure 6.3 shows the masterplate fabricated with the graphene-based CEs. Two of the cells were not sensitized with the dye and electrolyte was not introduced. In those cells, it is possible to notice their transparency.

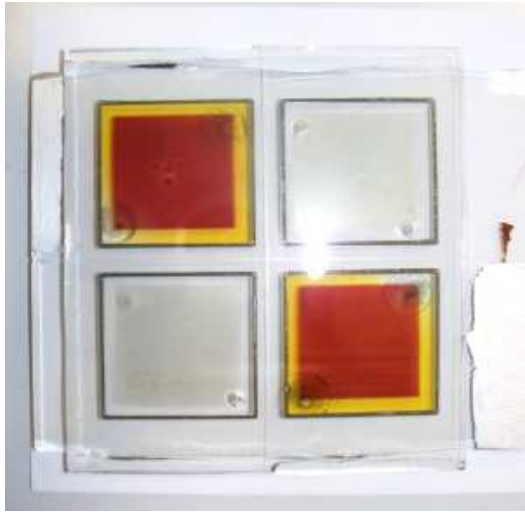

Figure 6.3 Photograph of a 7 × 7 cm^2 masterplate, having 4 individual cells with the graphene-based CEs. In two of the cells dye sensitization and electrolyte introduction was not carried out.

The performance of the DSCs in the masterplate was compared to the lab-size DSCs. Table 6.1 shows the fitted EIS parameters obtained from the half-cells analysis as described in Chapter 3. In there, it is also expressed a relative performance measurement based on the charge-transfer resistance (R_{ct}) value:

$$\Delta R_{ct} = \frac{(R_{ct,Pt} - R_{ct,graphene})}{R_{ct,graphene}} x100 \quad (6.1)$$

Table 6.1 Fitted EIS data from half-cells with Pt and graphene-based CEs.

CE	**Pt**	**Graphene-based**	
Active area of the CE / cm^2	0.75 / 4.00	0.75	4.00
R_{ct} / Ω cm^2	14.8	38.4	54.8
	Δ R_{ct} / %	-61.6	-73.0
	Δ R_{ct} / % (average)	-67.3	

The R_{ct} of the graphene-based CE is clearly inferior to the one obtained in Chapter 3, an indication of the use of the non-optimized films. The average relative performance based on the R_{ct}, ΔR_{ct}, for both areas, of the graphene-based CEs was ca. 67 % inferior to that of the Pt CE.

The performance of the DSCs at lab-scale (0.75 cm^2) and in the masterplate (4 cm^2), both laser sealed, were compared through their *I-V* parameters. Such measurements were taken as described in Chapter 3, at AM 1.5, 25 °C and 1 sun. The corresponding photovoltaic parameters of these cells (short-circuit current density, J_{sc}; open circuit voltage, *Voc*; fill factor, *FF*; and efficiency, η) are presented in Table 6.2. In there, it is also expressed a relative performance measurement based efficiency value:

$$\Delta\eta = \frac{(\eta_{grapheneCE} - \eta_{Pt})}{\eta_{Pt}} \quad (6.1)$$

Table 6.2 *I-V* parameters of DSCs fabricated with the Pt and graphene-based CEs, at a lab (0.75 cm^2) and masterplate-scale (4 cm^2) sizes

CE	**Pt**		**Graphene-based**	
DSC's active area / cm^2	0.75	4.00	0.75	4.00
V_{OC} / V	0.75	0.75	0.65	0.67
J_{SC} / mA cm^2	8.49	4.16	7.56	3.17
FF	0.54	0.39	0.22	0.19
η / %	3.40	1.23	1.08	0.41
		$\Delta\eta$ / %	-68.2	-67.0

The results in Table 6.2 show a relative efficiency, $\Delta\eta$, for the graphene-based CEs of ca. 68% inferior to that of the Pt CE, for both areas. This relative efficiency is lower than the ones obtained in Chapter 4 and even in Chapter 3 due to the non-optimized nature of the graphene-based films. The fact that the same relative efficiency was obtained for both DSCs with different active areas (0.75 cm^2 and 4 cm^2) seems to suggest that the laser-assisted glass frit sealing technique could be used with graphene CEs without lost of efficiency. It can be assumed that there is a direct correlation between the R_{ct} of a CE and the corresponding efficiency yield by a DSC fabricated with such CE [8, 9]. Accordingly, when the relative performance of both DSCs and half-cells are compared, it can be seen that, for the graphene-based CEs, the ΔR_{ct} of the half-cell sealed with the *Surlyn* thermoplastic is similar to the $\Delta\eta$ of the laser-assisted glass frit sealed DSC (ca. 68% inferior to that of Pt). This is another good indication that the developed sealing method can be successfully applied in tandem with graphene-based CEs.

6.4. Conclusions

Based on the presented preliminary results it appears that developed laser-assisted glass frit bonding technique can be applied to graphene successfully and that further scaling-up of DSCs modules using such CEs can be accomplished without compromising the overall performance of the cell.

References

1. Sastrawan, R., J. Beier, U. Belledin, S. Hemming, A. Hinsch, R. Kern, C. Vetter, F.M. Petrat, A. Prodi-Schwab, and P.L.W. Hoffmann, *New interdigital design for large area dye solar modules using a lead-free glass frit sealing.* Progress in Photovoltaics: Research and Applications, 2006. **14**(8): p. 697-709.
2. Sastrawan, R., J. Renz, C. Prahl, J. Beier, A. Hinsch, and R. Kern, *Interconnecting dye solar cells in modules - I-V characteristics under reverse bias.* Journal of Photochemistry and Photobiology a-Chemistry, 2006. **178**(1): p. 33-40.
3. Tulloch, G., *Light and energy--dye solar cells for the 21st century.* Journal of Photochemistry and Photobiology A: Chemistry, 2004. **164**(1-3): p. 209-219.
4. Kay, A., I. Cesar, and M. Gratzel, *New benchmark for water photooxidation by nanostructured alpha-Fe2O3 films.* Journal of the American Chemical Society, 2006. **128**(49): p. 15714-15721.
5. Kato, N., K. Higuchi, H. Tanaka, J. Nakajima, T. Sano, and T. Toyoda, *Improvement in long-term stability of dye-sensitized solar cell for outdoor use.* Solar Energy Materials and Solar Cells, 2011. **95**(1): p. 301-305.
6. Kroon, J., N. Bakker, H. Smit, P. Liska, K. Thampi, P. Wang, S. Zakeeruddin, M. Grätzel, A. Hinsch, S. Hore, U. Würfel, R. Sastrawan, J. Durrant, E. Palomares, H. Pettersson, T. Gruszecki, J. Walter, K. Skupien, and G. Tulloch, *Nanocrystalline dye-sensitized solar cells having maximum performance.* Progress in Photovoltaics: Research and Applications, 2007. **15**(1): p. 1-18.

7. Ribeiro, F., J. Maçaira, R. Cruz, J. Gabriel, L. Andrade, and A. Mendes, *Laser assisted glass frit sealing of dye-sensitized solar cells.* Solar Energy Materials and Solar Cells, 2012. **96**(0): p. 43-49.
8. Hauch, A. and A. Georg, *Diffusion in the electrolyte and charge-transfer reaction at the platinum electrode in dye-sensitized solar cells.* Electrochimica Acta, 2001. **46**(22): p. 3457-3466.
9. Aitola, K., J. Halme, N. Halonen, A. Kaskela, M. Toivola, A.G. Nasibulin, K. Kordás, G. Tóth, E.I. Kauppinen, and P.D. Lund, *Comparison of dye solar cell counter electrodes based on different carbon nanostructures.* Thin Solid Films, 2011. **519**(22): p. 8125-8134.

Chapter 7

Conclusions and Future Work Suggestions

The main objective of this work was to narrow the gap that presently exists in dye-sensitized solar cells' (DSCs) development that is preventing them to become a commercial reality in the photovoltaic energy market. In order to do so, two key points were tackled: i) the development of an alternative and low-cost catalyst (CE); ii) the development of a reliable sealing technique for DSCs based on glass substrates.

Carbon-based materials were studied as a potential replacement for platinum (Pt) as catalytic materials for the electrochemical reaction that occurs in the counter-electrode (CE) side. The use of high surface area single-wall nanohorns (SWNH) with the addition of 10 wt.% of hydroxyethylcellulose (HEC) was investigated. Films comprised of pristine SWNH/HEC could be used as CEs in temperature-limited applications (< 180 ºC), albeit being necessary for them to be several µm–thick. When pristine SWNH were decorated with Pt nanoparticles, a Pt/SWNH/HEC film used as a CE was capable of yielding the same performance as the reference Pt CE, although with half of its transparency, but with less 50 wt% of Pt. The Pt/SWNH/HEC CE could also be applied favourably into sensitive-temperature applications.

Stand-alone graphene oxide (GO) films were studied as transparent (transmittance measured at 500 nm > 80 %) CEs for DSCs. A new simpler manufacturing process for graphene-based films was disclosed. It was discovered that thermal annealing under an inert atmosphere of GO films was sufficient to create a CE as catalytic as a film comprised of chemically reduced

GO platelets that then suffered the same annealing. The described thermal annealing allowed preserving the active catalytic sites while simultaneously increasing the graphene sheets electrical conductivity. This eliminated the need to pre-reduce graphene oxide platelets, thus making the manufacturing process cheaper by making it simpler to create stable dispersions for spray deposition. Nevertheless, their efficiency was ca. 75 % of the reference Pt CE.

A composite CE was created in order to match or surpass the performance and transparency of the reference Pt CE. Oxidized graphene platelets were used on top of FTO substrates decorated with a very small amount of electrophoretically deposited nickel particles. By thermally annealing them in an inert atmosphere, it was possible to create a CE that had lower charge-transfer resistance than the Pt CE. This translated into yielding DSCs with similar efficiencies (ca. 7.5%). SEM, AFM and Raman analysis seemed to indicate that, along with the effect created by the thermal annealing, Ni particles were responsible for further restoration of conductivity in the oxidized graphene platelets on the surface contacting the FTO, and that this was essential for achieving such good performances. Preliminary stability tests performed on such CEs suggested that they have similar stability as the Pt CE. The created transparent (transmittance measured at 500 nm above 80 %) oxidized graphene/Ni composite CE presents itself as the front-runner replacement of Pt for iodide/triiodide based redox electrolytes.

Long-term stability is a key issue regarding the future commercialization of DSCs. Owing to that a novel sealing technique for proper encapsulation of DSCs based on glass substrates (glass / glass packages) was developed. The method was based on the use of a laser beam to provide a localized heating only to the glass frit causing it to melt and create a bonding (sealing) layer. This would ensure that any temperature-sensitive materials placed inside the device would be protected. The bonding layers exhibit excellent contact with both

substrates and were free of any gas inclusions or voids, indicating a mechanical stable sealing.

The developed sealing technique was applied to pre-submodule scaled DSCs (active area of 4 cm^2). The applicability of the developed graphene films with the laser-assisted glass frit sealing on those pre-submodules was assessed. Preliminary tests seemed to indicate that the novel laser-sealing technique can be successfully applied to scaled-up DSCs. Additionally, graphene-based CEs appeared to be compatible with the novel laser sealing method, as no loss of performance was found when compared with the traditional polymeric sealing.

Dye-sensitized solar cells have the potential to play an important role in the future of energy supply. Its low-cost potential and versatile applicability, together with its unique physics, that makes it possible to provide a stable energy supply and also manufacture flexible and light-weight systems, makes DSCs a potential very strong competitor, particularly in the case of portable electronic equipment and in building integrated photovoltaics. As seen throughout this dissertation, a marketable product is not very far. Nonetheless, important developments must occur to transform DSCs in a technological photovoltaic reference.

Scaling-up this technology should be the next step. As shown in this dissertation, the novel developed laser assisted glass frit sealing could provide the answer to the long-term stability issue. Submodules of DSCs up to 15 x 15 cm^2 have been in the meantime prepared using the laser-assisted sealing technology. These submodules would then be incorporated into modules using an adequate balance of system that would tailor them (power, voltage and current) in order to respond to the final customer's needs. It is imperative that the fabricated submodules must comply with international standards (such as IEC 61646 (IEC, 2008) and JIS C 8938 standards (JIS C 8938, 1995)) in order

to confirm their stability and consequently obtain approval for commercialization.

Presently it is estimated that the current state-of-the-art submodular architecture could only yield efficiencies of ca. 8%. Although this efficiency value is already sufficient for industrialization, module efficiency should be increased. Solutions could come in the form of decreasing the substrates sheet resistances by modification of the conductive oxide layer, as this plays the most important role in the gap of ca. 4 percentage points that exists to the state-of-the-art DSCs. Other solutions comprehend changing the typical module configuration used for the DSCs. Efficiency can be also increased by changing the cell's components: fabrication of new photosensitizers that absorb more energy, preferably cheaper (such as organic dyes); creation of new structures of photoanodes; substitution of the traditionally used iodide redox electrolyte for another redox mediator that lowers the difference between the redox potential of the dye and redox mediator (for iodide redox systems it is ca. 600 mV). As a matter of fact, by manipulating the energy levels, combination of new organic dyes with cobalt or ferrocene based redox electrolytes could in the very near future increase efficiencies up to more than 15 %, as a result of an increased open-circuit voltage (to more than 1 V) and short-circuit current (to more than 20 $mA \cdot cm^{-2}$).

Regarding the CE, efforts should be carried out to improve the performance of the graphene-based counter-electrode. Further studies on the graphene/Ni composite should also be made. Accelerated aging tests should be performed extensively in order to prove its stability. In parallel, the graphene/Ni composite CEs should be tested in the submodules fabricated with the laser-assisted glass frit sealing technique. This should prove to be a surplus, as graphene materials have also been proven to be much suitable catalysts for cobalt electrolytes than Pt, thus making it the perfect CE material for the next higher efficiency DSCs.